Infrared stimulation of neurons

David Moreau

Thèse de doctorat

Université de Limoges

Ecole doctorale n°521 Sciences et Ingénierie pour l'information, Mathématiques

Institut de recherche XLIM

Thèse pour obtenir le grade de

Docteur de l'Université de Limoges

Biophysique

Présentée et soutenue par

David Moreau

Le 26 Septembre 2017

Infrared stimulation of neurons

Thèse dirigée par Rodney O'Connor et co-encadrée par Claire Lefort

JURY :

Président du jury

M. Vincent Couderc, Directeur de recherche CNRS, Institut de recherche XLIM.

Rapporteurs

M. Fabrice Bardin, Professeur, Institut d'Electronique et des Systèmes (IES), Université de Nîmes.

M. Jean Valmier, Professeur, Institute for Neurosciences Montpellier (INM, INSERM), Université de Montpellier.

Examinateurs

M. Vincent Couderc, Directeur de recherche CNRS, Institut de recherche XLIM.

M. Jean-Marc Edeline, Directeur de recherche CNRS, Institut de Neurosciences Paris-Saclay.

M. Rodney O'Connor, Maître assistant, Ecole Nationale Supérieure des Mines de Saint-Étienne.

Mme Claire Lefort, Chargée de recherche CNRS, Institut de recherche XLIM.

Invitée

Mme Sylvia Bardet-Coste, Maître de conférences, Institut de recherche XLIM, Université de Limoges.

Acknowledgements

First of all, I express my gratitude to Mr. Fabrice Bardin, Professor at the University of Nîmes and to Mr. Jean Valmier, Professor at the University of Montpellier, to have accepted to read this manuscript, to judge it, and for their comments to help to improve it. My thanks also go to Mr. Vincent Couderc, CNRS Research Director at the XLIM research institute to have accepted to be the president of the jury of this thesis and to Mr. Jean-Marc Edeline, CNRS Research Director at the Institute of Neurosciences of Paris-Saclay to have agreed to be in this jury and for his helpful comments during the defense.

I also thank more particularly Rod O'Connor and Claire Lefort to have proposed the subject of the infrared neural stimulation as a PhD research project which I enjoy a lot. I also thank them for all the help that they gave me during the all PhD, each of them in different and complementary fields useful in such a multidisciplinary work, for the time that they dedicated to me every time I needed and to have learnt me to become the young researcher who I am now.

I would also like to thank Sylvia who was always very helpful when I needed and with who the in-vivo work became possible. This week of experiments was really great. I also thank her to have agreed to be in the jury of the thesis as a guest.

Thanks also to Philippe Leveque for his help on a common and unfinished work for now, and for his help at the end of this PhD, especially with all the administrative tasks related to the defense.

My thanks go also to the XLIM research institute, the photonics axis and the BIOEPIX lab, for their welcome within their teams and for all the good moments shared.

I also thank all the professors with who I shared my experience of teaching, especially Thierry Trigaud, Agnes Desfarges-Berthelemot and Raphael Jamier, for their help and advices to improve my pedagogy with the students.

Thanks also to Nathalie and Elodie, the two administrative persons in charge with who I worked with, for all their help during those three years.

Of course, a great thank to all of the other PhD students with who I lived and shared this experience during the three last years. I won't cite every single one of you because I could forget some, and I don't want to create jealousy. But a special thank to Erwan, my office colleague during those three years, that was a great pleasure to me to be in the same office as you, I'll keep wonderful memories of our out of subject studies, of all the jokes that we did, but less for the ones you did to me!

I would like also to thank Vincent and Lionel, who learnt me to be a waiter, which allowed me to pay my studies until the master's degree, and for all the good moments shared. Without you guys, my life would have be way more complicated!

I also thank finally everyone around me, family, friends and girlfriend, for the support that they give to me and to make me enjoy life.

Droits d’auteurs

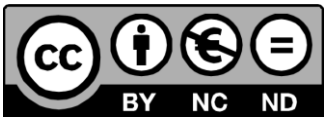

Summary

Introduction

The neural stimulation is the process to use an external energy source in the purpose to trigger action potentials in neurons of the peripheral and central nervous systems. The Initiation of action potentials is a central point of interest in many researches and clinical procedures in order to develop therapeutic tools.

In history, the traditional neural stimulation is based on the use of electrical methods. The application of electricity as a therapeutic tool goes back to very former times. According to some texts, the Greeks used the electric fishes and the shocks that they caused to calm the pain and to try to cure some diseases. Indeed these fishes' shocks anesthetize the region of the body affected since they hardly stimulate the nerves, and a therapeutic action on the paralyses was hoped. Then, in Roman times, medical specialists recommended the discharges of the torpedo, an electric fish found in the Mediterranean Sea, as a cure for the gout.

In more contemporary times, the use of electrical stimulation remains the main method to initiate neuronal activity with for example the works of Fritsch and d'Arsonval at the end of the 19th century, of Goddard in 1969 or more recently of Benabid on the deep brain stimulation. The main advantages of the electrical stimulation are the ease to control and quantify the stimulation parameters such as intensity, duration, frequency. Its spread use, even in clinical cases, makes this stimulation method the more developed.

A novel method for neural stimulation has gained increased interest in the last years based on the use of infrared laser light. Since its first application in 2005, Successful neural stimulation using infrared exposure have been reported in cells, and in both the peripheral nervous system and in the central nervous system. The main advantages of the infrared neural stimulation are that a contact is not needed between the targeted cells and the tip of the optical fiber delivering the infrared and it presents a high spatial resolution. However, the mechanism underlying the stimulation of neurons by the exposure to infrared laser light is not fully understood. So far, it is believed to have a photo-thermal origin, the infrared light being absorbed by the water in the tissue, leading to an increase of temperature in the targeted cell and in the surrounding area. Thus, the main risk to have in mind when using infrared neural stimulation is the risk of heat induced damage.

In this thesis, the mechanism underlying the infrared neural stimulation is investigated in an all optical manner. A first chapter attempts to present the context of the work in a more thorough way. In a second chapter, an optical method to probe the temperature changes at the cellular level is presented. Then, the third chapter leans on a pharmacological study and calcium imaging to try to supply a clarification in the mechanism underlying the infrared neural

stimulation. Finally, the fourth chapter provides the proof that neural activity induced by infrared exposure may be probed by calcium imaging in the central nervous system *in vivo*.

Chapter I. Context of the work

I.1. The nervous system

I.1.1. General presentation

Basically, the nervous system is a collection of specified cells allowing an organism to code sensory information and to respond to the environment. It receives information from the external environment as well as from the internal body functions, and after a step of information processing, produces an adapted response. In a common way, the vertebrate's nervous system may be divided into two parts: the Central nervous system (CNS) and the peripheral nervous system (PNS). The CNS is the major division, composed of the brain and the spinal cord. The PNS consists of all the other nerves in the body, those which do not lie within the CNS.

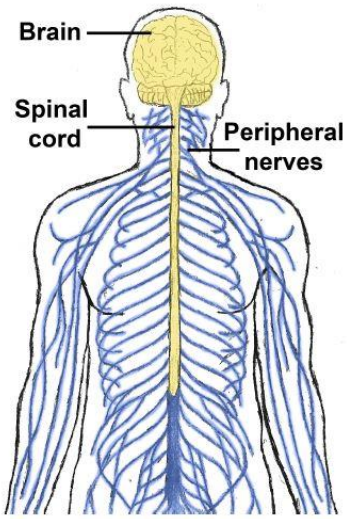

Figure I-1 Division of the nervous system into central nervous system (yellow) and peripheral nervous system (blue) [1].

The nervous system is pervasive in the body, allowing a good control and regulation of body functions in a fast timescale. Indeed, only a few milliseconds are necessary to initiate nervous signals which travel at speeds that exceed 100 $m.s^{-1}$.

I.1.2. Neural cells

The cells in the nervous system are classified into two broad categories: the neurons (or nerve cells) and the neuroglial cells (or glial cells). The main difference between those two types of cells is that neurons are specialized for electrical signaling over long distances when neuroglial cells are not. The glial cells are considered as supporting cells. They have essential functions in the brain, like to supply nutrients to the neurons, to maintain homeostasis, to remove dead neurons, to insulate neurons electrically by forming myelin and to support neural activity.

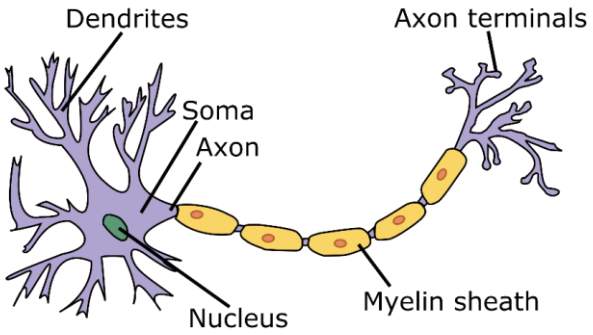

Figure I-2 Schematic representation of a neuron.

The neurons have a basic cellular organization looking like the other cells in the body. They are nevertheless distinguished by their specialization for intracellular communication. Their membrane components have a specific organization for electrical signaling, like the elaboration of dendrites arborization that arises from neuronal cell body. The axon, another part of the neuronal cell, is specialized in the electrical signal conduction. The myelin sheath which may surround it allows to insulate the neuron electrically, and allows also faster electrical signal conduction through the axon. Finally the axon terminals are privileged locations to make synaptic contacts and transmit the electrical signal to another neuron.

I.1.3. Generation and transmission of an action potential

I.1.3.1. Membrane resting potential, start point of the action potential

The information transmission in all the body is ensured by the neurons and their ability to generate electrical and chemical signals. Action potentials represent the main electrical signals generated by the neurons. Chemical signals are delivered through synapses, the region of contact between two neurons. At rest, it exists a difference in the concentrations of specific ions between inside and outside the plasma membrane. For example, Na^+, Cl^- and $Ca2^+$ ions have a greater concentration in the extracellular medium whereas K^+ ions are more numerous in the intracellular medium. This is the cause, of the generation of an electrical potential across the membrane.

To ensure the ions flow and control their concentrations at rest, the plasma membrane of the neurons is permeable to some of these ions. Two different kinds of proteins, located in the cell membrane, work against each other. It is about ion transporters and ion channels. Ion channels ensure the selectivity of the membrane permeability. Each ion channel allow a specific kind of ions to pass through the plasma membrane, following the concentration gradient. The opposite effect is ensured by proteins known as active transporters. In this case, the proteins participate by moving ions inside or outside of cells in the opposite direction of their concentration gradient. At rest, the electrical potential across the plasma membrane is called membrane resting

potential. In function with the type of neuron, the membrane resting potential may worth between -40 mV and -90 mV.

I.1.3.2. Ionic origin of the action potential

The electrical signal used by the neurons to code information, called the action potential, is generated by changes in the membrane potential. When the membrane potential pass above a certain threshold, due to a temporary permeability to sodium ions or to an external stimulus, it results in the opening of sodium ion channels. Once those channels activated, there is an influx of sodium ions resulting in an increase in the membrane potential called the depolarization. After this augmentation, sodium ion channels become inactivated and there is an increase in the permeability to potassium ions with the activation of the associated channels. Potassium ion concentration being higher in the cell than out of the cell at rest, ions move this time from inside to outside of the cell, leading to the decrease of the membrane potential. This step is called the repolarization. After this phase, there is a short step of hyperpolarization. During it, the permeability to potassium ions is higher than at rest, and the membrane potential becomes smaller than at rest. Once this step of hyper permeability calmed down, the membrane potential returns to rest. Figure I-3 describes schematically these steps.

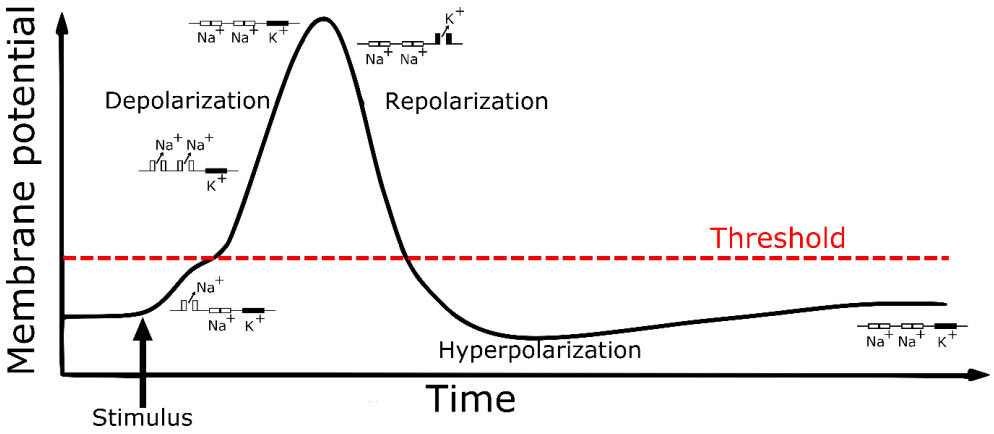

Figure I-3 The action potential is constituted by successive membrane potential changes. Inspired from R. Liljemalm [1].

I.1.3.3. Transmission of the action potentials through synapses

The action potential is a way of communication for the neurons. Figure I-4 illustrates the ability of the neurons to transmit and receive these electrical signals thanks to junctions called synapses. The dendrites are the privileged targets for synaptic input. The information transmitted through those synapses is read out at the origin of the axon. The axon then conducts the signal to the axon terminals where there is the next synaptic site. It exists two kind of synapses: chemical and electrical. The most of the time, the synapses are chemical,

but it exists also some electrical synapses. Their way of action is different and presented in Figure I-4.

When two neurons communicate through an electrical synapse, they become closer and closer to each other until the creation of a gap junction. This gap junction consists on an assembly of pairs of ion channels perfectly lined up in the membranes of the two neurons. Each pair of ion channels creates a pore through which ions may easily diffuse from the presynaptic neuron to the postsynaptic one. This exchange is considered as instantaneous.

In the case of the chemical synapses, the transmission of the action potential is a bit longer and complex. In this case, there is no junction but a small space between the two neurons called the synaptic cleft. In the presynaptic neuron, there is the presence of synaptic vesicles full of neurotransmitters. When an action potential reaches the presynaptic terminal, it induces an entry of calcium ions from the external medium to the presynaptic terminal. This causes the vesicles to fuse with the presynaptic neuron membrane and the neurotransmitters to be released in the synaptic cleft. The neurotransmitters are chemical signals acting like messengers between two neurons. After their release in the synaptic cleft, they bind to some specific receptors present on the postsynaptic neuron. It results in the opening or closing of the postsynaptic neuron ion channels and the possibility to generate an action potential or to block them (depending on the excitatory or inhibitory behavior of the neurotransmitters).

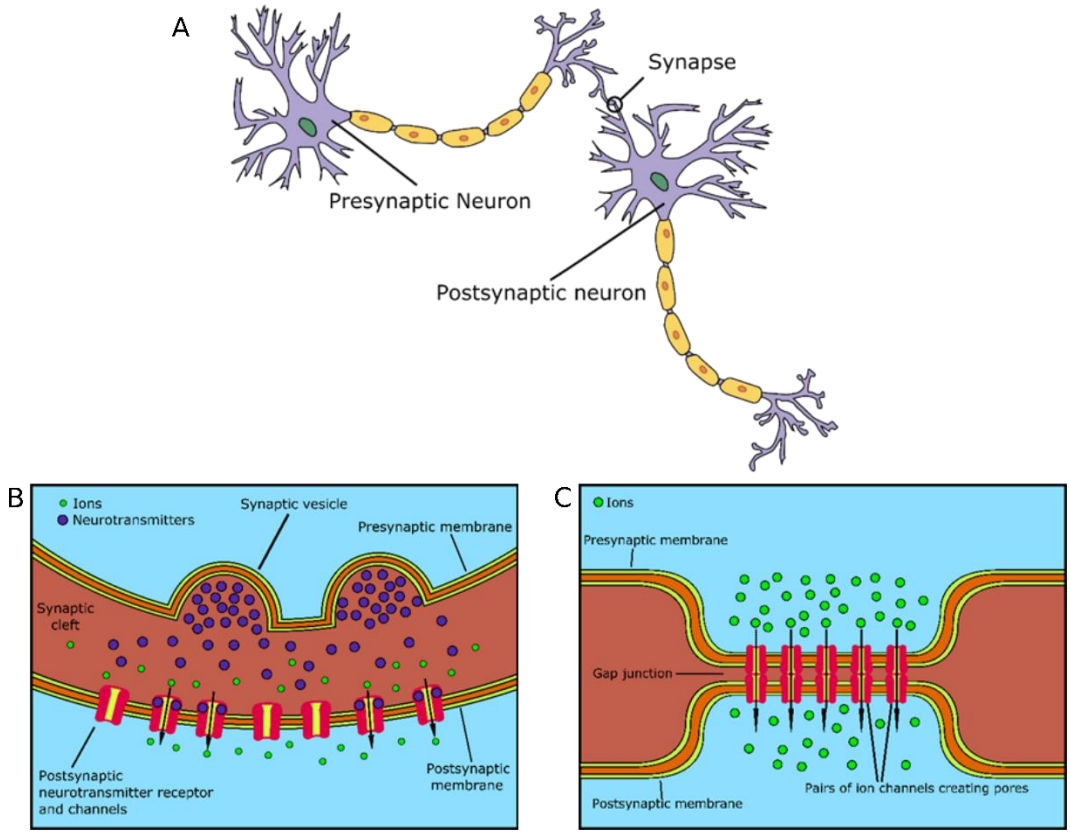

Figure I-4 Principle of the transmission of action potentials through synapses. A. Location of a synapse B. Chemical synapse. C. Electrical synapse. Inspired from D. Purves *et al*. [2].

I.2. Light tissue interactions

With the invention of the laser, the possible effect of light exposure on tissue targets took on a new approach. Many studies have been led to better understand the laser tissue interactions. Nowadays, five different kind of interactions have been identified: photochemical interactions, photomechanical interactions, photothermal interactions, photoablation and plasma induced ablation. Photoablation and plasma induced ablation rely on tissue ablation, which is not the subject of this PhD. In the following, photochemical, photomechanical and photothermal effects are detailed. Figure I-5 presents a map of the different laser tissue interactions depending on power density and duration of exposure.

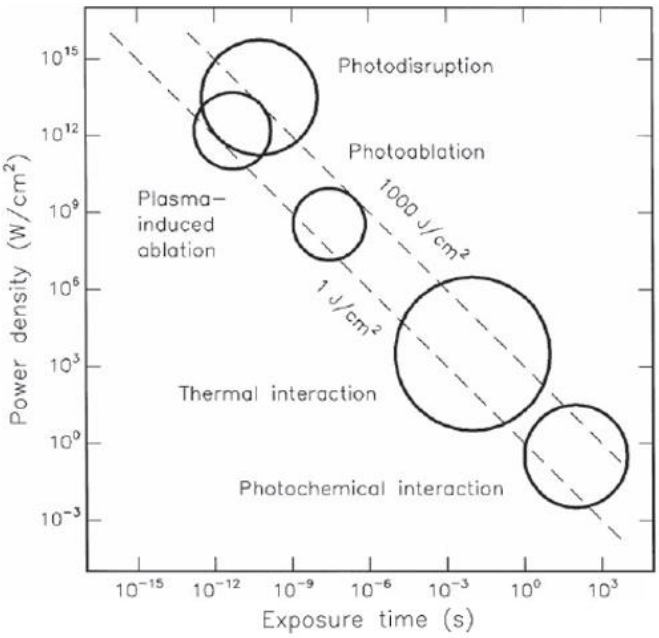

Figure I-5 Representation of a rough approximation of the exposure parameters needed according to laser tissue interaction types extracted from [3].

I.2.1. Photochemical effect

The photochemical interactions were discovered from empirical observations where light was found to be able to trigger chemical effects as well as reactions within macromolecules or tissues. The energy release due to photosynthesis is one of the best example of photochemical interactions. This interaction is characterized by the absorption of a photon by a molecular chromophore which can be endogenous or exogenous. The optical energy is consequently converted into chemical energy by the passage of the molecule to an excited state. The principle of photochemical interactions is involved in photobiology like in photodynamic therapy. In this case, an exogenous photosensitive dye is incorporated in the body and will accumulate itself in certain cells such as cancer cells. If a laser exposure is used with the appropriate wavelength, it results in the absorption of the photons by the dye which reaches an excited state. It then reacts with oxygen to generate some products like singlet oxygen which are toxic for the cell leading to their death. To reach photochemical interactions, long exposure times from seconds to continuous wave are needed with a power density about $1W/cm^{-2}$. The light used is in the visible range due to its efficiency (because of the high photon energy) but also due to their high penetration depth compared to the UV light, which has its importance in cases of deep targeted tissues.

I.2.2. Photothermal effect

Talking about the thermal interaction groups several interaction types where the change in the local temperature is the most important parameter change. The origin of this interaction comes

from a two-step process reaction between light and a targeted molecule. In a first step, the molecule passes to an excited state thanks to the absorption of a photon of the incident light. After that, this molecule will know some inelastic collisions with another molecule. The first molecule is so deactivated and simultaneously, the second one has an increase in its kinetic energy. At the microscopic level, the conversion of photo energy to kinetic energy is the origin of a temperature increase.

In biological tissues, free water molecules, pigments, proteins and other macromolecules are the main actors responsible for light absorption, the first step of photothermal interactions. This phenomenon is governed by Lambert's law:

$$I(z) = I_0 \times e^{-\alpha z} \qquad \textbf{Eq I-1}$$

Where z denotes the position on the optical axis, I_0 the incident intensity on the medium, I(z) the intensity at a distance z from the place where I_0 is considered and α the absorption coefficient of the considered medium.

The water is one of the main constituent of biological tissues. Thus, in thermal interactions, a significant role is played by water molecules absorption. Furthermore, it should be noted that the absorption coefficient depends on the wavelength of the exposed light. Those different statements lead to pay a careful attention on the absorption spectrum of water when we deal with thermal interactions.

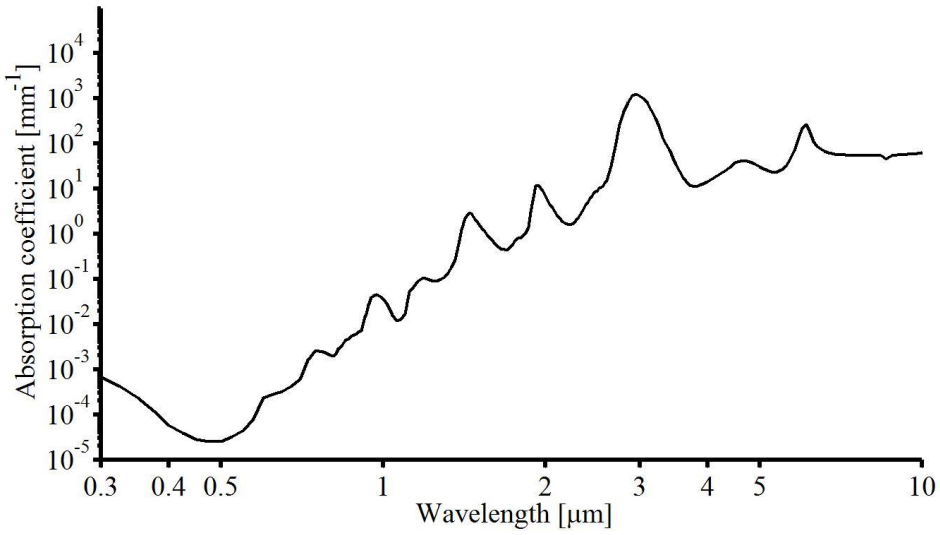

Figure I-6 Absorption spectrum of water. Data from Hale and Querry 1973 [4].

As an example of the importance of this absorption spectrum, four optical windows have been identified in biological imaging. They have been determined to make imaging in different wavelength ranges, with the lowest absorption coefficient possible to avoid thermal damages. Figure I-7, initially drew by Shi *et al*. [5], shows those optical windows related with the optical

transmission and absorbance of brain tissues. Looking on the wavelength range shows that the windows avoid the local maxima of the absorption spectrum of water.

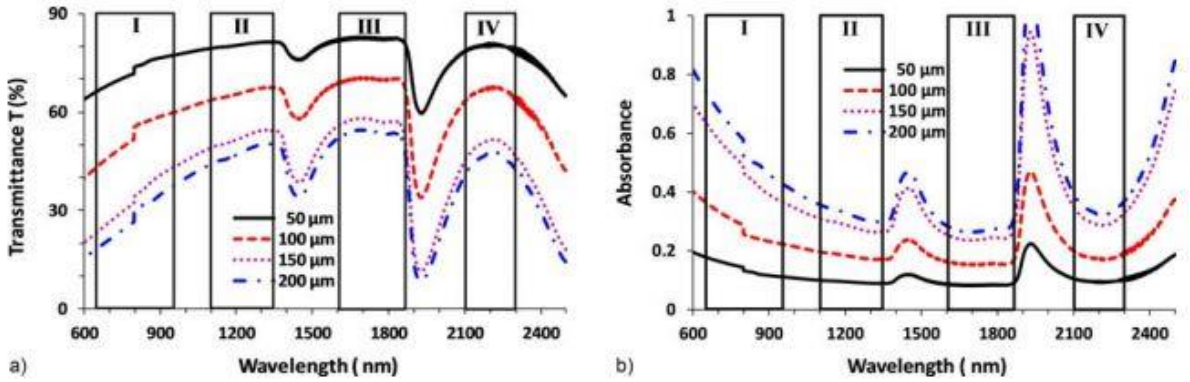

Figure I-7 Transmittance T (%) (a) and absorbance (b) in brain tissue (thicknesses were 50, 100, 150, and 200 µm) extracted from [5].

I.2.3. Photomechanical effect

The exposure of biological tissues to laser irradiation may result in the creation of stress in those tissues. This kind of interaction is described as photomechanical. The generation of transient stress waves may have several origins: a high temperature gradient induced by a fast heating is able to cause an abrupt thermoelastic expansion leading to the apparition of the stress waves. They can also be generated by a recoil which find its origin in the ejection of an ablated mass or even in a sudden expansion following a plasma generation or a phase change like the vaporization of tissue water.

I.2.4. Spatial confinement of laser tissue interactions

One of the differences between photochemical, photothermal and photomechanical effects concerns the zones of action. Photochemical effects occur only in the zone which is irradiated by the laser whereas photothermal and photomechanical interactions may be confined to the irradiated zone or may be distributed over that region because stress waves may propagate and thermal energy may diffuse. By using the optical penetration depth δ and the laser pulse duration t_p, three regimes are defined: stress confinement, thermal confinement and no confinement.

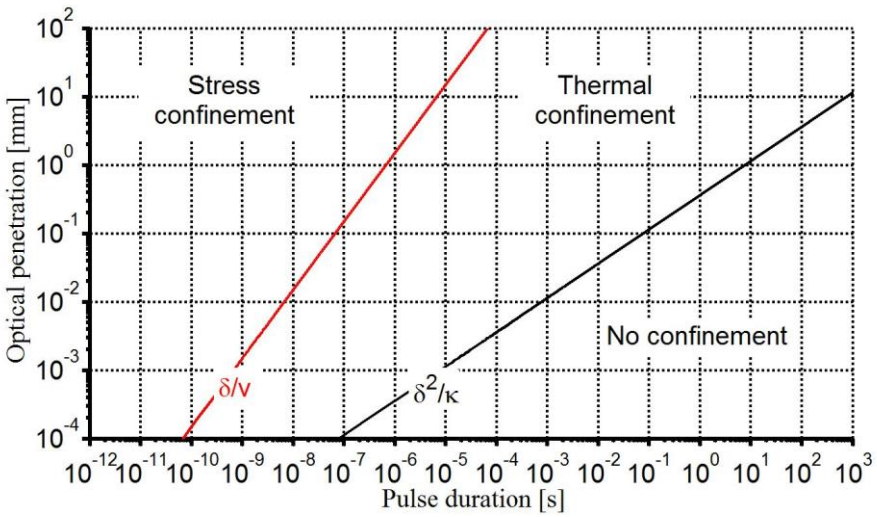

Figure I-8 Stress confinement, thermal confinement and no confinement regimes mapped in function with the pulse duration and the optical penetration depth. Graph is represented in logarithmic scale. Inspired from S. L. Jacques [6].

Stress confinement occurs with very short pulses. Actually, the pulse has to be short such as the energy is deposited in the zone before the stress waves can propagate outside of the irradiated zone. This criterion results in the accumulation of the stress induced by the laser leading to the generation of very large stress waves. To enable that, the pulse duration t_p has to respect the following criterion:

$$t_p < \frac{\delta}{v} \qquad \textbf{Eq I-2}$$

Where δ is the optical penetration and v the velocity of sound.

It should be noted that this equation may be applied only for the case where the stress is induced by thermoelastic expansion, because such phenomenon happens during the pulse. In the case where the stress is induced by recoil from ablation, it depends on the time course of this explosive phenomenon itself. This case is still under investigation.

In analogy with stress confinement, Thermal confinement happens when the laser pulse is enough short to make the energy to be deposited in the irradiated zone before the thermal energy may diffuse out of that region. This results in the accumulation of the heat and in the achievement of high temperature. To enable that, the pulse duration has to respect the following criterion:

$$t_p < \frac{\delta^2}{\kappa} \qquad \textbf{Eq I-3}$$

Where κ is the thermal diffusivity ($\kappa \approx 1.3*10^{-3}$ cm^2/s).

No confinement occurs when the pulse duration is not enough short, allowing the stress and thermal energy to diffuse out of the irradiated area before the energy of the pulse is delivered.

In such case, any effect will concern a larger volume. That means that the laser energy threshold is greater and the possible injuries will also concern a greater volume.

To be in no confinement regime, the pulse duration has to respect the following criterion:

$$t_p > \frac{\delta^2}{\kappa} \qquad \textbf{Eq I-4}$$

Consequently, when an optical exposure is performed on tissue, the choice of the laser parameters has to be carefully made. The combination of the duration of the pulse, the excitation wavelength and the energy delivered have an impact of the potential zone of effect and damages. To be spatially selective to the zone of exposure requires the need to be in the stress or thermal confinement regimes according to the desired effect.

I.3. Neural stimulation methods

I.3.1. Electrical stimulation

The stimulation of a neuron consists in applying an external energy to initiate the generation of action potentials. Traditionally, studying the cells or modifying the nerve cell function during clinical procedures is made by using electrical methods. Electrical stimulation is a powerful tool for neurostimulation with many clinical applications. The electrical stimulation is the most used method to initiate action potentials. When an electrical signal is applied, it results in a change in the membrane potential due to the electrical charge created reorganizing the charges in the proximity of the outer plasma membrane of the cell. The stimulation threshold of the membrane potential is then reached, as presented in Figure I-3, and the action potential initiated. Despite the numerous clinical applications of electrical neuroprostheses, even in the brain to treat Parkinson's disease for example [7], [8], electrical stimulation suffers from several limitations. In most of the applications, the neurons stimulated are not only those immediately adjacent to the electrodes. The electrical stimulation affects also the cells close to the region where the electric field is applied in a spatially decaying fashion. To stimulate a single cell, the electrodes should be placed very close to the neuron or impale the neuron. There is consequently a problem of spatial selectivity if we want to avoid to be too much invasive in the immediate region surrounding the targeted cell. The invasiveness of the method is also a problem because the electrodes have to directly surrender the region where the stimulation is desired. Another existing problem is the presence of electrical artifact when the stimulation is made in the same time that electrophysiology recording. Optical stimulation of neurons has been identified as a way to avoid some of the problems existing with electrical stimulation.

I.3.2. Optical stimulation using optogenetics

Neural stimulation is also possible through an exposure of the cell to an optical radiation combined with the use of genetic manipulations. Here, the principle requires light-gated ion channels like Channelrhodopsin. Light-gated ion channels are transmembrane proteins that form ion channels and may be activated by light. Channelrhodopsin proteins are transfected in the targeted cells and then activated by the exposure to blue light inducing the neurons firing. Boyden and coworkers in 2005 showed that blue light train pulses could evoke action potential by increasing the expressed channelrhodopsin-2 currents, transfected in hippocampal neurons [9]. This kind of stimulation is more selective spatially than the electrical stimulation since only the neurons illuminated and expressing the transfected proteins are depolarized. Using optogenetics, brain functions modulation by specific neurons have been studied [10]–[13]. A more recent study showed the possibility to apply optogenetics in clinical cases. Indeed, in the non-human primate brain (rhesus macaque), Channelrhodopsin-2 was used to activate neuron specific type [14]. The efficacy and the safety of the method were proved, without provoking neuron death or functional immune reactions. The most important limitation of this method remains the need to transfect the proteins sensitive to the light in the targeted cells. According to the opsin channels used, excitation light may be in the UV or visible range.

I.3.3. Optical stimulation using infrared radiation

The infrared neural stimulation is another recent tool to stimulate the neurons. Here the principle is to expose the biological target to infrared radiation. The infrared radiation interacts directly with the targeted tissue. In most of the studies carrying out infrared neural stimulation, the infrared radiation is delivered to the targeted tissue through an optical fiber. It thus allows a good flexibility and handling in the choice of the location of the targeted area. Neural activity induced by infrared exposure is highlighted with different methods, starting with electrophysiology, allowing to see action potentials using two electrodes, calcium imaging as well as other particular responses specific to the targeted neurons are also used.

It presents the same advantages than optogenetics compared to the electrical stimulation. It presents a good spatial selectivity and an invasiveness decreased compared to the electrical stimulation because there is no electrode. Consequently no contact is needed between the energy source and the targeted tissue. Furthermore, it is artifact free and compared to the optogenetics, there is no need to use genetic modification due to the direct interaction between the infrared radiation and the biological tissue. Infrared neural stimulation, which constitutes the main subject of the research work presented hereafter, is more precisely presented in the next part.

I.4. Infrared neural stimulation

I.4.1. First demonstration of infrared neural stimulation

The ability to stimulate neurons with infrared laser light was first performed by Wells and colleagues in 2005 [15]. To show this ability and to prove the concept, they compared compound nerve action potentials (CNAPs) and compound muscle action potentials (CMAPs) obtained using infrared stimulation and electrical stimulation. Compound action potentials are defined as a group of almost simultaneous action potentials from several muscle or nerve fibers located in the same area. This experiment was performed *in vivo*, on the sciatic nerve of a rat. As a result, see Figure I-9, a strong similarity in terms of shapes and response timing were found. Furthermore, when they increased the incident infrared energy, they saw that the amplitudes of both CNAPs and CMAPs responses were increased. This point is consistent with the dependence between the strength of the electrical signal and the response in classical electrical stimulation. Thus, this result has validated the concept of infrared neural stimulation. Then, they tested if the action potential produced was physiologically conducted by synapses. To do that, a neuromuscular blocker was used to block the synaptic connections between the nerve stimulated and the muscle. As a result, the CNAP was still present but the CMAP was loss, meaning the muscle activity was loss. This is the confirmation that the action potential was initiated in the nerve before to be transmitted to the muscle through synapses.

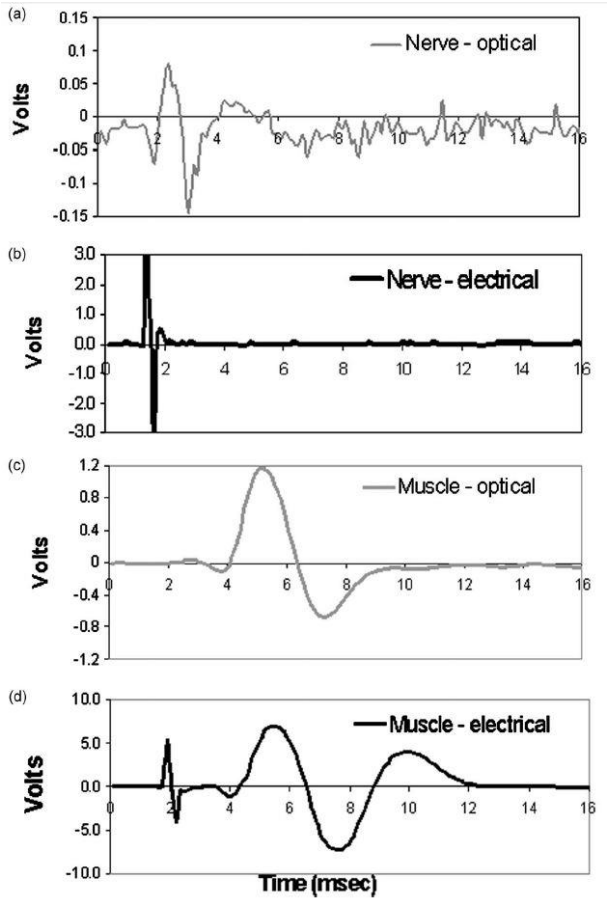

Figure I-9 Comparison of compound muscle and nerve action potentials induced by electrical and optical stimulation [15].

Stimulation and ablation thresholds were determined for six different wavelengths: 2.1, 3.0, 4.0, 4.5, 5.0 and 6.1 µm. By doing Fourier transform infrared spectroscopy, they also evaluated the absorption of the tissue for those different wavelengths. From that, they highlighted the dependency of the thresholds on the wavelength of stimulation and more precisely on the absorption coefficient. Both of the threshold increased with the decrease of the absorption coefficient. The safety ratio was also found to be greater for shorter absorption coefficients.

I.4.2. Infrared stimulation in the peripheral nervous system

The peripheral nervous system, constituted of all the nerves in the body except the brain and the spinal cord, is responsible of numerous diseases like the loss of the ear, of the balance, of the ability to move facial nerve… It is also a target easier to reach than the central nervous system. Thus the main part of the studies led about infrared neural stimulation were applied on the PNS.

I.4.2.1. Spatial selectivity of the infrared neural stimulation

The auditory nerve was used to demonstrate the spatial selectivity of the infrared neural stimulation. Izzo and coworkers [16] stimulated the gerbil auditory system by three different

ways: optical radiation, acoustic tones and electric current. The optical fiber was directed to the basal turn of the cochlea, where the electrodes were inserted in the case of electrical stimulation. They used immunohistochemical staining for the c-FOS protein allowing to reveal the spread of excitation in each case. c-FOS is a gene which is expressed in response to membrane electrical signals in neurons. As a compelling result, c-FOS expression was found to be directly in the beam path in the case of optical stimulation, whereas electrical stimulation resulted in the gene expression in all the turns of the cochlea in the tissue section probed. Other studies in the guinea pig cochlea [17] and in the gerbil cochlea [18] confirmed the spatial selectivity of the infrared neural stimulation.

I.4.2.2. Safety of the infrared neural stimulation

Another point of interest studied in the auditory system is the safety of the method. The main source of concern is the risk to damage the tissue by the thermal transients and the accumulation of thermal energy induced by the absorption of the infrared radiation. During 6 hours, the gerbil auditory system was continuously stimulated and the compound action potentials resulting were measured [19], [20]. The neuron damage would be expected to be translated by a decrease in the amplitude of the compound action potentials. As a result, the amplitude was found to remain pretty stable, leading to the conclusion that there was no damage induced by INS with the optical parameters used. In another study where the repetition rate used was far higher than the ones used usually, the damage thresholds were performed in guinea pig cochlea [21]. Here, the stimulation was during up to 5 h continuously. If the amplitude of the compound action potential did not decrease more than 25 % compared to the baseline, the stimulation was considered damage free. With a high repetition rate compared to other studies (250 Hz), no damage was found for radiant exposure of 25 µJ/pulse or lower. Above that value, damages were stronger with higher radiant exposures.

I.4.2.3. Chronic application of infrared neural stimulation

A More recent study performed with success the first chronic application of INS in the cat auditory system [22]. Here, an optical fiber was implanted and connected to a miniaturized and battery-powered stimulator. The laser exposure parameters were fixed at a wavelength of 1850 nm, consisting in 100 µs pulses at a repetition rate of 200 Hz and the pulse energy at the tip of the fiber was 12 µJ/pulse. With such parameters they performed chronic stimulation for 4-8 hours/day for up to 30 days. The laser and the stimulator were placed in a pocket of a jacket that the cat wore. The optically evoked auditory brainstem responses were obtained and suggested that the brain received neural input from INS of the spiral ganglion neurons. Further, the cats exhibited a behavioral response to the optical stimulus. Following the start of the stimulation and so of the laser activation, an increase in the numbers of head turns between

300 % and 1200 % was seen. This increase was to the side of the implant, as if the cat was looking for the source of a sound. However, this work is not sufficient to conclude whether the animals did hear a sound or not. The results are still promising to develop INS-based neuroprostheses applicable to the human.

I.4.2.4. Review of the other nerves targeted by the infrared neural stimulation

Another target for INS is the vestibular nerve, main actor of the balance of the body. In 2009 [23], the comparison between electrical and optical stimuli (λ = 1842 nm) was made on the guinea pig VIIIth nerve, facial nerve, or the ampullae of the superior and lateral semicircular canals. Although both stimuli successfully triggered compound action potentials from the nerve stimulated, a difference was observable in ampullae stimulation. Electrical stimulation resulted in eye movement, which was not the case with optical stimulation. Further work has been performed on the semicircular canal crista ampullaris of the toadfish [24], the toadfish being a well-established animal model for the vestibular physiology [25]. According to Zhao *et al.* [26], the results obtained in the toadfish were confirmed in the chinchilla [27]. All of those studies demonstrated the ability of the INS to trigger responses in vestibular nerves. However, the responses induced are a mix of excitatory, inhibitory, and mixed responses from canal afferents, and the ability of INS to trigger significant vestibule-ocular reflex eye movement response remains unclear.

The ability to stimulate the gerbil facial nerve has also been investigated [28]. The facial nerve ensures the motor control of facial expression muscles. The comparison between the responses between electrical stimulation and INS at 2120 nm led to find similar action potentials qualitatively and quantitatively. Spatial selectivity of INS was here demonstrated by the stimulation of single nerve bundles within the trunk when it is not possible with electrical stimulation. The stimulation threshold was found to be 0.71 J.cm^{-2} and 0.88 J.cm^{-2} respectively for the nerve trunk and the nerve branches. No histologically identifiable damages of the nerve were found for exposures up to 2 J.cm^{-2}.

The last *in vivo* target of the peripheral nervous system found in the literature is the cavernous nerve, which facilitates penile erection. As for the other targets, the ability of INS to stimulate cavernous nerves was investigating by comparing responses triggered by electrical and optical stimulation. In this case, the responses compared are the intracavernosal pressures induced by both type of stimulation. Fried and coworkers [29], [30] optimized the laser parameters and obtained similar intracavernosal pressures in magnitude and duration for electrical stimulation and INS. However, the stimulation of the rat cavernous nerve is easier than the human cavernous nerve. Indeed, there is a thin fascial layer over the human cavernous nerve which is not present in the rat. To be closer of the human model, testicular fascia layers with different

thicknesses were transplanted over the rat cavernous nerve before stimulation with continuous wave diode laser [31]. When the layer thickness was increased, the necessary power for successful stimulation was also increased, with the need of 40 mW for 150-160 µm layer and 53 mW for 360-380 µm. For layer's thicknesses of 500-600 µm, no successful stimulation was achieved. The results were correlated with a previous study [32] using other wavelengths and reported in Table I-1 where ICP denotes the intracavernous pressure and OPD the optical penetration depth.

Table I-1 Comparison of optical nerve stimulation threshold parameters of surface and subsurface rat cavernous nerve in function with the wavelength. Reproduced from Tozburun *et al*. [31].

Wavelength (nm)	**1455**	**1490**	**1550**
Absorption coefficient in water (cm^{-1})	29.1	19.3	10.7
OPD in water (µm)	344	518	935
Power to surface stimulation (mW)	28.3 ± 5.2	38.8 ± 5.2	55.0 ± 4.1
Threshold ICP response time (s)	12.7 ± 1.0	12.6 ± 1.4	13.6 ± 1.6
Fascia thickness (µm)	100 – 110	360 – 380	420 - 450
Power to subsurface stimulation (mW)	45	53	80
Threshold ICP response time (s)	13.7 ± 0.7	10.4 ± 1.8	13.1 ± 0.5
Sample size (N)	9	8	8

The critical aspect of the selection of the wavelength is here well demonstrated. For thicker layers, the need of a wavelength with better optical depth penetration is highlighted. The compromise is that a greater input power is required to achieve stimulation. To prevent for possible thermal damage, a prototype of temperature controlled optical nerve system was tested [33]. The system maintained the temperature with a precision of +/- 1 °C from the set value. The efficacy of the system was proved and the temperature could be maintained at a constant value of temperature, suitable for safe INS.

I.4.3. Infrared stimulation in the Central nervous system

A few studies showed also the successful application of INS in the central nervous system. Stimulating the central nervous system, and the brain more particularly, remains a challenge since it's hard to reach spatially and it is the location where numerous of neurodegenerative diseases take their origin as Alzheimer's, Parkinson's, multiple sclerosis… The first *in vivo* experiment was led in the rat somatosensory cortex using a radiation emitting at 1875 nm [34]. To detect the effect of INS, intrinsic signal optical imaging was used. The optical responses to

INS were found to be very similar to the responses obtained by natural tactile stimulation, showing the ability of INS to stimulate the somatosensory cortex. The optical imaging also revealed that the region of effect was approximately 2 mm in diameter. It shows that, as for stimulation in the PNS, the cortex stimulation by infrared radiation remains spatially selective. They also observed an increase in the amplitude of the intrinsic response when the radiant energy is increased. Increasing directly the radiant energy of the laser resulted in a linear response in peak signal magnitude when an exponential trend is found with the increase of the repetition rate. However, the electrophysiological recordings revealed that INS induced a reduction in the firing rate of the neurons. This work is the first work demonstrated INS causing neural inhibition. A possible explanation is that inhibitory neurons may have been stimulated in the superficial layers of the cortex. No damage in the cortex was highlighted even after more than 2 h of exposure to infrared radiation. In the same way, the ability of INS to stimulate the primary visual cortex of macaque monkeys was investigated [35]. Here again, increasing the radiant exposure resulted in an increase in the optical intrinsic signals. In this work, contrary to the precedent work, INS was found to evoke excitatory responses. It was found that INS could modulate visual responses in an eye-specific manner. Three different optical fiber diameters were used: 100 µm, 200 µm and 400 µm. With the two smaller diameter, INS enhanced the response of visual stimuli when the larger one induced a relatively suppressed response.

I.4.4. Infrared stimulation *in vitro* and in non-neural cells

Other studies have been led to see the effect of INS in other targets *in-vitro* or in non-neural targets. Wininger and colleagues showed by comparing electrical and infrared stimulation responses that the leg nerve of lobsters may be successfully stimulated thanks to INS [36]. The response of the optical stimuli were a bit smaller and and they found a thermal damage. They made the hypothesis that invertebrates like lobsters may be more susceptible to thermal damage due to the increased water content. Unfortunately, the spot size and the energy delivered to the nerve were not reported.

A more recent study in acute mammalian brainstem slices revealed that infrared exposure may result in evoking inward currents in individual neurons with low power densities [37]. They also showed that such events were accompanied by an increase in the synaptic activity. This is the first work revealing an increase in the synaptic activity induced by INS.

Other studies investigated the possibility to stimulate cardiomyocytes with INS. By applying pulsed infrared light, visible contractions were found synchronized to the periodic application of laser light [38]. Optical pacing was performed on adult rabbit heart with a laser diode emitting at 1851 nm [39]. The synchronization between laser stimulation pulses and the heart rate was

here again demonstrated. Further, it was found that the pacing frequency modulated the heart rate response. In the future, optical pacing may provide a good tool to replace conventional electrical pacing or in cardiology, to modulate the heart rate.

I.4.5. Electrical and Infrared costimulation

Duke *et al*. explained a method to decrease the stimulation threshold [40]. By targeting sciatic nerves of rats, they confirmed the hypothesis that the delivery of a subthreshold electrical stimulus, concurrently with infrared stimulation, decreased the required optical energy per pulse to achieve stimulation. Thus they demonstrated proof of concept for a combined electrical/optical nerve stimulation. A significant aspect of the results they obtained, is that the reduction of infrared neural stimulation threshold for a given subthreshold electrical stimulus does not follow a linear trend. This implies that electrical stimulation and INS do not function by the same mechanism. In their work they presented the following logarithmic relationship based on their results:

$$O = 0.22\, ln(1 - E) + 1 \qquad \textbf{Eq I-5}$$

Where O is the optical energy (% INS threshold), and E is the magnitude of the electrical stimulus (% electrical stimulation threshold).

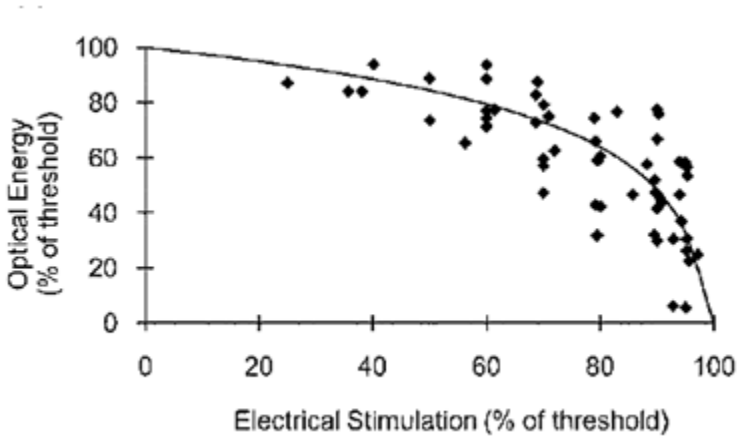

Figure I-10 Evolution of the optical threshold in function with the electrical threshold when combining electrical and optical stimulation [40].

For instance, according to the equation, if the electrical stimulus is applied at 95% of the electric threshold, it induces that the optical threshold will be reduced by a factor nearly 3. They also explained in this work that this reduction in optical threshold significantly increases the window for safe INS, since less energy is required to stimulate, thereby reducing the heat induced in the tissue. They finally reported that the spatial selectivity of INS is maintained and that the greater benefit is achieved when the electrical and optical pulses are delivered simultaneously. A further work [41] showed that there is a finite region of excitation between the cathode and

the anode where costimulation is possible. This region, close to the cathode, increased when increasing the radiant exposure of the infrared light. During long period of stimulation, it was found that the threshold of the hybrid stimulation varied, in accordance to the threshold of the electrical stimulation. When the electrical stimulation threshold decreased, the response to optical stimuli decreased. This negative correlation proves once more that both of the stimulation does not exhibit the same underlying mechanism.

I.4.6. Underlying mechanism

Infrared neural stimulation efficiency has been demonstrated in many studies, on a wide variety of targets. However, its underlying mechanism is not fully elucidated and remains a field of interest. Different works attempted to identify this mechanism leading to the consideration of a few hypotheses.

I.4.6.1. Photothermal mechanism

Wells and colleagues, with a study on the rat sciatic nerve, identified that the effect was likely photothermal, considering the high absorption coefficient of water for the wavelengths used for typical INS [42]. They excluded photochemical interactions due to low energy of infrared photons, and did not believed in the photomechanical effect since the pulses durations are too long to allow stress confinement. They also made the hypothesis that heat sensitive ion channels may be involved. Following this hypothesis, by measuring changes in intracellular Ca^{2+} concentration evoked by INS, Rhee and colleagues showed that temperature-sensitive Transient Receptor Potential mediated the calcium transients in the rat vagus nerve [43]. More precisely, they identified the Transient Receptor Potential Vanilloid 1 (TRPV1) ion channel as the main responsible of the responses observed, since the use of capsazepine, a highly selective TRPV1 antagonist reduced significantly the calcium transients. The involvement of this ion channel is supported by the work of Suh and colleagues where it was not possible to stimulate TRPV1 knockout mice auditory nerves whereas all control animals were successfully stimulated [44]. A further study by Albert *et al*., revealed a similar role for TRPV4 channels. INS was here used to stimulate both retinal and vestibular ganglia [45]. The laser-evoked neuronal voltage variations measured were completely abolished in both cell types by the use of Ruthenium Red, a general TRPV channel blocker or by the use of RN 1734, a specific TRPV4 channel blocker. It should be noted that the cells used here were found to not express TRPV1 channels, making them not essential for successful INS. The follow-up study [46] highlighted the absolute temperature as the key parameter more than the rate of heat. To elicit action potentials, the laser parameters used induced an increase of temperature from 22 °C, the room temperature, to 55-60 °C. This result confirmed the potential involvement of heat-sensitive ion channels like TRPV channels.

However, INS application in the rat dorsal root and nodose ganglia disagree with previous works [47]. The responses observed do not match with TRPV1 because of their limited expression in such neurons. Further, this work resulted in the observation of reversal potential values going from - 20 to - 55 mV, which does not correspond to non-selective TRP cation channels. Rather, this range suggests that the infrared light interacts with more than one ionic channel.

I.4.6.2. Electrostatic mechanism

A different mechanism for INS was proposed where the fast heating due to infrared water absorption would influence membrane capacitance [48]. The change in the membrane capacitance would involve a modification of the membrane potential which would be sufficient to initiate action potentials. With electrophysiology, they demonstrated the shift of the capacitance in Xenopus oocytes, human embryonic kidney cells (HEK) and artificial lipid bilayers. With such a mechanism, the basic electrical properties of the plasma membrane is the primary interest, there is no need of ion channels. They demonstrated that the current response triggered by this electrostatic mechanism depends on the temperature gradient and not on the value of the temperature itself. A simulation study investigated the possibility of this theory [49]. The results indeed showed that membrane capacitance changes may happen consequently to the INS, but with typical INS parameters, the necessary change to activate an axon is not reached.

I.4.6.3. Intracellular effect

Previous works considered effects occurring at the level of the plasma membrane. A study led in cardiomyocytes showed the evidence of an intracellular effect triggered by the infrared exposure [50]. They revealed that the infrared induced Ca^{2+} transients were of mitochondrial origin, since the pharmacological inhibitor of the mitochondrial Na^{+} / Ca^{2+} exchanger (CGP-37157) attenuated the IR response.

With all of those studies, the underlying mechanism of INS remains unclear. Understanding the effect of INS on the plasma membrane or on intracellular signal is still a challenge to elucidate.

I.4.7. Review of the Infrared laser parameters used for INS

Table I-2 presents the different laser parameters of INS used in the studies reviewed in this chapter. The biological target, the excitation wavelength (λ), the infrared pulse duration (t_p) as well as the repetition rate (RR), the fiber diameter (Φ fiber) and the energy delivered (E) are reported. It should be noted that the infrared pulse duration represents the duration of exposure of the targets to infrared and the repetition rate is the frequency of repetition of the exposures.

Consequently, those reported parameters are not necessarily corresponding to the pulse durations and the repetition rates of the laser used itself. According to the works reviewed, the energy is not expressed in the same units. Some prefer to use radiant energies, other the amount of energy per pulse or even the laser power. Furthermore, those works express the energy delivered either on the targeted tissue, in agreement with the spot size on the target, or at the fiber tip. Consequently units are expressed in the table itself, and an asterisk is added when the radiant exposure refers to the value delivered on the cell in agreement with the spot size on the target. It should be noted that in some references, this parameter is not explicitly given.

Table I-2 Biological target and optical parameters used to perform INS in some of the different works reviewed in this chapter. Asterisks denote when the radiant exposure refers to the value delivered on the cell in agreement with the spot size on the target.

Target	λ (µm)	t_p (ms)	RR (Hz)	Φ fiber (µm)	Energy	ref
Gerbils auditory system	2.12	0.35	2	100	60 mJ.cm^{-2}	[16]
Guinea pig cochlea	1.86	0.1	10	200	0 - 127 µJ/pulse	[17]
Gerbil cochlea	1.86	0.02	2	200	10-20 mJ.cm^{-2}	[18]
Gerbil auditory system	1.840 - 1.873	0.035 - 1	2 13	200	1-100 mJ.cm^{-2}	[20]
Gerbil auditory system	2.12	0.25	2	100	10-100 mJ.cm^{-2} *	[19]
Guinea pig cochlea	1.869	0.1	250	130	0 - 127 mJ/pulse	[21]
Cat auditory system	1.85	0.1	200	-	12 µJ/pulse	[22]
Mice auditory nerve	1.85 – 1.86	0.03 -1	10	200	0.03 – 0.7 J.cm^{-2}	[44]
Guinea pig vestibular nerve	1.84	1	-	300	2 mJ/pulse	[23]
Toadfish hair cells	1.862	0.2 – 0.75	1 - 200	200 or 400	122 – 1107 µJ/pulse	[24]
Rat vestibular and mice retinal ganglion	1.875	7 – 10	-	105	20 - 60 J.cm^{-2}	[45]
Rat vestibular and mice retinal ganglion	1.47 1.535 1.875	7 – 10 – 20	1 – 2 – 10	105	430 mW 410 mW 230 mW	[46]
Gerbil facial nerve	2.12	0.25	2	600	0.71-1.77 J.cm^{-2}	[28]
Rat cavernous nerve	1.850 - 1.889	2.5	5 - 20	400	0.09- 0.86 J.cm^{-2} *	[29]
Rat cavernous nerve	1.49	15 000	-	-	0.45 – 1.35 J	[31]
Rat cavernous nerve	1.455- 1.550	15 000	-	9	0.5 – 1.35 J	[32]
Rat cavernous nerve	1.455	30 000	-	9	6.4 W.cm^{-2}	[33]
Rat sciatic	2.1 – 6.1	0.25	2	600	0.3 - 0.7	[15]

nerve					$J.cm^{-2}$ *	
Rat sciatic nerve	2.12	0.35	2 - 5	600	0.3 - 1 $J.cm^{-2}$ *	[42]
Rat sciatic nerve	1.875	2	2	400	0.6 – 1.69 $J.cm^{-2}$ *	[40]
Oocytes or HEK cells	1.889 1.869	0.1 – 10 0.2 - 1	-	400 600	0.3 – 7.9 0.7 - 3.7 mJ/pulse	[48]
Rat nodose ganglions	1.85	2 – 20	10	200	5 W peak power	[43]
Rat brainstem slices	1.89	1000	-	14	261 $J.cm^{-2}$ *	[37]
Rat somatosensory cortex	1.875	0.25	50 – 200	400	0.01 – 0.55 $J.cm^{-2}$ *	[34]
Macaque primary visual cortex	1.875	0.075 – 0.3	100 - 200	100 200 400	0.5 – 1.3 $J.cm^{-2}$	[35]
Rats cardiomyocytes	780	$80*10^{-12}$	$82*10^{6}$	No fiber	15 – 30 mW	[38]
Rats cardiomyocytes	1.862	3 – 4	0.25 – 1	400	9.1 – 11.6 $J.cm^{-2}$	[50]
Adult rabbit heart	1.851	2.5 – 12	2.5 – 3.3	400	6.3 – 11.8 $J.cm^{-2}$ *	[39]
Lobster leg nerves	1.856	0.2 – 2	0.5 – 1	600	-	[36]

I.5. Local Temperature measurement

During the infrared neural stimulation, the temperature change induced by the absorption of the infrared radiation by the water in the tissue is one of the primary concern. The intracellular temperature regulates also cellular functions, it governs the dynamics and the reactivity of many biomolecules inside a cell. Measure the temperature at the cellular level is consequently a necessity in the investigation of the infrared neural stimulation mechanism and for its safety.

To measure the temperature at the cellular level, several microscopy techniques have been developed. Europium (III) thenoltrifluoro-acetonate (Eu-TTA) thanks to its temperature–dependent phosphorescence intensity was used to make thermal imaging in Chinese hamster ovary cells [51]. The technique was spatially limited by the diffraction and the time resolution was sampling-rate-limited. The Eu-TTA intensity was found to be temperature dependent between 15 °C and 40 °C. However this technique is limited by the toxicity of Eu-TTA and the differential uptake and repartition into organelles and membrane. A fluorescent nanogel thermometer was developed with a relatively good biocompatibility [52]. They estimated their thermal resolution to 0.29 - 0.5 °C but for a relatively small temperature range (27 °C – 33 °C). According to their calibration curve, the temperature sensitivity is pretty good in this range but becomes much less important outside of it. It is also potentially toxic for a cell, and limited in the time scale resolution. The ability of fluorescence lifetime imaging microscopy (FLIM) of both fluorescent gold nanoclusters [53] or fluorescent polymeric thermometer [54] to measure

temperature have been proved. Although the temperature resolution of those two studies were respectively 0.1 – 0.3 °C and 0.18 – 0.58 °C, FLIM is also known to be sensitive to viscosity and pH. Submicrometer thermocouples inserted in the cytosol of the cell have also been proposed [55]. The cytosol temperature may be measured in real time with a good accuracy but the insertion of a physical object in a cell may compromise its integrity. The transfection of Escherichia coli bacteria with a temperature sensitive vector was also tested [56]. The temperature vectors express increasing quantities of β-galactosidase (LacZ) in response to temperature increase. The heating of individual bacteria was monitored by the detection of LacZ expression. Nonetheless, this method is slow for real time measurements and dynamic temperature measurement are not possible because of the lack of reversibility. Another highly promising technique is based on the anisotropy of fluorescence from green fluorescent protein [57]. The problem is that the cell lines in which we want to measure the temperature have to stably express the proteins. Neurons or primary tissues are difficult to transfect, making this method difficult to apply in such targets. Other methods using luminescent Ru(bpy)32+-doped silica nanoparticles [58], quantum dots [59], [60] or Er3+ nanoparticles [61] have been demonstrated, but the toxicity of these substances has to be taken into account.

I.6. Assessment of Neural activity with fluorescent calcium probes

Measuring the changes of intracellular calcium concentration is an excellent way to see neural activity [62]. Calcium indicators may be fluorescent or bioluminescent. In the following, we are interested in the fluorescent calcium probes. A fluorescent calcium probe allows to make dynamic measurement of free Ca^{2+} concentration. The probe is constituted by a part able to fix specifically Ca^{2+} ions, like Ca^{2+} chelators (BAPTA or EGTA), associated to a chromophore. An important parameter of Ca^{2+} probes is the dissociation constant defined thanks to the following reaction.

$$\mathrm{Ca}^{2+} + \mathrm{probe} \rightleftarrows \mathrm{Ca}^{2+}\mathrm{probe}$$

The dissociation constant is defined as:

$$\mathrm{Kd} = \frac{[\mathrm{Ca}^{2+}] \times [\mathrm{probe}]}{[\mathrm{Ca}^{2+}\mathrm{probe}]} \qquad \textbf{Eq I-6}$$

The relation between the Ca^{2+} concentration $[Ca^{2+}]$, the dissociation constant Kd and the fluorescence F follows a sigmoidal pattern:

$$[\mathrm{Ca}^{2+}] = \mathrm{Kd} \times \frac{(F - F_{min})}{(F_{max} - F)} \qquad \textbf{Eq I-7}$$

Where F_{min} is the fluorescence without any calcium, F_{max} is the fluorescence with calcium at saturation. Figure I-11 shows this relationship with the trace of the relative fluorescence of two fluorescent probes (Fluo-4 and Fluo-4FF) in function with the pCa. The pCa is defined as:

$$pCa = -log_{10}([Ca^{2+}])$$ **Eq I-8**

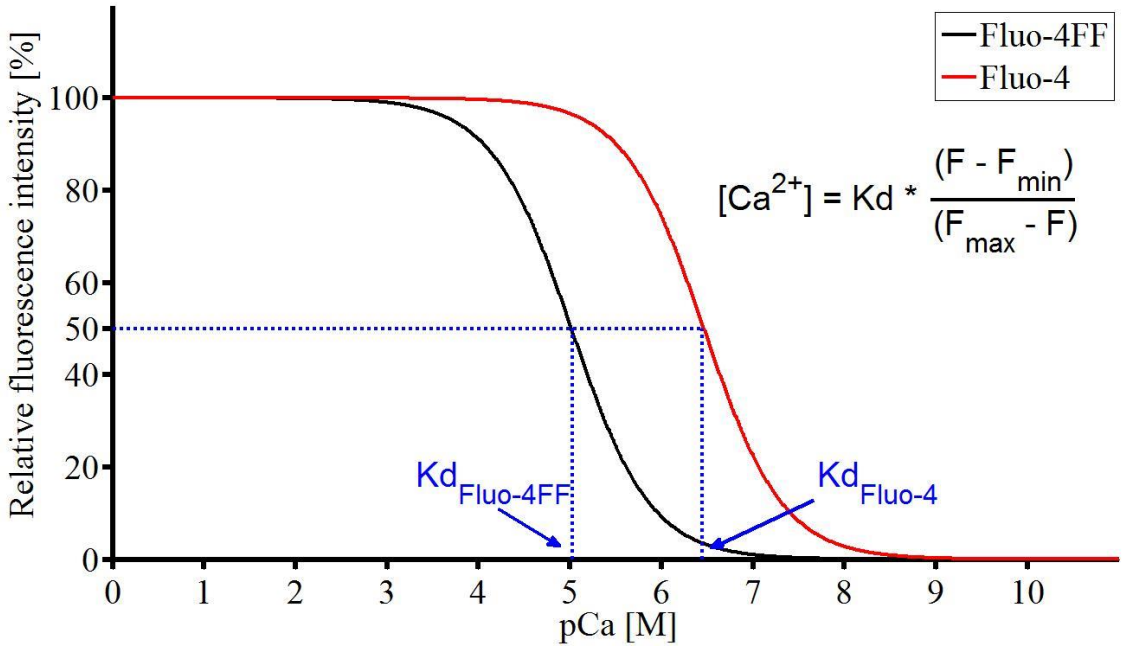

Figure I-11 Evolution of the relative fluorescence intensity in function with the pCa for Fluo-4 and Fluo-4FF.The Ca^{2+} concentration [Ca^{2+}], the dissociation constant Kd and the fluorescence F follows a sigmoidal pattern.

The dissociation constant is defined as the Ca^{2+} ion concentration when the fluorescence value is the half of the maximal fluorescence, when the Ca^{2+} ion concentration is at saturation for the probe. If we consider the two previous curves related to Fluo-4 and Fluo-4FF fluorescences, it is obvious that the two probes are able to measure Ca^{2+} concentration in different ranges. According to the previous graph, with a Kd of 345 nM, Fluo-4 allow to detect Ca^{2+} concentration from approximately 39 nM to 3.16 µM (corresponding respectively to 10 % and 90 % of the maximal fluorescence). This range is for instance adapted to see Ca^{2+} concentration changes in the cytosol. With a Kd of 9.7 µM, Fluo-4FF allow to detect Ca^{2+} concentration from 1 µM to 89 µM.

The first fluorescent calcium probes were synthetized in the 1980s with the creation of Quin-2. It is composed of a Ca^{2+} chelator (EGTA or BAPTA) associated with a fluorophore. His Kd of 114 nM allowed to probe the weak variations of intracellular calcium ions concentrations. When a calcium ion is bounded to the probe, it results in a change in its fluorescence intensity. However this probe has been quickly abandoned for many reasons. The excitation was made in the UV range, which may induce cell damages. The quantum yield was not so great, leading to the necessity to use high concentration of the probe, which was moreover highly subject to photobleaching.

Then, ratiometric calcium probes were developed like Fura-2 or Indo-1, to cite the most popular. The calcium binding triggers a fluorescence intensity variation and a shift in the absorption spectrum (Fura-2) or in the emission spectrum (Indo-1). In the case of Fura-2, the fluorescence emission is centered at 510 nm for an excitation at 340 nm in presence of calcium and at 380 nm without Ca^{2+} ions. An increase in the Ca^{2+} concentration lead to an increase in the fluorescence with an excitation at 340 nm (F_{340}) and a decrease when the excitation is at 380 nm (F_{380}). Usually, to calculate Ca^{2+} concentration, the fluorescence ratio F_{340}/F_{380} is measured, explaining the name of ratiometric probe. In the case of Indo-1 the principle is the same but there is one excitation and two emissions wavelength depending on the presence of Ca^{2+} ions. Even if those probes are very efficient to measure intracellular Ca^{2+} concentration changes, experiment with Fura-2 are time limited because of the need of a continuous excitation filter change. Furthermore, these two probes are excited with short wavelength in the UV region, which may induce damages on cells.

Therefore, fluorescent probe mono excitation / mono emission with an excitation in the visible light have been synthetized. Those probes allow to see intracellular Ca^{2+} concentration changes with fast kinetics. Some of the most known examples of such probes are Fluo-3, Fluo-4, and Ca^{2+} green. In this case, the calcium binding triggers an increase in the fluorescence quantum yield of the probe. However, they don't allow precise calibration to estimate the value of the intracellular Ca^{2+} concentration.

As a conclusion, there is no ideal calcium probe. We have to choose it according to the expected experiment. In this choice, several criteria are important to consider like the dissociation constant, which must be adapted to the intracellular Ca^{2+} concentration expected. The response time has to be considered in function with the kinetics expected. With fluorescence imaging, the fluorescence quantum yield is also obviously an important parameter.

Table I-3 presents different fluorescent permeant calcium probes. Their excitation wavelength (λ_{exc}), emission wavelength (λ_{em}), and dissociation constant are reported. For both wavelength, two values are reported for ratiometric dyes, the first one being at low Ca^{2+} concentration and the second one at high Ca^{2+} concentration.

Table I-3 List of common fluorescent calcium probes, membrane permeant, with their fluorescence properties and dissociation constants (data collected from ThermoFisher Scientific).

Probe	λ_{exc} (nm)	λ_{em} (nm)	Kd
Indo-1	346/330	475/400	230 nM
Fura-2	360/330	510	145 nM
Fura-red	472/436	657/637	140 nM
Fluo-3	506	526	390 nM
Fluo-4	494	506	345 nM
Calcium green-1	506	531	190 nM
Fluo-4ff	494	517	9.7 µM
Fluo-5f	494	516	2.3 µM

Chapter II. Temperature measurement at the cellular level

The infrared stimulation of neurons call on radiations which are well absorbed by the water in biological tissues. Thus, the temperature increase is not insignificant and is even believed to play a key role in the underlying mechanism of INS. In the literature, different ways to measure the temperature at the cellular level exist with more or less limitations, detailed in the previous chapter. This chapter presents the method that we used to measure the temperature increase induced by infrared exposure and the consequent results obtained.

II.1. Rhodamine B as an optical thermometer

II.1.1. Rhodamine B

Rhodamine B (RhB) is a well-known water soluble fluorescent dye. Its fluorescence spectra are centered at 554 nm for the absorption and 576 nm for the emission, see Figure II-1. Furthermore, the fluorescence intensity of RhB decreases linearly with the temperature from at least 10 °C to 60 °C [63], [64]. In addition, the RhB fluorescence is negligibly pressure sensitive and pH independent above pH=6 [65]. In microfluidic applications, temperature has been measured in several studies with this dye [66]–[71]. Being membrane permeant, RhB appear thus like a potential tool able to measure the temperature in biological cells. It has already been used to make temperature measurement in rat tail tendon exposed to radiofrequency electromagnetic fields [72], and in our group in cells exposed to continuous wave microwaves [73].

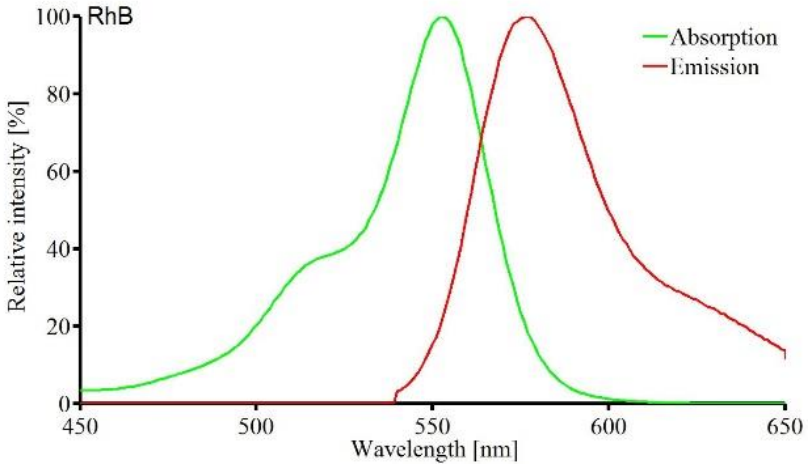

Figure II-1 Fluorescence spectra of Rhodamine B.

II.1.2. Loading of Rhodamine B in cells

Prior to fluorescence imaging experiments, cell culture growth medium was replaced with Tyrode's solution. Known as HEPES Buffered Salt Solution (HBSS), this solution consists in 121 mM NaCl, 5.6 mM KCl, 1.7 mM $MgCl_2$, 6 mM $NaHCO_3$, 12.5 mM glucose, 2.3 mM $CaCl_2$

and 25 mM HEPES. NaOH solution at 1 mM was used to adjust the pH to 7.3. U87 human glioblastoma cells or HT22 mouse hippocampal neurons [74] were incubated with a 50 µM solution of RhB in HBSS during 2 hours. Cell bath was finally washed twice with fresh HBSS before the beginning of the experiments.

II.1.3. Experimental setup

Figure II-2 shows the experimental setup used to measure the temperature in cells exposed to infrared laser light radiation and nanosecond pulsed electric fields (nsPEFs). nsPEFs are used in another project in our lab in order to investigate on their potential use to cure cancer diseases. Experiments were located in a room with a stabilized temperature at 23 °C. All the experiments in this part were made at room temperature.

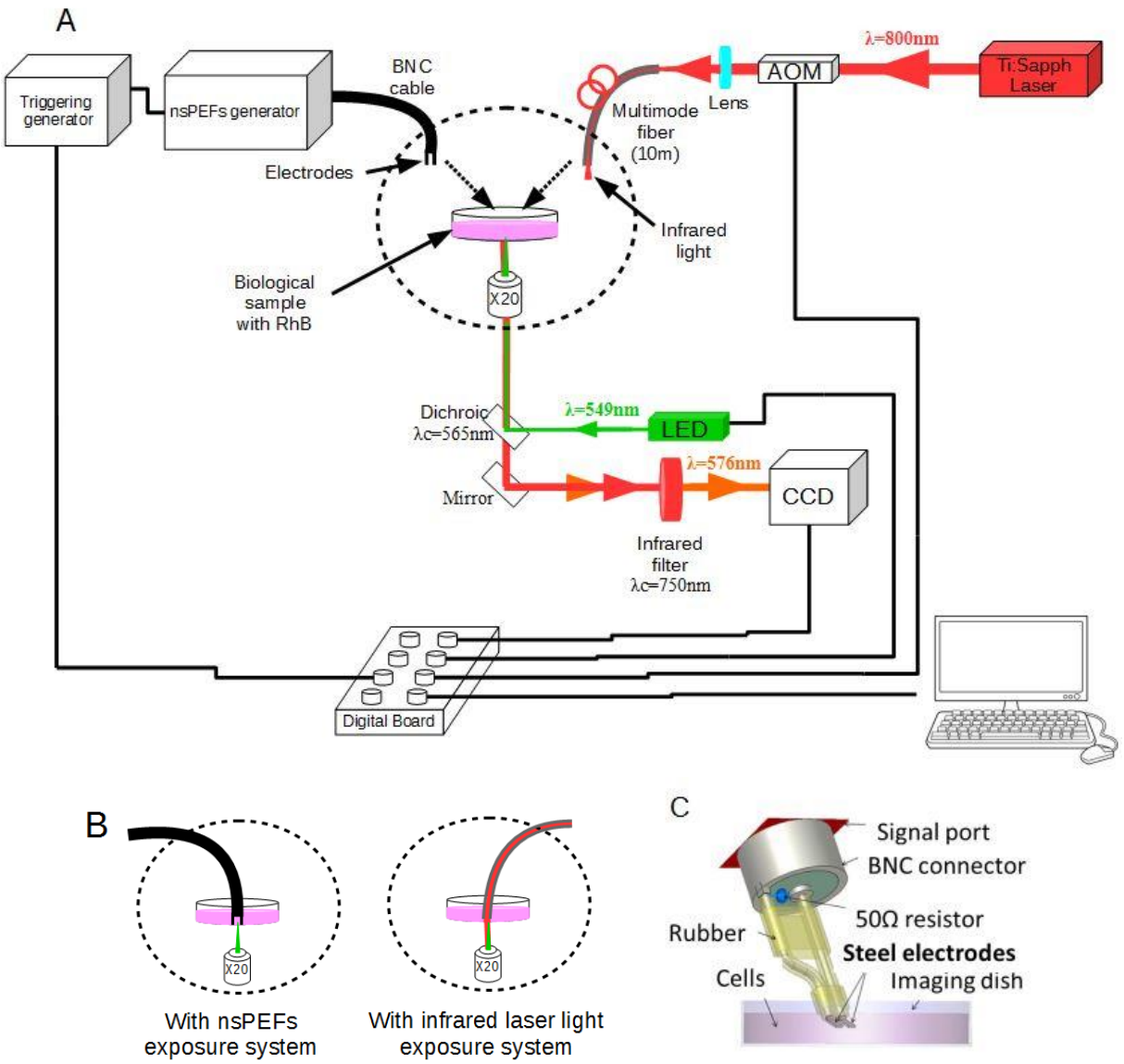

Figure II-2 Experimental setup used for temperature measurement with RhB in cells exposed to infrared radiation and nsPEFs. A. General setup. B. A zoom on the petri dish. C. Schematic representation of the electrodes used to deliver nsPEFs.

II.1.3.1. Rhodamine B fluorescence intensity detection

The detection of the fluorescence of RhB was performed using a wide field fluorescent microscope (LEICA DMI6000 B). A light emitting diode (LED) emitting at 549 nm provided by a (LED)-based light engine (Spectra7, Lumencor) was used to make the fluorescence excitation of RhB (Figure II-2.A). The light was directed to the cells using a dichroic mirror with a cutoff wavelength of 565 nm. A 20X microscope objective was used to focus the light provided by the LED to the cells loaded with RhB, and fixed on the bottom of the petri dish. The same microscope objective collected then the fluorescence light of RhB, which passed through the dichroic mirror before to be led to the electron multiplying charge-coupled device camera (EM-CCD, 16 bits, Evolve 512, Photometrics). A short pass filter with a cutoff wavelength of 750 nm was used to prevent the infrared light provided by the infrared laser light delivery system to reach the CCD camera. The parameters of acquisition of the CCD were controlled as well as the LED engine by a freely available software (Winfluor, Strathclyde University). The synchronization of all the elements in imaging system was performed using an analog output from digital acquisition (DAQ) board (USB-6229-BNC, National Instruments).

II.1.3.2. Infrared laser light exposure

For the initial proof of principle, the infrared laser source was a tunable titanium-doped sapphire oscillator (Chameleon, Coherent, INC, 680-1080 nm, 10 nm, 140 fs, 80 MHz). The central wavelength was fixed at 805 nm. The laser beam was coupled to a 10 m long multimode graded-index fiber (GIF50C, Thorlabs), with a 50 µm core diameter and a numerical aperture of 0.2 in the air. The fiber was used to have a great precision in the position of the infrared exposure, multimode to have a better injection efficiency and 10 m long because of our lab organization, the laser being on the other side of the room of the microscope. With these technical elements, the initial femtosecond pulses lose their femtosecond characteristics. But the pulse property of the laser was not useful in this case, it was only used to deliver energy to the biological sample. The maximal average power reached at the output of the fiber was about 750 mW, corresponding to a coupling efficiency with the fiber of 80 %. The optical fiber was placed 500 µm above the exposed cells using a micromanipulator. An acousto-optical modulator (AOM, MT1101R, AA Optoelectronic) was inserted before the optical fiber to rapidly modulate the infrared laser exposure parameters (infrared power and duration of the exposure). The infrared transmission by the AOM was externally controlled by analog signal initiated by Winfluor and the DAQ board. The switching delay between the application of the voltage on the AOM and the response at the fiber output was 250 µs.

II.1.3.3. nsPEFs delivery system

Nanosecond pulsed electric fields are an emerging tool especially used in cancer treatment applications[75]. nsPEFs are used to transiently permeabilize the plasma membrane of cells[76], [77], allowing for example non membrane permeant drugs uptake. Despite having high peak power, their ultrashort durations make them to be considered as non thermal due to the low average energy density that they deliver. However, Song and colleagues showed in an analytical way that nsPEFs exposure to biological cells may result in both electrical and thermal effect by Joule heating[78].

Our work consisted partly in highlighting the local increase of temperature induced by nsPEFs exposure. Thus, U87 human glioblastoma cells were exposed to nsPEFs provided by a nanosecond pulse generator delivering 10 ns pulses (FID technology, 10 kV maximum voltage, 50 Ohm output impedance). The nanosecond pulse generator was triggered by a function generator (Agilent 33120A) controlled by a custom made Labview program (Labview 7.1, National instruments). The triggering signal was recorded by the DAQ board during all the experiments. nsPEFs were recording for each experiment with an oscilloscope. Figure II-3 provides an example of the shape of the nsPEFs used. The electric field was calculated according to the different attenuators used and to the distance between the two electrodes.

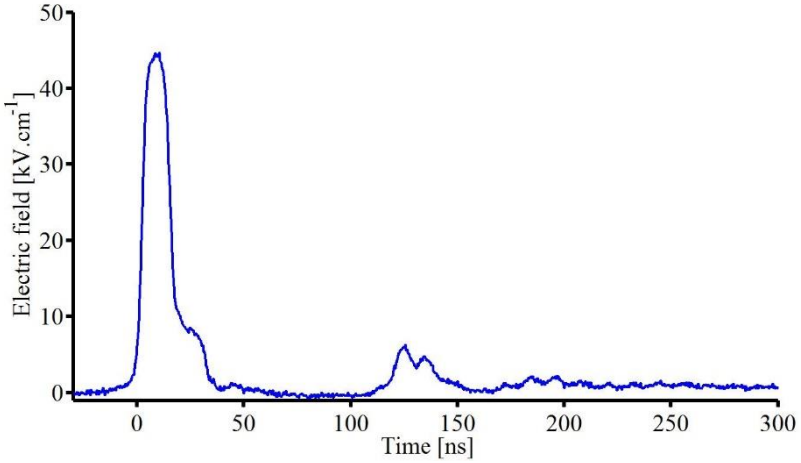

Figure II-3 nsPEF shape recorded with an oscilloscope.

II.1.4. Fluorescence intensity to temperature calibration

To be able to quantify the changes in temperature from the fluorescence intensity changes measurements, a step of calibration is necessary. To perform it, 2.5 mL of a water solution of RhB at a concentration of 50 µM was used in a petri dish. The dish was placed in a metallic ring with a resistive element and a temperature controller (TC-E35, Bioscience Tools). The whole solution was consequently heated by the metallic ring from 23 °C to 29 °C. The calibration procedure was divided into two distinct parts occurring simultaneously. The first

step was to record the evolution of fluorescence during the heating period. In the same time, the temperature of the solution was recorded with a fiber optic thermometer (Luxtron 812 Industrial Temperature Monitor), already calibrated. The Luxtron probe has an analog voltage output proportionally linked to the temperature, allowing the recording of the evolution of the temperature. Finally, by extracting the two different previous results over time, it was possible by data processing to establish the relationship between the temperature and the fluorescence intensity of RhB. Figure II-4 shows an example of the relations obtained during calibration procedure. Ten calibration procedures were performed both by increasing and decreasing the temperature. By taking the fluorescence intensity at 23 °C as a reference, the averaged decrease in the fluorescence was found to be linear and estimated at 1.6 % +/- 0.2 % per Celsius degree.

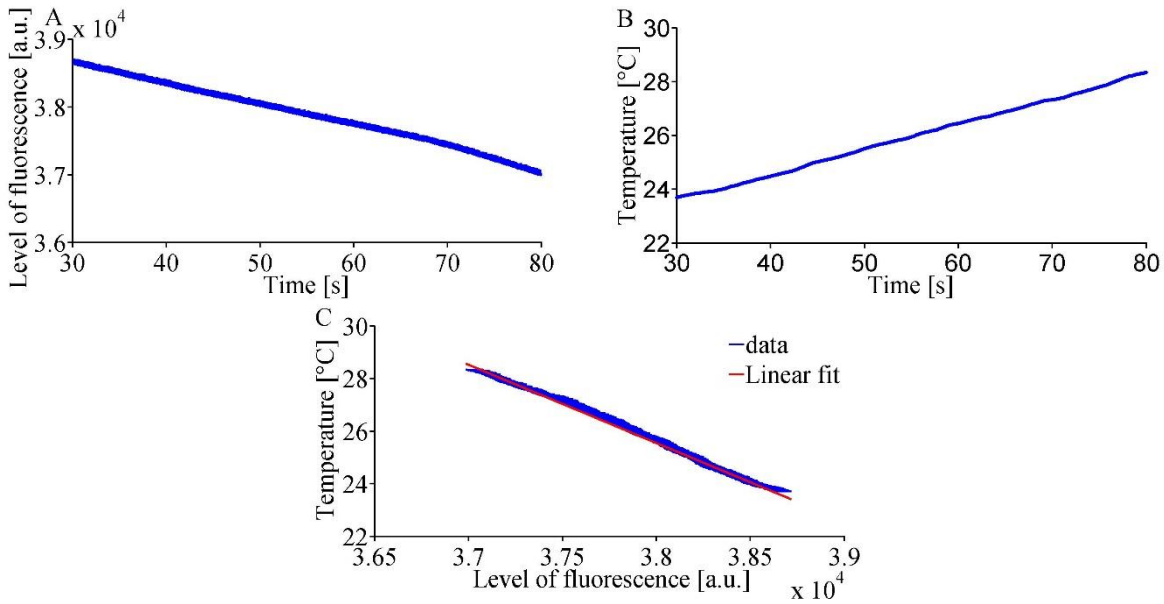

Figure II-4 Calibration procedure made in water solution with RhB at 50 µM. A. Evolution of the fluorescence intensity of RhB over time. B. Evolution of the temperature probed with Luxtron external thermometer over time. C. Relation between RhB fluorescence intensity and temperature.

II.2. Temperature measurement of cells exposed to infrared laser light

In a first time, we chose U87 human glioblastoma cells as biological sample. These cells are electrically non-excitable. They were chosen because these were cells that we had in a high quantity in our lab. Figure II-5 shows an image of U87 human glioblastoma cells labelled with RhB as they are detected on our CCD using the setup described previously. To measure the fluorescence intensity at the cellular level, the definition of a region of interest (ROI) was necessary. This ROI represents the spatial unit where the temperature is measured and an averaged level of fluorescence intensity is detected inside. The smallest the ROI is, the more

spatially precise the measure is, but the noisiest the measure is. Thus the ROI was chosen as the spatial region covered by a single cell exposed to the infrared light.

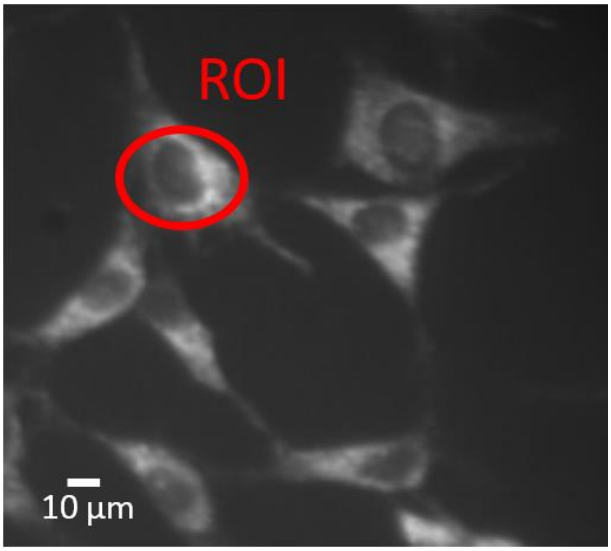

Figure II-5 Image of U87 human glioblastoma cells labelled with Rhodamine B seen by epifluorescence detection and definition of the ROI.

II.2.1. Continuous infrared exposure

The first test was to apply an infrared exposure with an average power of 500 mW at the output of the fiber during 60 s. The fluorescence recording lasted 200 s. To have a great signal to noise ratio, the integration time of the camera had to be enough long. Furthermore, during such exposure, the temporal resolution has not to be too high. Thus, an image was taken every 200 ms. Figure II-6 reports the evolution of temperature induced by such exposure.

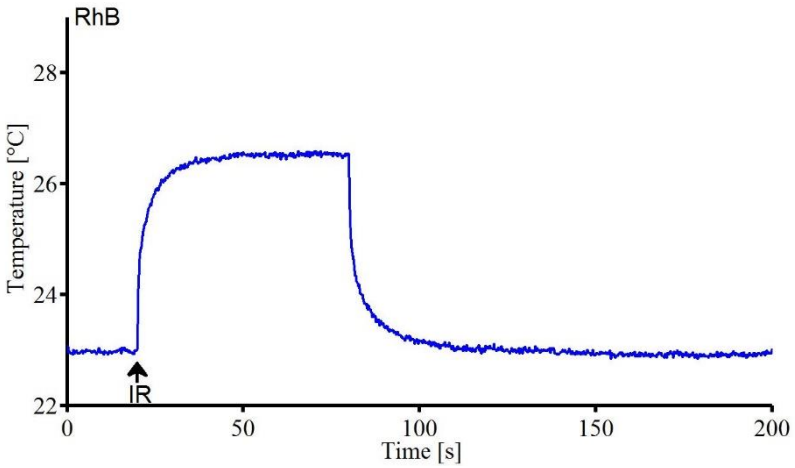

Figure II-6 Temperature evolution in U87 human glioblastoma cells exposed to 500 mW infrared laser light (λ = 805 nm) during 60 s.

The application of the infrared radiation resulted in a fast increase of temperature, then a steady state is reached, with the thermal balance between the energy delivered by the infrared radiation and the thermal exchanges with the extracellular bath. The steady state was defined

when the temperature of the system was stabilized and did not vary more than +/- 0.1 °C. The time constant of the system, defined as the necessary duration needed by the system from the beginning of the exposure to reach 63 % of the final increase of temperature, was here of 2.4 s. After the end of the exposure, the temperature of the cell returned to its initial value of 23 °C, highlighting the reversibility of the RhB fluorescence intensity changes with temperature.

II.2.2. Impact of the fiber output power

The impact of the average power at the fiber output on the temperature increase in U87 cells was then investigated. The average power was varied from 100 to 700 mW by steps of 100 mW. The other parameters remained unchanged, the fiber was still placed at 500 µm above the cells, the duration of the exposure was still 60 s, and the temporal resolution of the measurement was kept at 200 ms. Figure II-7 shows the evolution of the temperature in each case mentioned above.

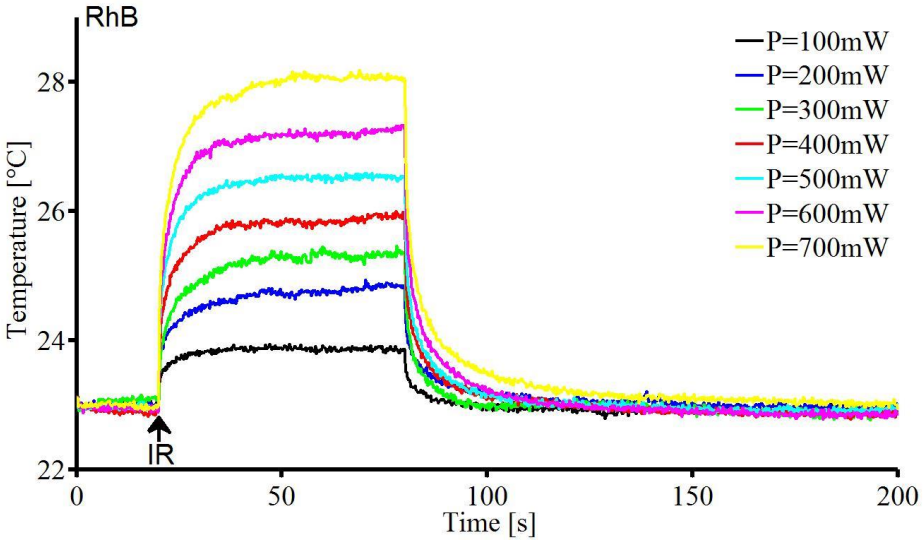

Figure II-7 Evolution of temperature of U87 human glioblastoma cells exposed to various average powers of infrared laser light (λ = 805 nm) during 60 s.

As expected, the increasing of the average power of the infrared light used for the exposure induced stronger temperature increases. The same behavior of the evolution of temperature was found for every average power used: there was a strong increase of temperature first, and then, the system reached a steady state. The time constant of the system does not vary with the average power used and was still 2.4 s (+/- 0.2 s), which is in agreement with the linearity of the heat equation diffusion, taking into account thermal exchanges by conduction and convection:

$$\frac{\partial T}{\partial t} + \left(\vec{v}.\overrightarrow{grad}\right).T = D_t.div\left(\overrightarrow{grad}(T)\right) + \frac{P_c(t)}{C_m.\rho_m} \qquad \textbf{Eq II-1}$$

Where

- T denotes the temperature.

- $\vec{v}$ is the speed of the fluid, induced by convection.

- D_t represents the thermal diffusivity.

- $\frac{P_c(t)}{C_m \cdot \rho_m}$ represents the energy brought by the infrared exposure.

The variation of temperature ΔT between the start of the exposure and the temperature reached at the steady state are reported in Table II-1 and Figure II-8.

Table II-1 Evolution of ΔT in function with the infrared power applied.

Output fiber power (mW)	ΔT (°C)
100	0.7 +/- 0.1
200	1.7 +/- 0.1
300	2.2 +/- 0.1
400	2.8 +/- 0.1
500	3.4 +/- 0.1
600	4.2 +/- 0.1
700	5 +/- 0.1

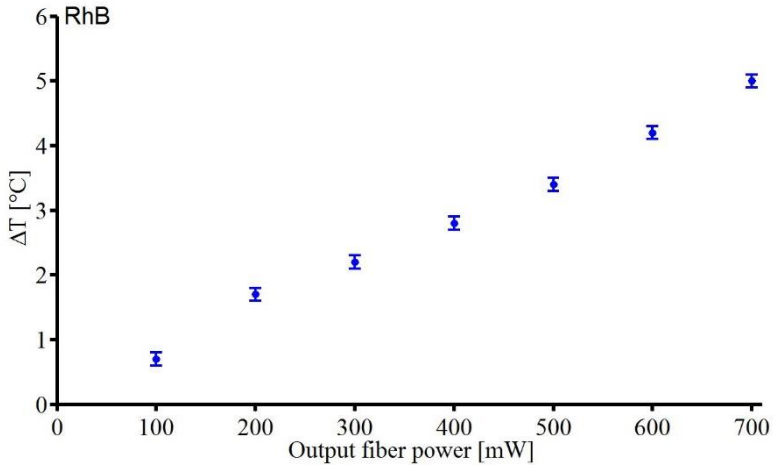

Figure II-8 Evolution of ΔT in function with the infrared power applied.

II.2.3. Temporal resolution of the system

Intermittent rectangular pulses of infrared exposure were used to evaluate the temporal resolution of the method reached with our setup. The fiber output average power was set at 500 mW with the fiber tip maintained at a distance of 0.5 mm from the cells. The infrared exposure consisted of a series of 100 ms pulses separated by a delay of 50 ms (duty cycle = 67%) over a period of approximately 10 s. Figure II-9 presents the subsequent temperature

changes induced by such exposure. A magnified view of the temporal pattern of the infrared exposure as well as the temperature change induced is shown in the inset of Figure II-9.

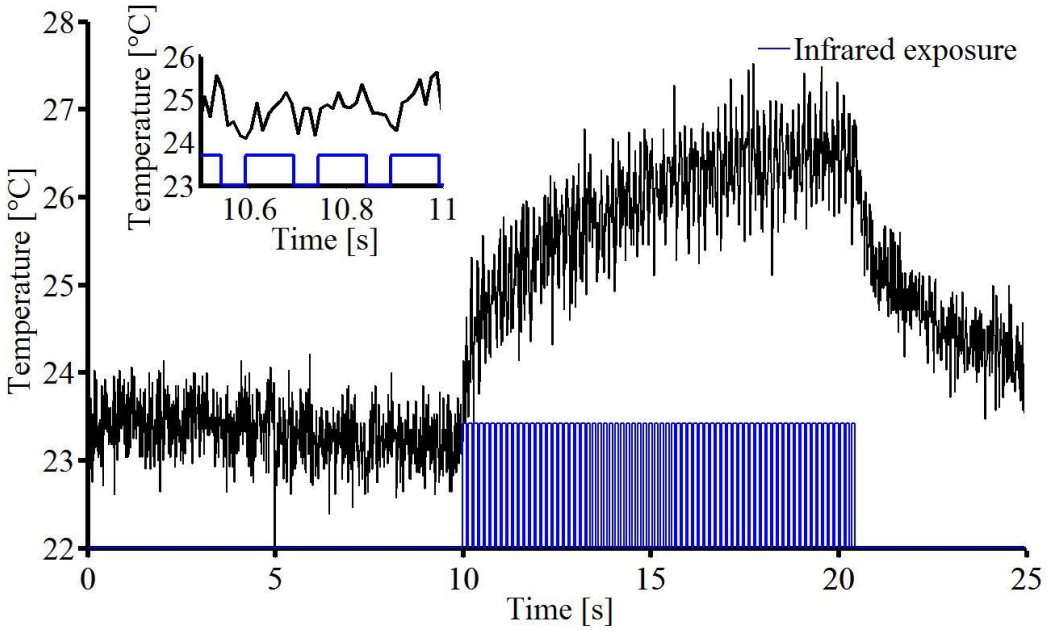

Figure II-9 Effect of intermittent infrared exposure on the temperature.

With the limitations in the camera readout and LED control speed, the best temporal resolution obtained to make measurements was 4 ms. To reach that precision, the integration time of the camera was decreased to 4 ms. As a consequence, the signal to noise ratio decreased a lot, resulting in the presence of noise in the data. Each infrared pulse is correlated to a small increase of temperature when the delay between pulses is correlated with a decrease of temperature. However, this delay was too short to reach back the basal temperature. Thus, the intermittent infrared exposure applied induced a global increase of temperature of nearly 3.5 °C, from 23 °C to 26.5 °C. Unfortunately, the noise present in the measurement, due to the low integration time needed on the camera, prevented us to estimate obviously the value of the increase of temperature induced by one single pulse. However, it is possible to say that with a CCD camera with better quantum efficiency, the temporal resolution of the method could reach a few milliseconds at least, as showed here.

II.3. Temperature measurement of cells exposed to nsPEFs

II.3.1. Comparison between temperature probe with RhB and temperature probe with Luxtron

With the promising rapid temperature measurement performed with RhB in U87 human glioblastoma cells, the method was used in the case where cells are exposed to nsPEFs, another subject of interest of our lab, see Figure II-2 for the experimental setup. To study the likely local temperature change induced by the exposure to nsPEFs, the electrodes were

positioned such like that the field of view of the microscope was between the electrodes. The regions of interest chosen here were single cells located in the center part of the field of view. The parameters of nsPEFs exposure were made in agreement with the parameters used in other researches of the lab. 1, 10, or 100 nsPEFs were applied with a frequency of 10 or 100 Hz. The pulses had a duration of 10 ns with an electric field set at 44.1 $kV.cm^{-1}$. The pulse triggering signal was recorded and synchronized with the temperature measurement.

Until know, such temperature measurement were made using the commercial fiber optic thermometer Luxtron. The Luxtron fiber probe is a specialized temperature sensor, immune to likely interferences due to high voltage and radiofrequency with a response time varying between 250 ms (stirred water) and 1.25 s (still air). The accuracy given by the manufacturer is about +/- 0.5 °C. Thus, the differences between probing the temperature with RhB and with Luxtron probe were investigated. The excitation parameters were made with cells labelled with RhB and then with the Luxtron probe precisely placed between the electrodes. With RhB, the temporal resolution was 200 ms. Figure II-10 shows the corresponding evolution of temperature probed with both techniques. Table II-2 summarizes the changes in the temperature probed with both methods.

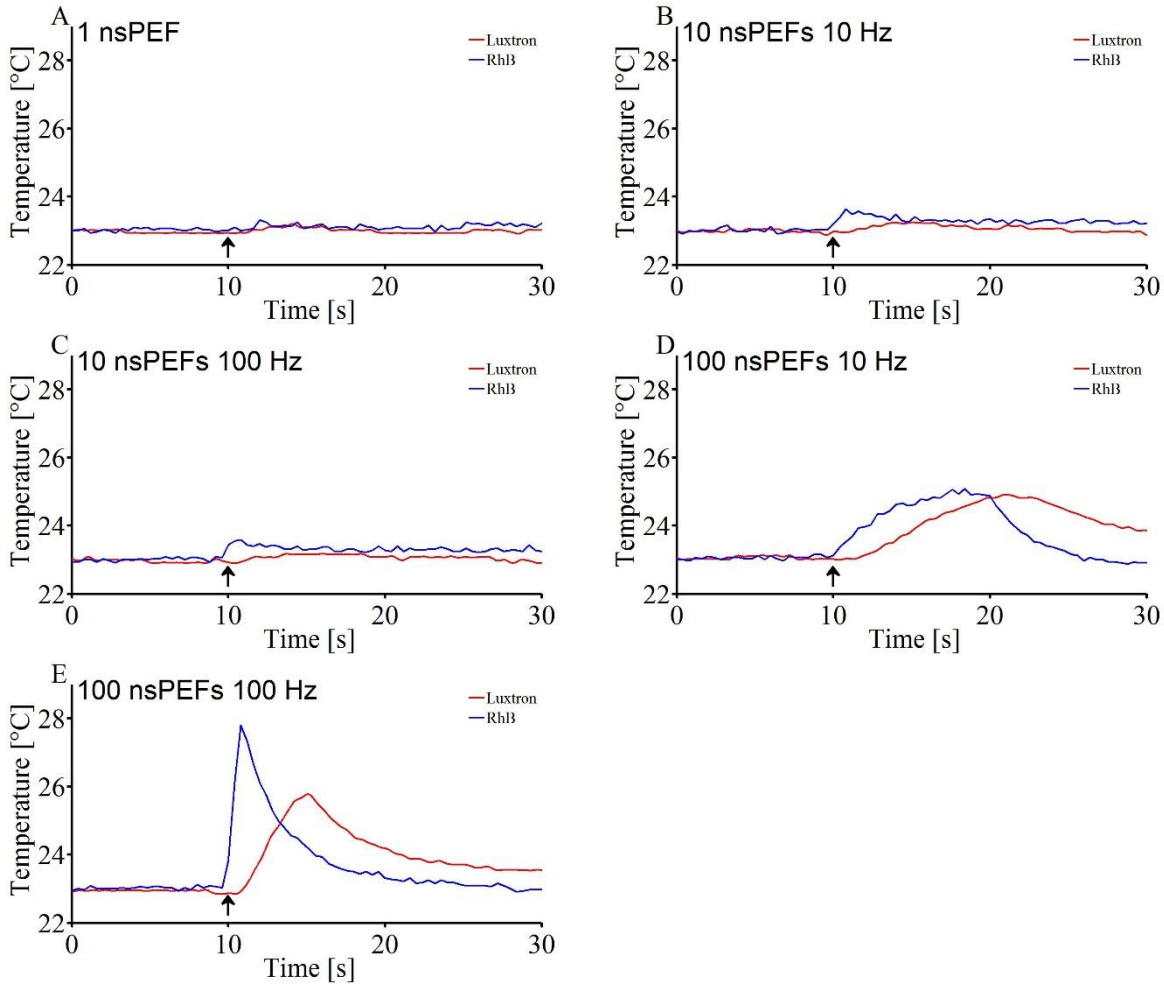

Figure II-10 Evolution of the temperature over time induced by the exposure to nsPEFs probed by RhB in U87 human glioblastoma cells and by Luxtron probe. The arrows denote the beginning of the exposure to nsPEFs. A. 1 nsPEF. B. 10 nsPEFs at 10 Hz. C. 10 nsPEFs at 100 Hz. D. 100 nsPEFs at 10 Hz. E. 100 nsPEFs at 100 Hz.

Table II-2 Temperature modification induced by the exposure to nsPEFs probed by RhB in U87 human glioblastoma cells and by Luxtron probe.

		Number of nsPEFs					
		1		10		100	
		RhB	Luxtron	RhB	Luxtron	RhB	Luxtron
Frequency (Hz)	10	0 °C	0 °C	0.6 °C	0.3 °C	2.1 °C	2 °C
	100			0.6 °C	0.3 °C	4.8 °C	2.8 °C

The application of a single 10 ns pulse did not result in the observation of any temperature change with neither the RhB measurement in U87 human glioblastoma cells nor the Luxtron probe placed between the electrodes. For both frequency of 10 and 100 Hz, the application of 10 nsPEFs resulted in a temperature change of 0.6 °C according to RhB measurement and 0.3 °C according to the Luxtron probe. The importance of the frequency and the differences that it induces on the temperature change is well observable with the application of 100 nsPEFs. In this case, both temperature measurement techniques are in agreement with the fact that the use of 100 nsPEFs at 100 Hz induced higher increase of temperature than the use of 100 nsPEFs at 10 Hz.

The most important point here is the differences observed in the temperature modification when measured with RhB or with Luxtron probe. An obvious difference is the presence of a delay between the time when RhB reported temperature changes and when the Luxtron probe detected those changes in the extracellular volume between the electrodes. Considering the experiments done with 100 nsPEFs, the use of a frequency of 10 Hz resulted in a similar temperature change detected by both techniques (Figure II-10.D), about 2 °C. However, when RhB probed the increase of temperature in a synchronously manner with the application of the nsPEFs, the Luxtron probe reported this change with a delay due to its lowest temporal resolution. But the relative long duration of such exposure compared to the temporal resolution probably did not altered the magnitude of the temperature measurement. The same magnitude being found by the two techniques demonstrated the ability of RhB to probe the temperature even when it is exposed to high voltage.

When considering the same number of nsPEFs but with 100 Hz (Figure II-10.E), the temporal resolution took a greater importance. With RhB, the temperature change probed is still observed in a synchronously manner with the application of the nsPEFs. With Luxtron probe, the temporal resolution was not sufficient to measure the temperature elevation before its dissipation and resulted in an incorrect measurement, both in the duration and in the amplitude of the temperature change (4.8 °C measured with RhB against 2.8 °C with Luxtron). The external fibered optic thermometer Luxtron was not precise enough to represent the good

temporal evolution of the temperature as observed in U87 human glioblastoma cells with RhB fluorescence.

The Luxtron thermometer offers the possibility to make accurate temperature measurements in fluids in an easy way, even during high voltage experiments. However, its temporal resolution prevents to make accurate measurements during fast phenomena as the exposure to nsPEFs during 1 s (100 nsPEFs at 100 Hz). Rhodamine B used as an optical thermometer presents a better temporal resolution than the Luxtron probe, as well as a better thermal precision, depending on the CCD camera used to record fluorescence intensity. Another strong difference between the two methods is the spatial resolution. With RhB, it is possible to measure the temperature at the cellular level, inside a single cell, when with the Luxtron probe, it's only possible to probe the temperature in the extracellular medium, in a small volume surrounding the tip of the probe.

II.3.2. Impact of the electric field strength on the temperature increase

Fixing the number of nsPEFs to 100 and the frequency to 10 Hz, the effect on the electric field applied on the temperature increase has been studied. Here temperature measurement were made at the cellular level with RhB. The electric field was varied from 5.5 kV.cm^{-1} to 44.1 kV.cm^{-1} including 11, 17, 22 and 34 kV.cm^{-1}. Figure II-11 shows on one side the evolution of the temperature over time at the cellular level induced by such exposure and on the other side the influence of the electric field strength on the temperature increase.

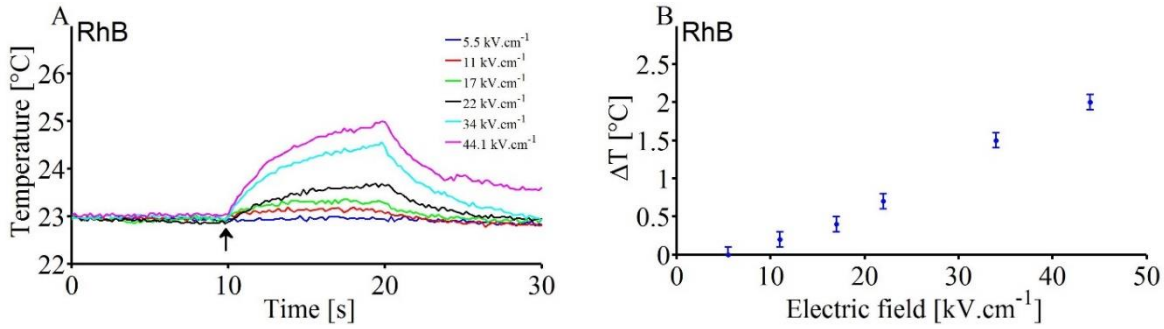

Figure II-11 A. Effect of the electric field strength on the temperature evolution over time induced by the exposure to 100 nsPEFs at 10 Hz probed by RhB in U87 human glioblastoma cells. The arrow denotes the beginning of the exposure. B. Effect of the electric field strength on the increase of temperature.

As expected, the electric field strength played a key role in the local temperature increase induced by nsPEFs application. Increasing the electric field resulted in the increase of the temperature change. With temporal resolution of 200 ms and thermal precision of +/- 0.1 °C, The observation of a non-negligible thermal effect happened from the application of field strength of 11 kV.cm^{-1}, for the application of 100 nsPEFs, 10 ns long, at 10 Hz. All the previous results of temperature measurement in cells exposed to both infrared radiation and nsPEFs were published in Biomedical Optics Express in 2015 [79].

II.4. Application of temperature measurement with Rhodamine B in cells during infrared neural stimulation

The previous part was made at the beginning of the PhD. During the PhD, equipment changed and the experimental setup evolved. The experimental setup is consequently presented here again and a different calibration procedure has been made in agreement with the new filter set installed.

II.4.1. Experimental setup

Figure II-12 shows the experimental setup used to measure the temperature in cells exposed to infrared radiation used to make infrared neural stimulation presented in Chapter 4. Experiments were located in a room with a stabilized temperature at 23 °C. Here the biological sample used was HT22 mouse hippocampal neurons [74], an immortalized neuronal cell line. Cells were maintained at a physiological temperature about 37 °C using a resistive heating element and temperature controller (TC-E35, Bioscience Tools). The temperature was also measured by a calibrated fiber optic thermometer and was found to worth 37 °C +/- 1°C (LUXTRON 812 Industrial Temperature Monitor).

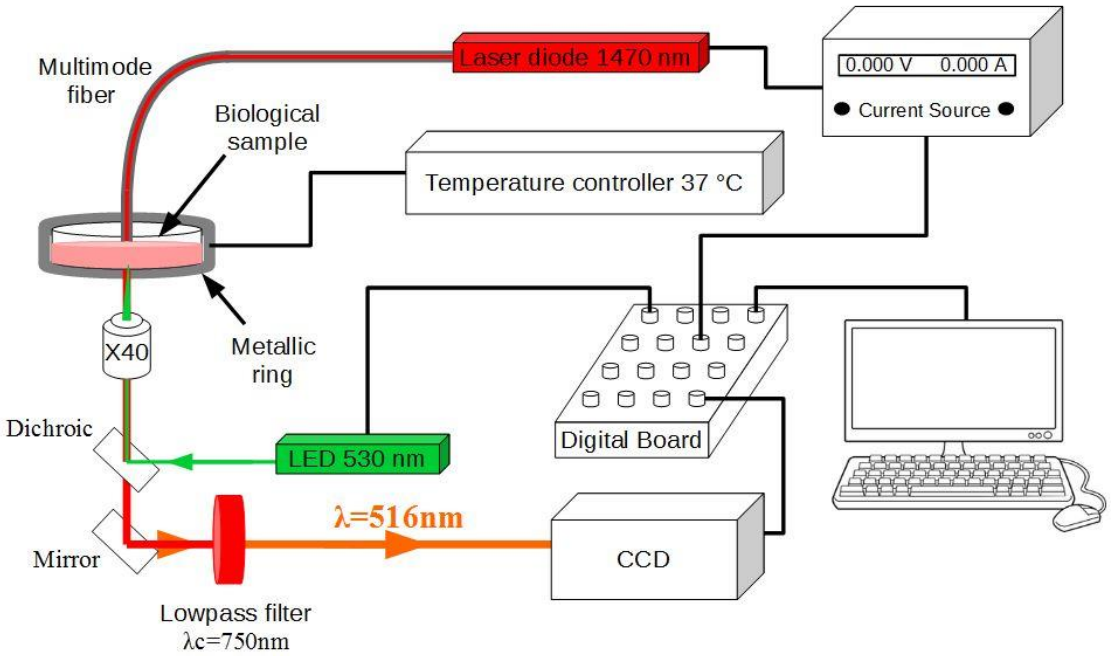

Figure II-12 Experimental setup to make temperature measurements in cells exposed to 1470 nm radiation

II.4.1.1. Rhodamine B fluorescence intensity detection

To measure RhB fluorescence intensity, a wide field inverted microscope (Olympus IX70) was used. The excitation of the dye was ensured by a light emitting diode (4-Wavelength High-

Power LED Source, Thorlabs). A 40X microscope objective with a numerical aperture of 0.6 (Olympus) was used to focus the excitation. The backward fluorescence emission (λ_{em}=576 nm) of RhB was collected by the same microscope objective before to pass through the multichroic mirror (59012bs, Chroma) and to be detected with a 14 bit CCD camera (pixel matrix 512x512, iXon, AndorTM Technologies). A shortpass filter (λc=750 nm, FES0750, Thorlabs) was placed before the CCD camera to block the infrared light coming from the infrared exposure system. The acquisition parameters of the CCD and the LED emission parameters were externally controlled with Winfluor software and with a DAQ board.

II.4.1.2. Infrared radiation exposure

The infrared source used was a multimode laser diode (LU1470T015, Lumics), emitting in continuous wave mode at 1470 nm. The laser diode presents a fibered output with a 105 µm core diameter and a 0.15 numerical aperture. A cooling block (LU_CB_T_0, Lumics) was used to stabilize the temperature and an adapted power supply (LU_DR_AD, Lumics) controlled the exposure duration and the power of the emitted infrared radiation. The power supply was externally controlled with Winfluor. Thus, exposure parameters were controlled and synchronized with the fluorescence detection of RhB. The tip of the fiber was placed at a distance of 500 µm of the targeted cells, using a micromanipulator.

II.4.2. Fluorescence intensity to temperature calibration

To be able to quantify the changes in temperature from the fluorescence intensity changes measurements, a step of calibration is necessary. To perform it, 2.5 mL of a water solution of RhB at a concentration of 50 µM was used in a petri dish. The dish was placed in a metallic ring with a resistive element and a temperature controller (TC-E35, Bioscience Tools). The whole solution was consequently heated by the metallic ring from about 37 °C to 52 °C, since high temperature increases are expected. 52 °C is the highest temperature reached with the metaling ring used as a heating element. The calibration procedure was a bit different from the calibration explained earlier in the chapter to have better precision: the RhB solution was still heated thanks to the resistive element, but here, by steps. The solution was heated for a few degrees, and we waited a short time to have a homogeneous temperature in the whole solution. Then, the temperature probed by the Luxtron thermometer was reported and the fluorescence spectrum of RhB seen with our setup, with its filter set, was recorded. To acquire the spectra, the LabRAM HR Evolution spectrometer (HORIBA scientific) was used. For each temperature, 10 spectra were recorded and averaged. Figure II-13.A shows the evolution of the fluorescence spectrum of RhB, seen with our setup and optical filters, with the temperature. The area under each spectrum was calculated and normalized compared to the value at 37 °C. The results are reported in Figure II-13.B. A linear evolution was observed and fitted at the

maximum with the data points. According to this calibration procedure, the RhB fluorescence decreased from 2.4 %.°C^{-1} by taking 37 °C as reference value.

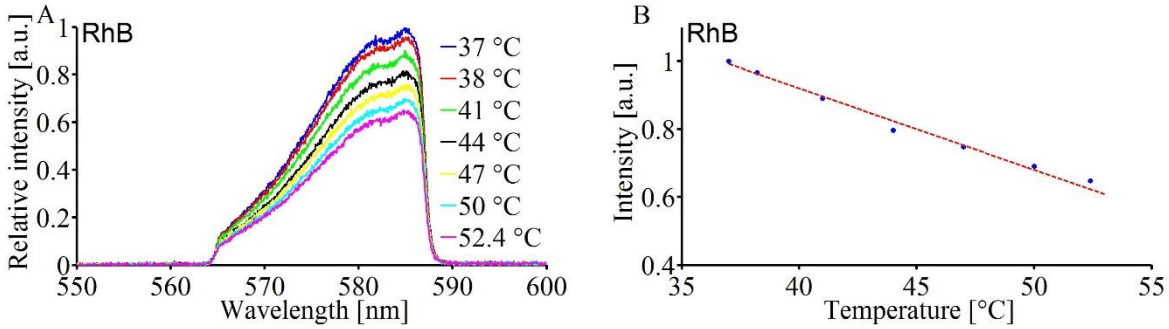

Figure II-13 Calibration procedure made in water solution with RhB at 50 µM by measuring RhB spectrum at different temperature. A. Evolution of the RhB fluorescence spectrum with the temperature. B. RhB relative intensity decreased of 2.4 %.°C^{-1} with 37 °C as reference temperature value.

II.4.3. Temperature measurement in cells exposed to infrared radiation

As explained in the first chapter, the local temperature increase by the absorption of the infrared radiation during INS is believed to play a key role. Compared to the titanium-doped sapphire oscillator radiation at 805 nm, the radiation delivered by the laser diode is centered at 1470 nm. The water absorption coefficient is thus much higher with the laser diode radiation (about 28 cm^{-1} at 1470 nm against about 2.10^{-2} cm^{-1} at 805 nm, see Figure I-6). Thus, the temperature change and its gradient are expected to be here much higher than the previous results presented. Therefore, the temperature change was first measured in a water solution of RhB (50 µM) to have an approximate idea of the amplitude of the temperature change and more importantly of the dynamics we need with the CCD camera to be able to measure such changes with a good signal to noise ratio.

The duration of the exposure was 500 ms with an average power varying from 25 mW to 275 mW by steps of 25 mW. The temporal resolution used was here 20 ms. Figure II-14 shows the evolution over time of the temperature for each power applied and the evolution of the maximal temperature reached in function with the infrared powers used. Each measurement was made 5 times and then averaged.

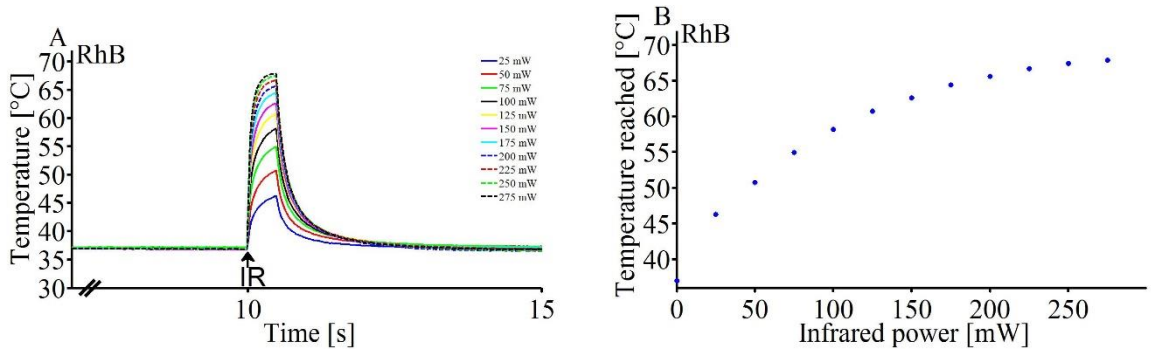

Figure II-14 Evolution of the temperature in water solution exposed to 1470 nm radiation. A. Evolution over time for different infrared averaged power used. B. Evolution of the maximal temperature reached with the averaged power.

Then, the exact same procedure was applied with HT22 mouse hippocampal neurons loaded with RhB. Here, the signal being lower, the temporal resolution had to be a bit worse with 50 ms precision. Figure II-15 shows the evolution over time of the temperature for each power applied and the evolution of the maximal temperature reached in function with the infrared power used. Each measurement was made 9 times, on 9 different cells and then averaged.

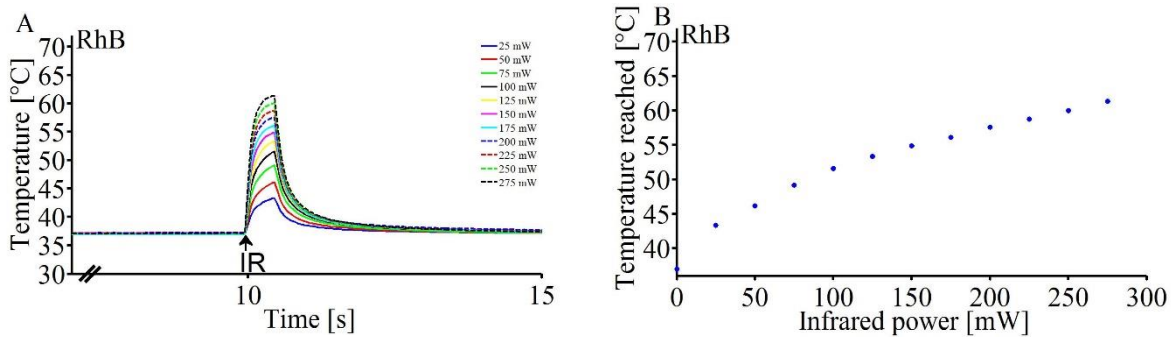

Figure II-15 Evolution of the temperature in HT22 mouse hippocampal neurons exposed to 1470 nm radiation. A. Evolution over time for different infrared averaged power used. B. Evolution of the maximal temperature reached with the averaged power.

The parallel between temperature measurements in water solution and in HT22 mouse hippocampal neurons has been made to see the existing differences. Figure II-16 shows the evolution of the temperature reached with the infrared power applied for both kind of measurements.

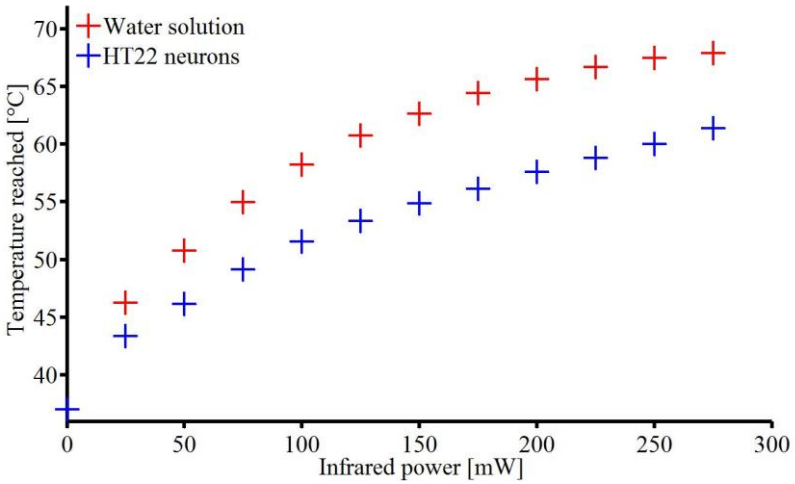

Figure II-16 Evolution of the maximal temperature reached with the averaged power in water solution and in HT22 mouse hippocampal neurons.

A significant difference is observed between temperature measurements performed in water solution and in HT22 mouse hippocampal neurons. Considering the same exposure parameters, the temperature increase is smaller in biological cells than in the water solution.

As a hypothesis, a part of those differences could be due to the plasma membrane, constituted of lipids, known as thermal insulator. Those differences may also be attributed to an infrared-induced leak of RhB from inside of the cell to outside.

II.5. Conclusion

Among the methods allowing temperature measurement at the cellular level, using RhB fluorescence is an easy way with respect to both the optical setup and the needs of biologists. In the literature, the temperature sensitivity of RhB fluorescence intensity has been exploited to make temperature measurement in fluidic applications at the micron scale.

Here, we used the same property of this fluorescent dye to perform temperature measurement at the cellular level, exposed to an exogenous heat source. The thermal effect of infrared radiation at 805 nm and of nsPEFs were first demonstrated with a thermal precision of 0.1 °C. Fluorescence process being quasi instantaneous compared to the temporal resolution reached by the CCD cameras used to detect it, the method allowed a greater temporal resolution than the Luxtron probe, a commercially available thermometer. Temporal resolution is an important parameter to consider, especially when the exogenous heat source is applied during a really short time or with high frequency. With that method, in this chapter, the local increase of temperature induced by the exposure to nsPEFs has been experimentally highlighted for the first time.

Finally, to have an idea of the increase of temperature induced by INS, temperature measurement were performed in HT22 mouse hippocampal neurons exposed to 1470 nm radiation used hereafter to perform INS. This is a first step in the understanding of phenomena induced by biological tissue heating. Those last results will be used again farther in this thesis, combined with INS intracellular responses.

Chapter III. Triggering calcium transients through the activity of Phospholipase C by infrared radiation exposure

The underlying mechanism behind the infrared stimulation of neurons remains unclear, as explained in Chapter I. In the literature, different theories have been proposed involving the activation of temperature sensitive calcium ion channels located on the plasma membrane (TRPV) [43]–[45] or the creation of pores in the plasma membrane allowing ions to move in the cell [80]. Both of those theories lean on the influx of cations, typically Ca^{2+} ions, from the outside of the cell to the inside, leading to an intracellular Ca^{2+} ion concentration increase. However, Ca^{2+} ions may also come from the inside of the cell. Some organelles, located in the cytosol of the cell, are known to be internal calcium stores like the endoplasmic reticulum or the mitochondria (see Figure III-1), and may be at the origin of the intracellular Ca^{2+} ion concentration increase observed.

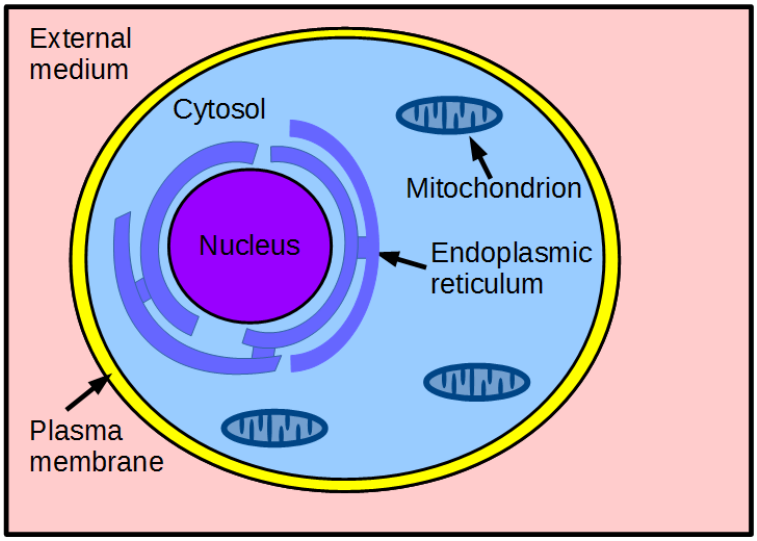

Figure III-1 Internal calcium stores: mitochondrion and endoplasmic reticulum

The previous hypotheses considered effects occurring at the level of the plasma membrane. Another study led in cardiomyocytes showed the evidence of an intracellular effect triggered by the infrared exposure [50]. They revealed that the infrared induced Ca^{2+} transients were of mitochondrial origin.

This chapter attempts to make a clarification on the underlying mechanism involved in the infrared neural stimulation. The intracellular effect of INS is highlighted by the intracellular Ca^{2+} ion concentration increase induced by the infrared exposure, found to be originating from the release of Ca^{2+} ions from the endoplasmic reticulum.

III.1. Calcium ions release from the endoplasmic reticulum: involvement of the Phospholipase C

III.1.1. Intracellular calcium signaling induced by Phospholipase C activity

Figure III-2 illustrates the way used to trigger Ca^{2+} ions release in the cytosol from the endoplasmic reticulum involving the enzyme Phospholipase C. It all starts with the activation of G protein. G proteins are a family of proteins specialized in the transmission of a wide variety of stimuli signals from outside to the inside of the cells. At rest, G protein is inactive when it is attached to guanosine diphosphate (GDP). When a signaling molecule, also called messenger, binds to a receptor, it changes the receptor shapes. This results in the binding of the receptor to the inactive G protein, and a guanosine triphosphate (GTP) molecule displaces the GDP. The binding to GTP make the G protein active. To return to inactive state, G protein hydrolyzes GTP into GDP. Other external signals like voltage for example may activate G protein. Active G proteins triggers a series of chemical reactions in the cell. For example, when Gq protein, one of the family of the G proteins, is switched on with the binding of GTP, it results in the activation of the Phospholipase C (PLC) isozyme PLC-β, starting a phosphoinositide signaling process. PLC is an enzyme which hydrolyzes phospholipids just before the phosphate group. PLC-β activation results in the catalysis of the hydrolysis of the phosphoinositide phosphatidylinositol 4,5-bisphosphate (PIP_2). PIP_2 is thus split into two, resulting in the production of inositol 1,4,5-trisphosphate (IP_3) and of diacylglycerol (DAG), secondary messengers used in signal transduction and lipid signaling in biological cells. While DAG stays inside the membrane, IP_3 is a soluble molecule which diffuses through the cytosol to the endoplasmic reticulum (ER), a cell organelle known to be an intracellular calcium store. Once IP_3 reached the ER, it is able to bind to Ins3P receptors on a ligand gated Ca^{2+} channel located at the ER surface. This results in the opening of Ca^{2+} channels and in the release of Ca^{2+} ions in the cytosol.

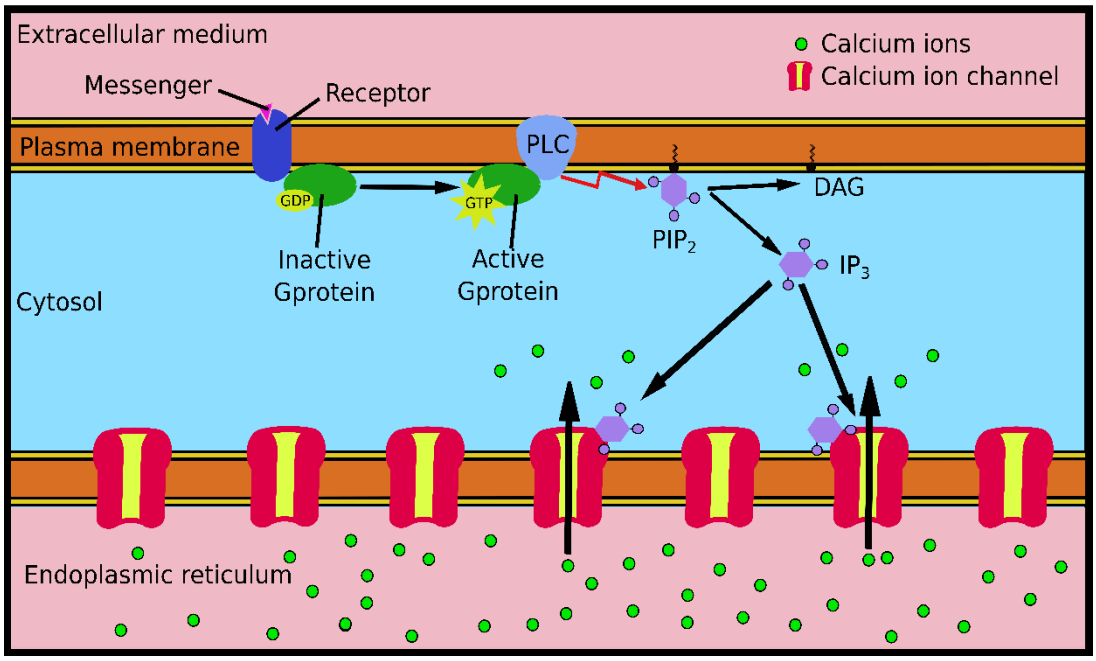

Figure III-2 The IP_3 pathway: calcium ions release from the endoplasmic reticulum induced by Phospholipase C activity

III.1.2. Phosphoinositide signaling possibly induced by infrared exposure

Among the studies reviewed in Chapter 1 concerning the underlying mechanism of infrared neural stimulation, some points may lead to think that infrared exposure could trigger stimulation of phosphoinositide signaling, like the activation of phospholipase functions. In cardiomyocytes, that are electrically excitable cells, Dittami and colleagues [50] showed that infrared exposure led to intracellular Ca^{2+} transients. With the use of the pharmacological inhibitor of the mitochondrial Na^+ / Ca^{2+} exchanger (CGP-37157), the intracellular Ca^{2+} transients were attenuated. They concluded on the mitochondrial origin of the Ca^{2+} ions. They also reported the same effect by using 2-APB and ryanodine, which are known to inhibit the release of calcium ions from the endoplasmic reticulum. Furthermore, Smith *et al*. [81] used femtosecond pulsed infrared exposure on HeLa cells, non-electrically excitable, and showed the infrared-induced generation of calcium waves. During the experiments, there was no calcium in the external medium, leading to conclude on the involvement of intracellular Ca^{2+} stores. Consequently, according to the two previous works, it is conceivable to think that the release of Ca^{2+} ions from the endoplasmic reticulum may be a common mechanism in intracellular infrared-induced effects.

In a more recent work, Beier *et al*. [80] proposed the transient plasma membrane nanoporation as mechanism explaining the infrared neural stimulation. In this work they also investigated the thermal destabilization of phospholipids induced by infrared exposure. They used Chinese hamster ovary (CHO) cells expressing human muscarinic type 1 receptor which was transfected with PLCδ-PH-EGFP construct. PLCδ-PH-EGFP has a high affinity to IP_3, and its

location is probed thanks to the EGFP fluorescence. Thus, it is used to probe the location of IP_3 by fluorescence detection. Initially, it appeared in the membrane, when IP_3 is still a part of PIP_2. Following infrared exposure, the fluorescence signal translocated moved to the cytosol of the cells, representing the depletion of PIP_2 and the release of IP_3. As discussed by the authors, this could be evidence of phosphoinositide signaling stimulation by infrared exposure.

Thus, in this chapter, we investigate whether infrared exposure is able to trigger phosphoinositide signaling. More particularly, we have a focused interest of the possible activation of phospholipase C and the IP_3 pathway leading to calcium ions release from the endoplasmic reticulum to the cytosol.

III.2. Material and methods

III.2.1. Experimental setup

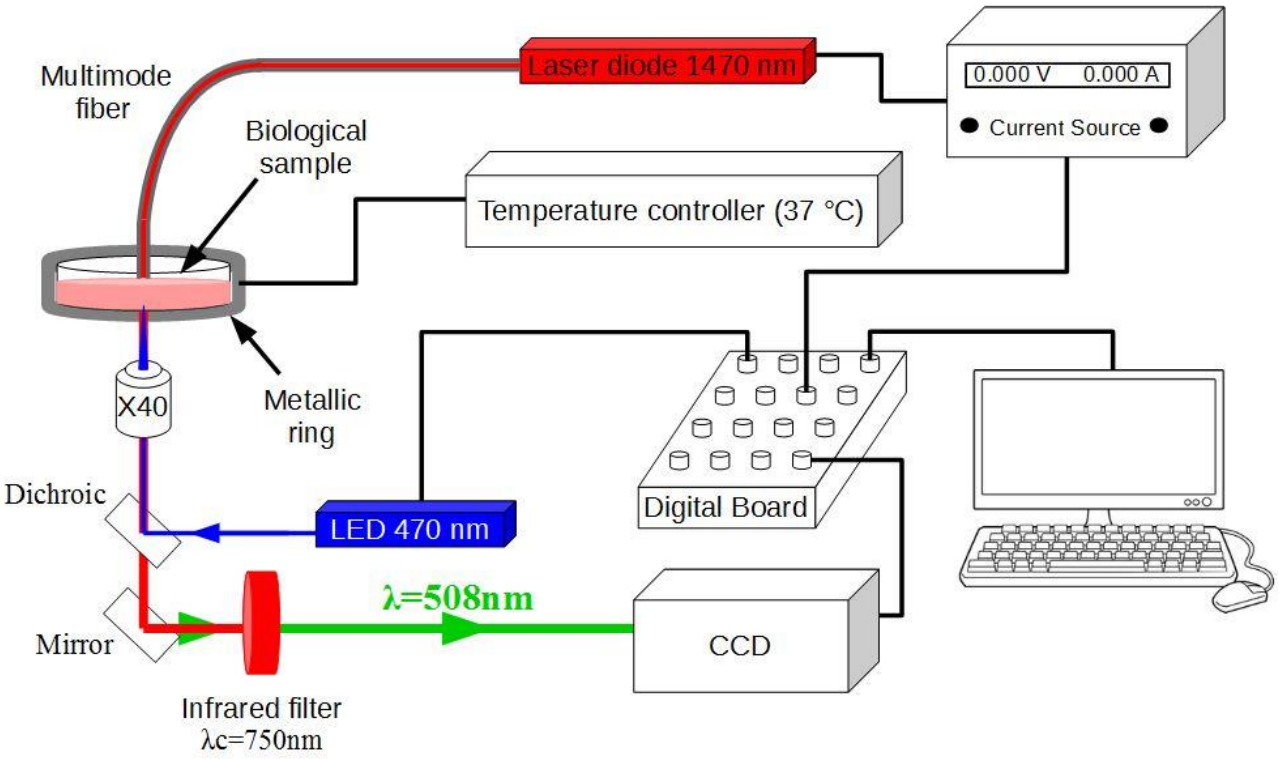

Figure III-3 Experimental setup

Figure III-3 shows the experimental setup used to expose cells to infrared, built around a wide field inverted microscope (Olympus IX70). Cells were maintained in a medium at a physiological temperature about 37 °C using a resistive heating element and temperature controller (TC-E35, Bioscience Tools). The bulk temperature was also measured by a calibrated fiber optic thermometer and was found to worth 37 °C +/-1 °C (LUXTRON 812 Industrial Temperature Monitor).

HT22 immortalized mouse hippocampal neurons [74] (The Salk Institute, La Jolla, CA), as example of excitable cells, and U87 human glioblastoma cells (ECACC, Public Health England, 89081402), as example of non-excitable cells, were used.

III.2.2. Fluo-4 AM loading and intracellular calcium imaging

Prior to fluorescence imaging experiments, cell culture growth medium was replaced with Tyrode's solution. Known as HEPES Buffered Salt Solution (HBSS), this solution consists in 121 mM NaCl, 5.6 mM KCl, 1.7 mM MgCl2, 6 mM NaHCO3, 12.5 mM glucose, 2.3 mM CaCl2 and 25 mM HEPES. NaOH solution at 1 mM was used to adjust the pH to 7.3. To probe the intracellular calcium imaging, the membrane permeable fluorescent dye Fluo-4 AM was loaded in cells during 45 minutes. With a Kd of about 345 nM, Fluo-4 allows to detect Ca^{2+} concentration in its linear regime (defined in chapter I, section I.6) from approximately 39 nM to 3.16 µM (corresponding respectively to 10 % and 90 % of the maximal fluorescence). We thus probed intracellular calcium changes in the linear regime of the dye, since resting calcium is less than 100 nM, and intracellular elevations are about 2 µM. Cell bath was finally washed twice with fresh HBSS before the beginning of the experiments.

The fluorescence spectra of Fluo-4 are shown in Figure III-4.

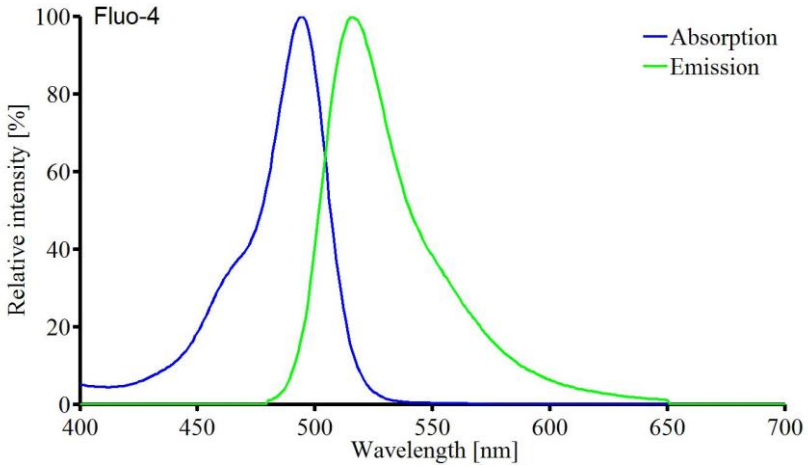

Figure III-4 Fluo-4 fluorescence spectra.

The excitation of the dye was ensured by a light emitting diode (4-Wavelength High-Power LED Source, Thorlabs) with an average power of 1 mW delivered (λ_{led}=470 nm). A 40X microscope objective with a numerical aperture of 0.6 (Olympus) was used to focus the excitation. The backward fluorescence emission (λ_{em}=516 nm) of Fluo-4 was collected by the same microscope objective before to pass through the multichroic mirror and to be detected with a 14 bit CCD camera (pixel matrix 512x512, iXon, AndorTM Technologies). A shortpass filter (λc=750 nm) was placed before the CCD camera to block the infrared light coming from the infrared exposure system. The acquisition parameters of the CCD and the LED emission

parameters were externally controlled with Winfluor and with an analog output from a digital acquisition (DAQ) board (USB-6229-BNC, National Instruments).

III.2.3. Infrared exposure

The infrared source used was a multimode laser diode (LU1470T015, Lumics), emitting in continuous wave mode at 1470 nm. The laser diode presents a fibered output with a 105 µm core diameter and a 0.15 numerical aperture. A cooling block (LU_CB_T_0, Lumics) was used to stabilize the temperature and an adapted power supply (LU_DR_AD, Lumics) controlled the exposure duration and the power of the emitted infrared radiation. The power supply was externally controlled with Winfluor. Thus, exposure parameters were controlled and the infrared exposure was synchronized with the fluorescence detection of intracellular calcium. The tip of the fiber was placed at a distance of 500 µm of the targeted cells, using a micromanipulator.

III.2.4. Pharmacological reagents and cell media preparation

To investigate on the possibility of triggering the IP_3 pathway by infrared exposure, different pharmacological reagents were used to block the IP_3 pathway at different stages of the process.

2-Aminoethoxydiphenylborane (2-APB, 1 mM), an IP_3-channel inhibitor was used to block the Ca^{2+} ion channels located in the membrane of the endoplasmic reticulum, activated by the binding of IP_3. U73122 (10 µM), an inhibitor of phospholipase C, was used to block the activity of PLC and consequently the release of IP_3 in the cytosol and all the process of release of Ca^{2+} ions from the endoplasmic reticulum. However U73122 is known to present a lot of side effects. Thus, we used its inactive analog, U73343 (10 µM), which presents the same side effects but does not inhibit PLC activity. Those different pharmacological reagents were diluted in 2 mL HBSS. Cells were pre-incubated with those solutions for 10 minutes. Before the experiments, petri dishes were washed twice with HBSS where $CaCl_2$ was omitted and replaced by the chelator EGTA (4 mM) to yield Ca^{2+} free medium. The use of Ca^{2+} free medium allows to ensure that the hypothetical increase of intracellular Ca^{2+} ion concentration observed originates from the release of Ca^{2+} ions from internal stores.

Thapsigargin (2 µM), a sarco/endoplasmic reticulum Ca^{2+}-ATPase pump (SERCA) inhibitor, was diluted in Ca^{2+} free HBSS medium. Cells were incubated in it for 20 min to deplete the internal ER Ca^{2+} stores, used in experiments detailed hereafter to ensure the lack of Ca^{2+} ions in the extracellular medium.

To investigate on the possible membrane permeabilization, YO-PRO-1, allowing assessment of such phenomenon, was diluted in HBSS (1 µM) and added at the start of imaging

experiments without pre-incubation. Healthy cells are impermeable to YO-PRO-1, however for apoptotic cells, the creation of pores in the plasma membrane allows this dye to come in the cell. When YO-PRO-1 enter in the cell, the fluorescence strongly increase. Thus, YO-PRO-1 fluorescence was measured following IR exposure. YO-PRO-1 fluorescence spectra (Figure III-5) are close to Fluo-4 fluorescence spectra, making its use very easy in our setup, without the need to change any filter.

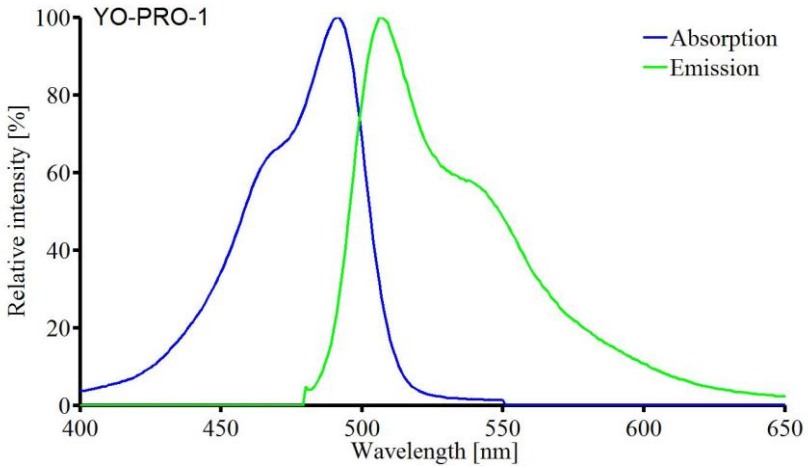

Figure III-5 YO-PRO-1 fluorescence spectra.

The detergent digitonin, as it effectively water-solubilizes lipids, was used to permeabilize the plasma membrane. It was thus used as a positive control experiment showing the ability of YO-PRO-1 to report membrane permeabilization. Digitonin was added in place of IR stimulation at a final working concentration of 100 µM.

III.2.5. Image analysis

The selection of the region of interest, defined as a single cell exposed to infrared radiation, and the extraction of the fluorescence over time were made with Winfluor. Raw fluorescence data were exported into Matlab to compute relative changes in Fluo4-AM fluorescence ($\Delta F/F_0$). F_0 denotes the fluorescence baseline before addition of the stimulus and $\Delta F=F-F_0$ denotes the change of fluorescence at each time point, reflecting the change of intracellular Ca^{2+} concentration changes. About 10 experiments were performed for each observation and treatment condition. Consequently, each of the result are expressed as the mean fluorescence +/- the standard deviation both calculated with Matlab.

III.2.6. Statistical analysis

In pharmacological studies, independent t-tests were performed with Matlab on the peak $\Delta F/F_0$ following IR stimulation in each condition. The t-test is a statistical test allowing to compare the means of two sample groups and to know if the means of the two sets of data are significantly

different in the statistical point of view. In our case, we want to compare two independent sets of data. Let's call the first set of data "A" and the second one "B". The t value of t-test is calculated with the relationship:

$$t = \frac{m_A - m_B}{\sqrt{\frac{{\sigma_A}^2}{n_A} + \frac{{\sigma_B}^2}{n_B}}} \qquad \textbf{Eq III-1}$$

Where:

- m_A and m_B denote the means of A and B respectively

- n_A and n_B denote the sizes of A and B respectively

- σ_A and σ_B denote the standard deviations of A and B respectively

The standard deviation σ_A is calculated by:

$$\sigma_A = \sqrt{\frac{\sum_{i=1}^{n_A}(x_i - m_A)^2}{n_A}} \qquad \textbf{Eq III-2}$$

Where x_i denote each data of the data set.

With the t value, the value of the degrees of freedom, d.f. is necessary. It is defined as

$$d.f. = n_A + n_B - 2 \qquad \textbf{Eq III-3}$$

We then use these values in the Student table (see 0). In the student table, going to the line corresponding to the degrees of freedom and searching the closest inferior t value, allows to find the right column to extract the corresponding p-value. The p-value represents the probability of falsely rejecting the null hypothesis. We consider in our case the null hypothesis as the hypothesis saying that the means are not different. For example if p=0.01, that means that we can reject the null hypothesis, and say that the two means of the data sets are different with a 1% of probability to be wrong, or with 1-p, 99 % of confidence. Usually, we can conclude that the means of two independent data sets are different with a statistically significance when p<0.005.

III.2.7. Calculation of the energy density deposited on cells

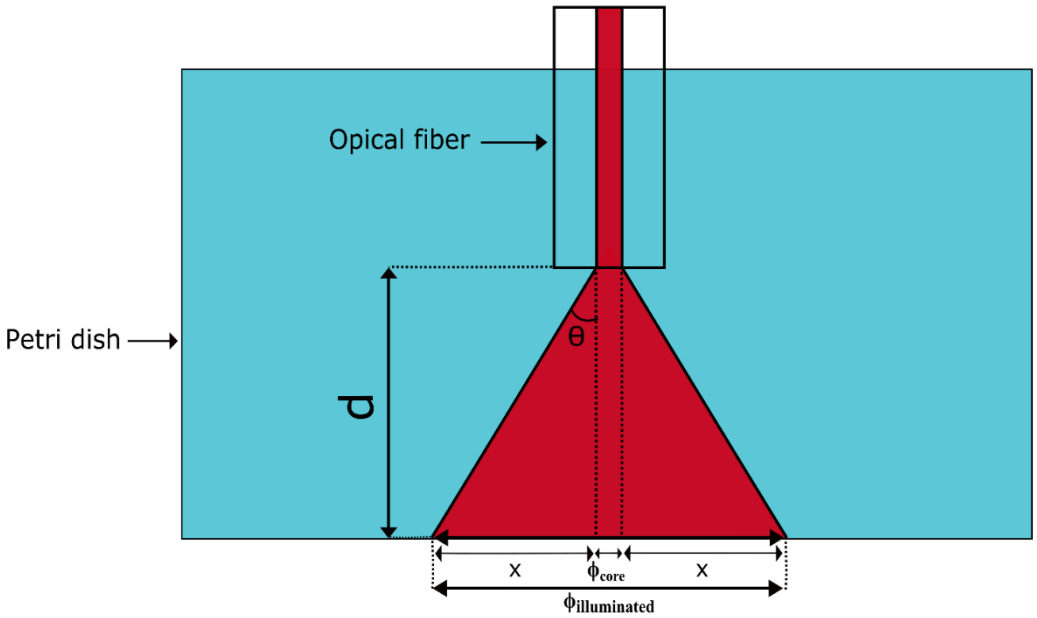

Figure III-6 Schematic representation of the area exposed to infrared in agreement with the numerical aperture of the fiber.

To calculate the energy density delivered to the cells during infrared exposures, we chose to consider the energy provided at the output tip of the fiber and the area illuminated at the bottom of the petri dish, where the cells are fixed.

By measuring the power at the output of the fiber, we can calculate the energy density dE delivered during an exposure to infrared.

$$dE = \frac{P \times t}{A} \qquad \textbf{Eq III-4}$$

Where:

- A denotes the area illuminated (m^2)

- P denotes the infrared power at the output of the fiber (Watts)

- t denotes the duration of the exposure (seconds)

And the area illuminated by

$$A = \pi \times \left(\frac{\phi_{illuminated}}{2}\right)^2 \qquad \textbf{Eq III-5}$$

According to the notation taken in Figure III-6, the diameter of the area illuminated is given by

$$\phi_{illuminated} = \phi_{core} + 2 \times x \quad \textbf{Eq III-6}$$

It remains to calculate x thanks to the numerical aperture NA. The numerical aperture is defined by:

$$NA = n \times \sin(\theta) \quad \textbf{Eq III-7}$$

Where:

- n denotes the refractive index of the medium (considered here as water, n=1.33)

- θ denotes the acceptance angle of the fiber (radians)

With simple trigonometry, the distance x represented on Figure III-6 may be calculated with:

$$x = d \times \tan(\theta) \quad \textbf{EqIII-8}$$

Where:

- d denotes the distance between the fiber tip and the bottom of the petri dish

By injecting Eq III-7 in EqIII-8 we have:

$$x = d \times \tan(\arcsin\left(\frac{NA}{n}\right)) \quad \textbf{Eq III-9}$$

Using it in Eq III-6 we obtain:

$$\phi_{illuminated} = \phi_{core} + 2 \times d \times \tan(\arcsin\left(\frac{NA}{n}\right)) \quad \textbf{Eq III-10}$$

Injecting Eq III-10 in Eq III-5 allows us to write:

$$A = \pi \times \left[\frac{\phi_{core}}{2} + d \times \tan(\arcsin\left(\frac{NA}{n}\right))\right]^2 \quad \textbf{Eq III-11}$$

By using Eq III-4 and Eq III-11, the calculation of the energy density delivered to the cell is given by:

$$dE = \frac{P \times t}{\pi \times \left[\frac{\phi_{core}}{2} + d \times \tan(\arcsin\left(\frac{NA}{n}\right))\right]^2} \quad \textbf{Eq III-12}$$

Finally, the absorption of water was taken into account with the use of Lambert's law and the absorption coefficient α (≈28 cm^{-1} at 1470 nm):

$$dE = \frac{P \times t}{\pi \times \left[\frac{\phi_{core}}{2} + d \times \tan(\arcsin\left(\frac{NA}{n}\right))\right]^2} \times e^{-\alpha \times d} \quad \textbf{Eq III-13}$$

III.2.8. Extracellular electrophysiology

Neural activity induces the increase of transmembrane currents that may be probed in the extracellular medium [82]. The extracellular field is shape mostly by synaptic transmembrane currents, but also substantially by Na^+ and Ca^{2+} spikes, or ionic fluxes through ion channels. Custom microelectrode arrays (MEAs) were used to perform extracellular electrophysiological recordings, see Figure III-7. The MEAs as well as the experiments led on it were performed within the bioelectronics department of the Ecole des Mines of Saint-Etienne. The MEAs consisted of 64 gold electrodes deposited on glass and spin-coated with poly(3,4-ethylenedioxythiophene) doped with poly(styrenesulfonate) (PEDOT:PSS), a conducting polymer with high conductivity [83]. Parylene-C[poly(para-chloroxylylene)] was used as insulating material because of its moisture, chemical and dielectric barrier properties.

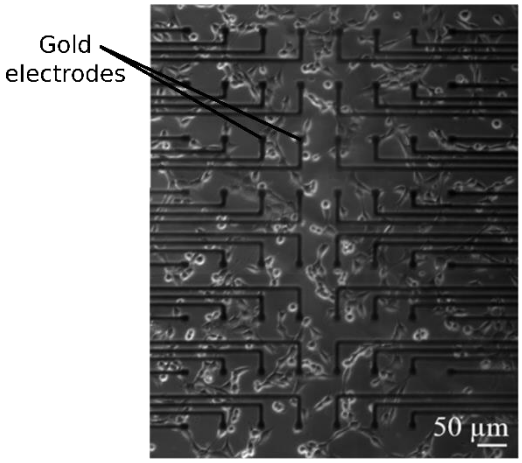

Figure III-7 Picture of a MEA seeded with HT22 cells.

Electrical recordings were acquired with a multi-channel amplifier system (RHD2000 series, Intan technologies) with digital output via USB interface, with a sampling rate of 35 kHz. Data were then notch filtered (50 Hz) to filter the electrical grid contribution, and processed by threshold detection to identify neural spikes induced by the infrared exposure and to extract the spike rate.

III.3. Infrared exposure induces dose dependent intracellular Ca^{2+} ions concentration transients

In a first time, dosimetry experiments were made to see the effect of both the energy density applied and the duration of the infrared exposure on the intracellular Ca^{2+} ion concentration increase. The same protocol was used for HT22 mouse hippocampal neurons and U87 glioblastoma cells. The results in the different kind of cells are finally compared.

III.3.1. Effect of the energy density

III.3.1.1. HT22 mouse hippocampal neurons

Infrared exposure triggered a change in the intracellular Ca^{2+} ions concentration which is dose dependent in HT22 mouse hippocampal neurons. Figure III-8 shows the dependency and the relationship existing between the infrared energy delivered to the cells and the fluorescence change, related to the intracellular Ca^{2+} ion concentration change. The duration of exposure was here set at 500 ms and the power of the infrared was varied between 75 mW and 275 mW by steps of 25 mW. This corresponds to energy densities delivered from 24.7 $J.cm^{-2}$ to 90.4 $J.cm^{-2}$.

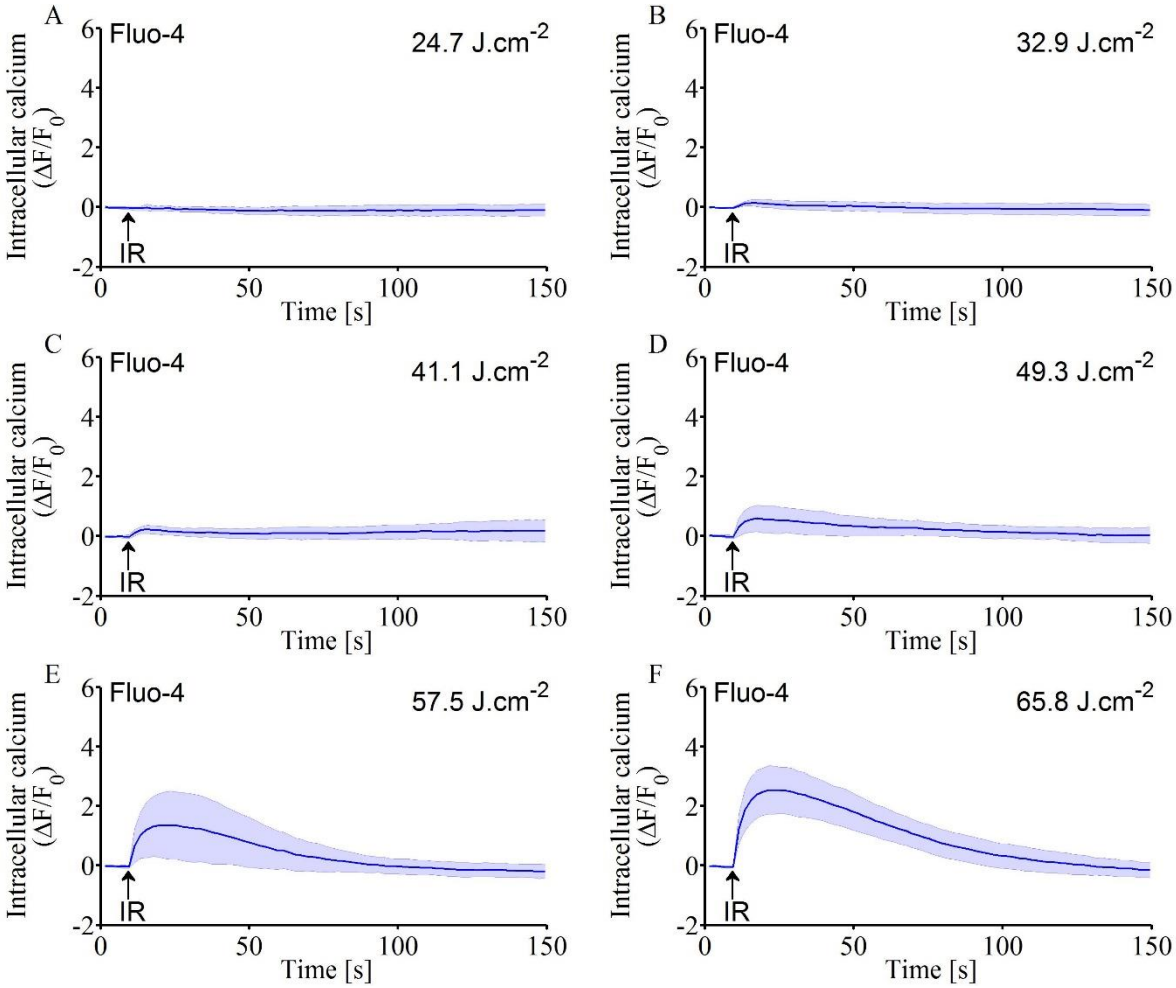

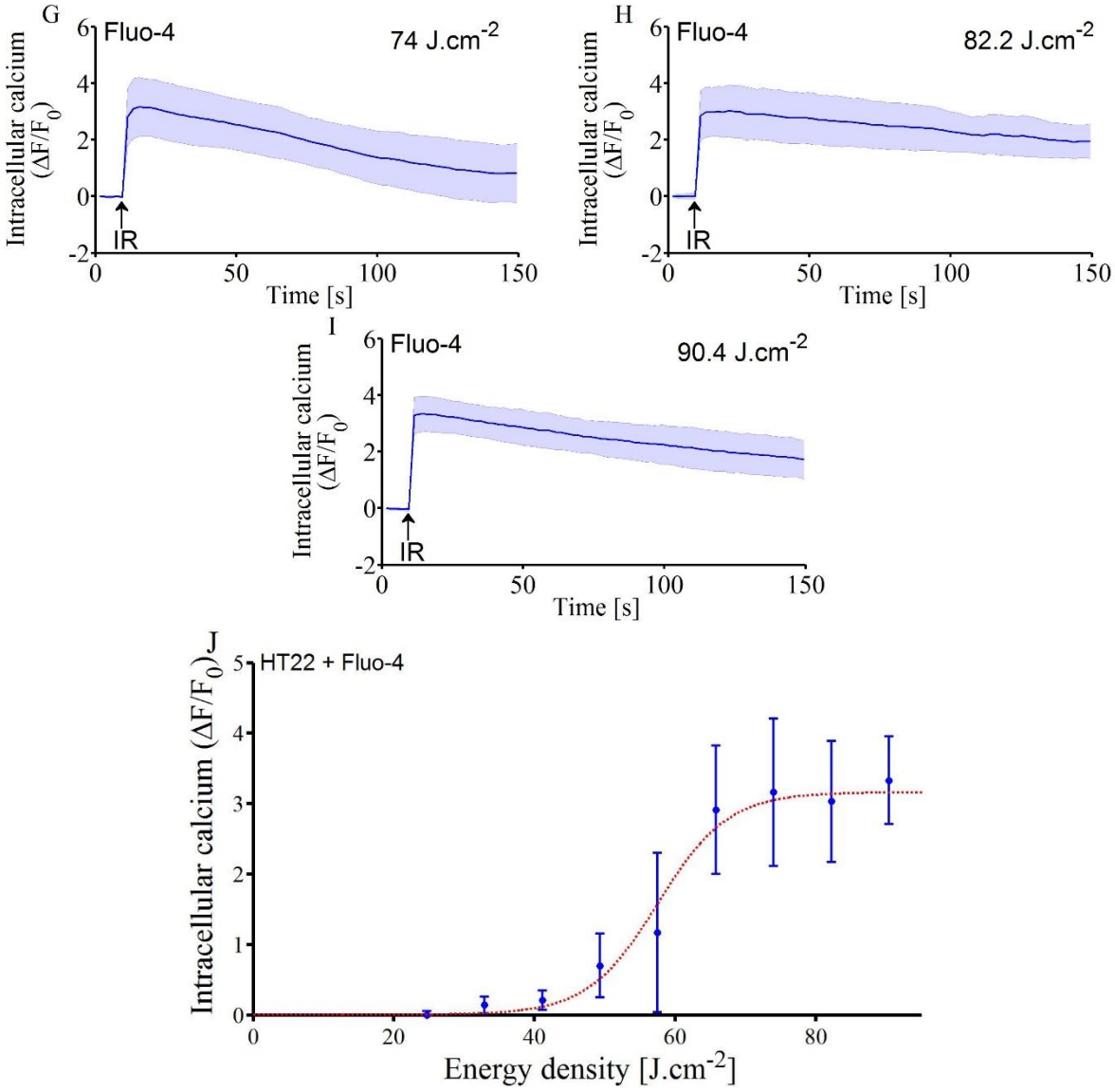

Figure III-8 The change in the Fluo4-AM fluorescence reporting intracellular Ca^{2+} ions concentration changes in HT22 mouse hippocampal neurons followed a sigmoidal dose-response relationship with the infrared energy density delivered to the cells. A to I. Exposure from 24.7 $J.cm^{-2}$ to 90.4 $J.cm^{-2}$. J. Sigmoidal relationship between the magnitude of the peak of change in the intracellular Ca^{2+} ions concentration and the energy delivered.

Qualitatively, it is obvious that when the energy density of the infrared exposure was increased, the intracellular Ca^{2+} ions concentration was increased. Further, the time to go back to the intracellular Ca^{2+} ions concentration baseline was longer with higher energy densities.

The thermal effect in HT22 mouse hippocampal neurons was investigated in chapter 2. Table III-1 reminds the temperature increases measured with RhB for the different energy densities applied.

Table III-1 Remind of the temperature changes induced by infrared exposure, measured in HT22 mouse hippocampal neurons with Rhodamine B.

Energy density (J.cm^{-2})	Temperature reached (°C)	ΔT (°C)
24.7	49.2	12.2
32.9	51.6	14.6
41.1	53.4	16.4
49.3	54.9	17.9
57.5	56.1	19.1
65.8	57.6	20.6
74.0	58.7	22.7
82.2	60.0	23.0
90.4	61.4	24.4

With our setup and 500 ms exposures, the threshold to see intracellular Ca^{2+} transients was approximately 32.9 J.cm^{-2} corresponding to an increase of temperature of about 14.6 °C. By reporting the peak values of the relative changes in the Fluo4-AM fluorescence in function with the energy density delivered, a sigmoidal relationship was found between the magnitude of change in the intracellular Ca^{2+} ions concentration and the energy delivered. The maximal change in intracellular Ca^{2+} ions concentration corresponded to a relative change in Fluo4-AM fluorescence of about 3.5 fold, following infrared exposure with energy densities of 74 J.cm^{-2} and higher. The half maximal effective energy density (EC_{50}), defined as the energy density inducing a response halfway between the baseline and the maximum, was approximately 58 J.cm^{-2}.

III.3.1.2. U87 human glioblastoma cells

Infrared exposure triggered a change in the intracellular Ca^{2+} ions concentration which is dose dependent in U87 human glioblastoma cells, as in HT22 mouse hippocampal neurons. Figure III-9 shows the dependency and the relationship existing between the infrared energy delivered to the cells and the intracellular Ca^{2+} ions concentration change. The same parameters were used as previously, to compare the intracellular Ca^{2+} ions concentration induced in electrically and non-electrically excitable cells.

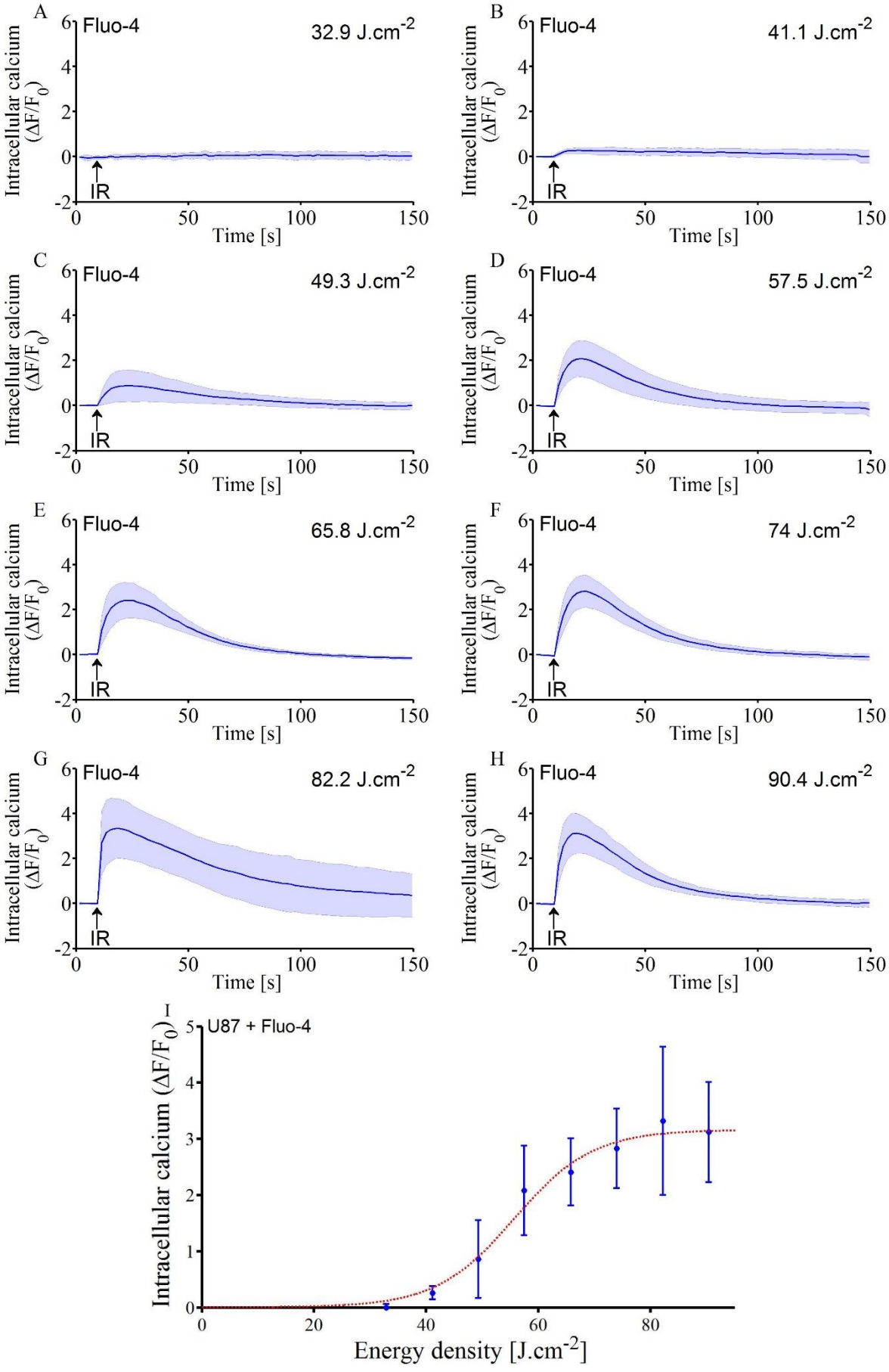
A
Fluo-4
32.9 J.cm-2
B
41.1 J.cm-2
C
49.3 J.cm-2
D
57.5 J.cm-2
E
65.8 J.cm-2
F
74 J.cm-2
G
82.2 J.cm-2
H
90.4 J.cm-2
IR
Time [s]
Intracellular calcium (ΔF/F0)
I
U87 + Fluo-4
Intracellular calcium (ΔF/F0)
Energy density [J.cm-2]

Figure III-9 The change in the Fluo4-AM fluorescence reporting intracellular Ca^{2+} ions concentration changes in U87 human glioblastoma cells followed a sigmoidal dose-response relationship with the infrared energy density delivered to the cells. A to H. Exposure from 32.9 $J.cm^{-2}$ to 90.4 $J.cm^{-2}$. J. Sigmoidal relationship between the magnitude of the peak of change in the intracellular Ca^{2+} ions concentration and the energy delivered.

Basically the same observations that for HT22 mouse hippocampal neurons were made here. When the energy density of the infrared exposure was increased, the intracellular Ca^{2+} ions concentration was increased. Here, no intracellular Ca^{2+} transient was found with energy density of 32.9 $J.cm^{-2}$. Consequently, the threshold to see intracellular Ca^{2+} transients was here approximately 41.1 $J.cm^{-2}$. A similar sigmoidal relationship was found between the magnitude of change in the intracellular Ca^{2+} ions concentration and the energy delivered. The maximal change in intracellular Ca^{2+} ions concentration corresponded to a relative change in Fluo4-AM fluorescence of about 3.5 fold, following infrared exposure with energy densities of 82.2 $J.cm^{-2}$ and above. The half maximal effective energy density (EC_{50}) was around 56 $J.cm^{-2}$.

III.3.2. Effect of the exposure duration

III.3.2.1. HT22 mouse hippocampal neurons

Figure III-10 shows the dependency and the relationship existing between the infrared exposure duration and the intracellular Ca^{2+} ions concentration change in HT22 mouse hippocampal neurons. Here the power at the output of the fiber was maintained at 275 mW, the higher of the previous study. The exposure duration was varied from 50 ms to 500 ms.

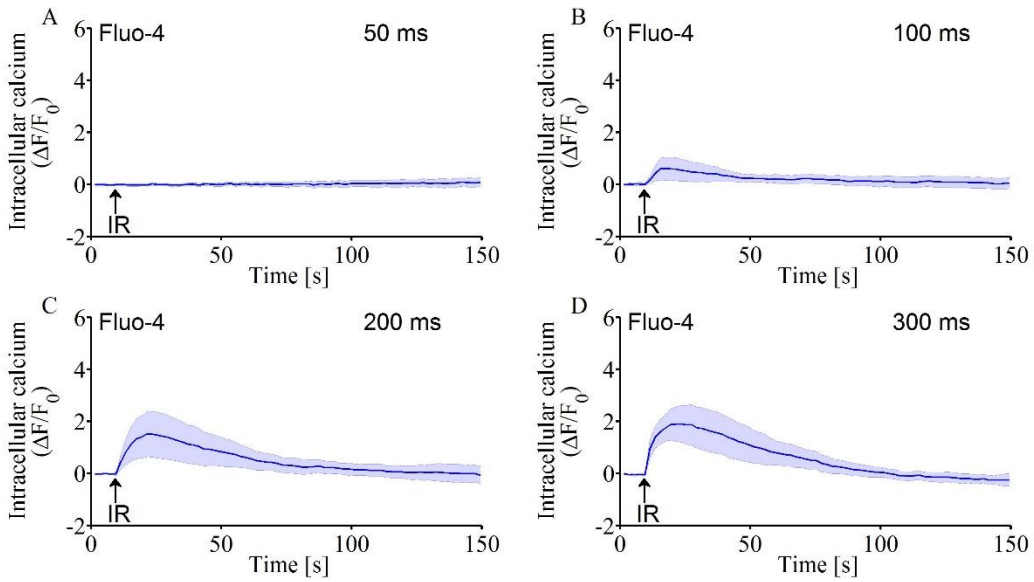

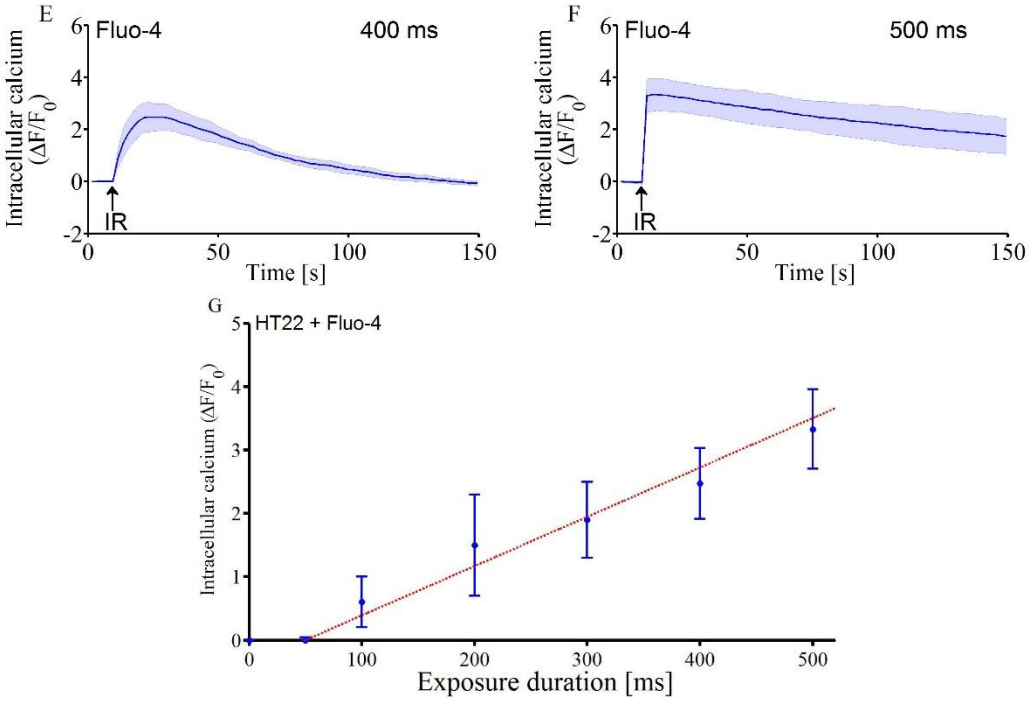

Figure III-10 The change in the Fluo4-AM fluorescence reporting intracellular Ca^{2+} ions concentration changes in HT22 mouse hippocampal neurons followed a linear relationship with the infrared exposure duration. A to F. Exposure duration from 50 ms to 500 ms. G. Linear relationship between the magnitude of the peak of change in the intracellular Ca^{2+} ions concentration and the exposure duration.

With 50 ms exposure duration, no intracellular Ca^{2+} ion concentration increase was found, the threshold to see a response following infrared exposure being 100 ms with our setup. Above those 100 ms the exposure duration was increased by steps of 500 ms. When the duration of exposure was increased, the intracellular Ca^{2+} ions concentration changes were found to be greater. By reporting the peak values of the relative changes in the Fluo4-AM fluorescence in function with the exposure duration, a linear relation was found between the magnitude of change in the intracellular Ca^{2+} ions concentration and the duration of exposure, over the range of durations tested.

III.3.2.2. U87 human glioblastoma cells

Figure III-11 shows the dependency and the relationship existing between the infrared exposure duration and the intracellular Ca^{2+} ions concentration change in HT22 mouse hippocampal neurons. The same exposure parameters were used here that for HT22 mouse hippocampal neurons.

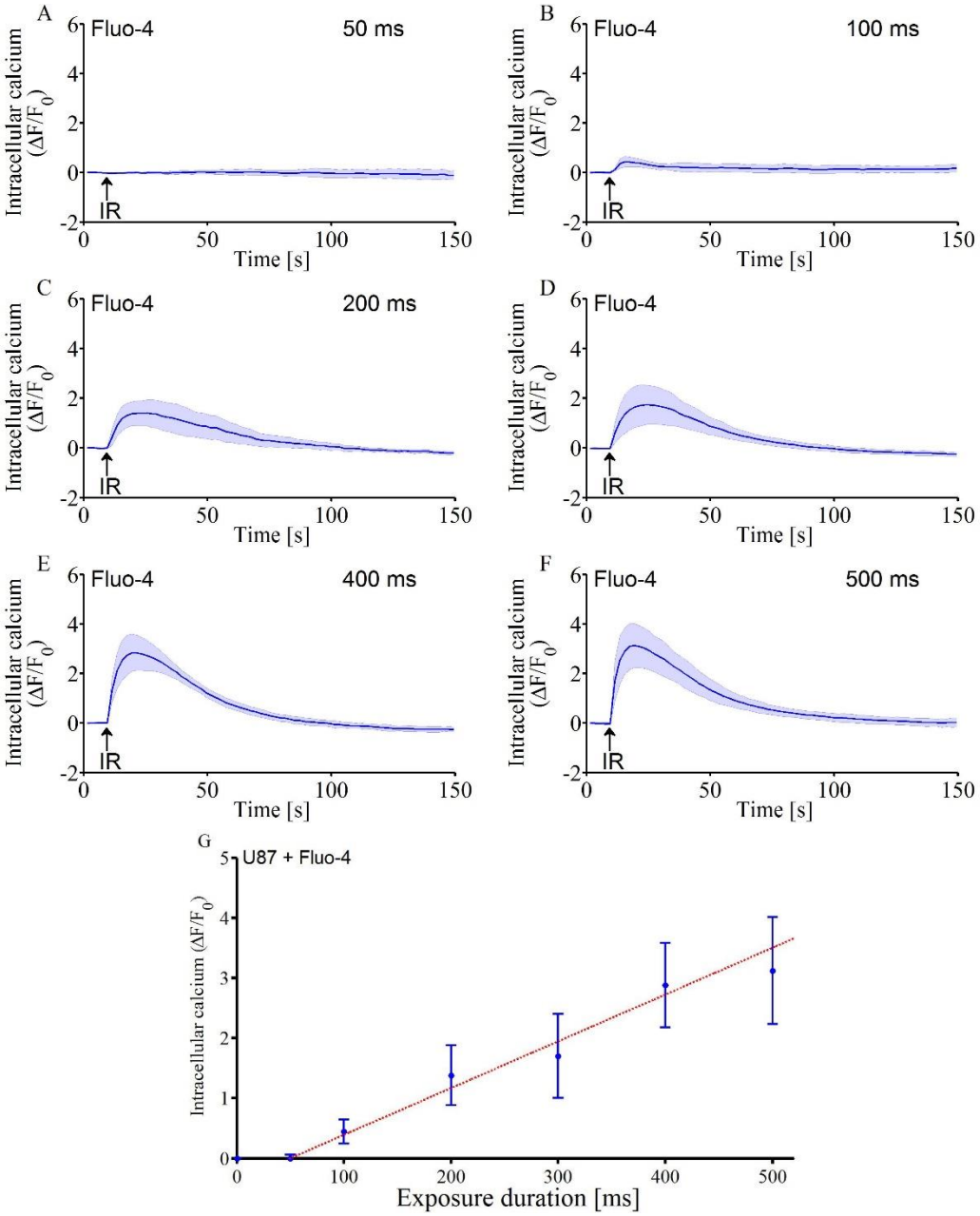

Figure III-11 The change in the Fluo4-AM fluorescence reporting intracellular Ca^{2+} ions concentration changes in U87 human glioblastoma cells followed a linear relationship with the infrared exposure duration. A to F. Exposure duration from 50 ms to 500 ms. G. Linear relationship between the magnitude of the peak of change in the intracellular Ca^{2+} ions concentration and the exposure duration.

As for the electrically excitable cells, when the duration of exposure was increased, the intracellular Ca^{2+} ions concentration changes were found to be greater in U87 cells. A similar linear relation was found between the magnitude of change in the intracellular Ca^{2+} ions concentration and the duration of exposure.

III.3.3. Comparison between HT22 mouse hippocampal neurons and U87 human glioblastoma cells

In the results presented up to now in this chapter, the ability of infrared exposure to trigger intracellular Ca^{2+} ions transients has been demonstrated in both HT22 mouse hippocampal neurons and U87 human glioblastoma cells, which are respectively electrically and non-electrically excitable cells. Similarities and small differences have been found between the two types of cells, which are reported in Table III-2. This indicates that the mechanism responsible for the intracellular Ca^{2+} ion concentration increase induced by infrared exposure does not depend on the electrically excitable character of the cell.

Table III-2 Comparison in the measurements of intracellular Ca^{2+} ions concentration between HT22 mouse hippocampal neurons and U87 human glioblastoma cells in function with the energy density delivered and with the exposure duration.

Cell type	HT22 mouse hippocampal neurons	U87 human glioblastoma cells
Energy density threshold to see $[Ca^{2+}]$ changes with a 500 ms exposure	32.9 $J.cm^{-2}$	41.1 $J.cm^{-2}$
Dependence form of the peak of $[Ca^{2+}]$ with the energy density	Sigmoidal	Sigmoidal
Maximum fluorescence change ($\Delta F/F0$)	≈ 3.5 fold	≈ 3.5 fold
Maximum fluorescence change threshold	74 $J.cm^{-2}$	82.2 $J.cm^{-2}$
EC_{50}	58 $J.cm^{-2}$	56 $J.cm^{-2}$
Exposure duration threshold to see $[Ca^{2+}]$ changes with infrared exposure at 275 mW	100 ms	100 ms
Dependence form of the peak of $[Ca^{2+}]$ with the exposure duration	Linear	Linear

III.3.4. Cell morphology conservation

The possible cell morphology changes, like blebbing or swelling known as cellular damages, were investigated in U87 human glioblastoma cells exposed to infrared radiation during 500 ms with an energy density of 90.4 $J.cm^{-2}$. The exposure was triggered at t = 10 s.

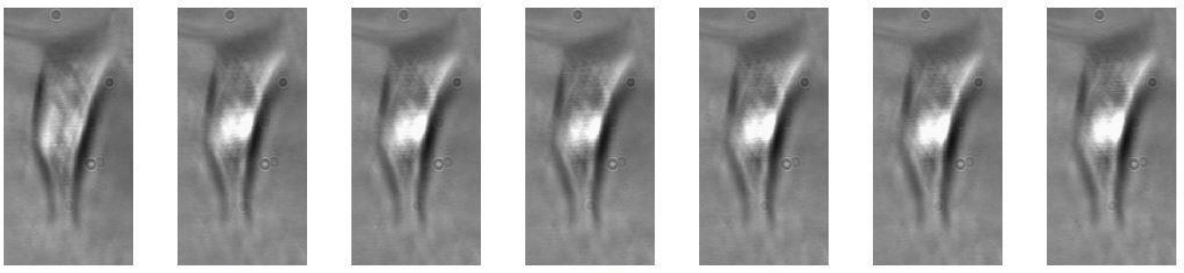

Figure III-12 Investigation of possible cell swelling in U87 human glioblastoma cells exposed to 500 ms infrared with 90.4 J.cm^{-2} energy density

As a result, no significant change in the cell morphology was found following the infrared exposure and during 10 minutes post-exposure, indicating that the infrared exposure did not induced damages to the cell resulting in morphological change.

III.4. Pharmacological study of the infrared-induced calcium signaling in HT22 and U87 cells

To understand the mechanism involved in the intracellular Ca^{2+} ion concentration increase induced by infrared exposure, a pharmacological approach was used. To pharmacologically dissect the source of the Ca^{2+} signals induced by infrared exposure, the parameters of infrared exposure were chosen according to the results concerning the dependence of the intracellular Ca^{2+} signals with the IR exposure duration and energy density. The infrared exposure duration was fixed at 500 ms, and the infrared power at 275 mW (energy density of 90.4 J.cm^{-2}), to determine whether IR exposure caused permeabilization of the plasma membrane.

III.4.1. HT22 mouse hippocampal neurons

To see the differences in intracellular Ca^{2+} signal when the cell is exposed or not to infrared radiation, Fluo-4 fluorescence was recorded in HT22 cells exposed to a single 500 ms infrared exposure and in HT22 cells at rest, without any infrared exposure. Experiments in both conditions were repeated 10 times and averaged, see Figure III-13.

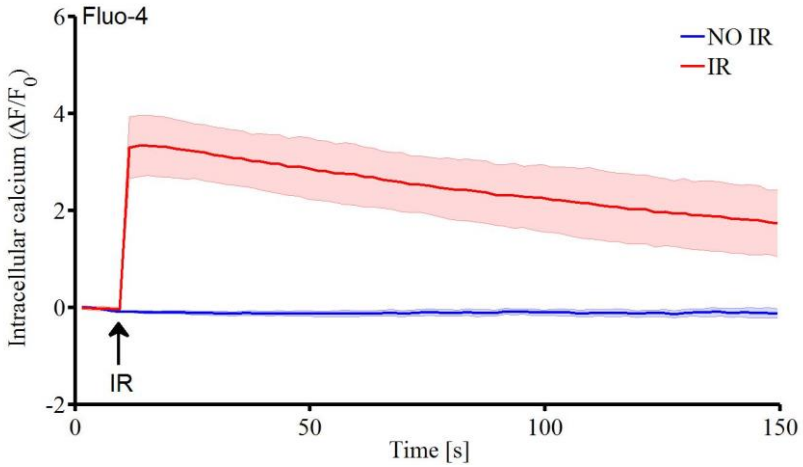

Figure III-13 Intracellular calcium variation in HT22 cells induced by exposure to infrared compared to control experiments without any exposure

The application of infrared exposure resulted in a strong change in the fluorescence of the dye Fluo-4. This indicates that there was a strong change in the intracellular Ca^{2+} ions concentration induced by the optical exposure. In the control experiments, where cells were not exposed to infrared radiation, fluorescence was found to be pretty stable, indicating that

the acquisition parameters allowed to probe the fluorescence without photobleaching, and that there was no spontaneous calcium signals.

Then, the possibility that infrared exposure cause the permeabilization of the plasma membrane has been investigated with YO-PRO-1 (1µM), as shown in Figure III-14.

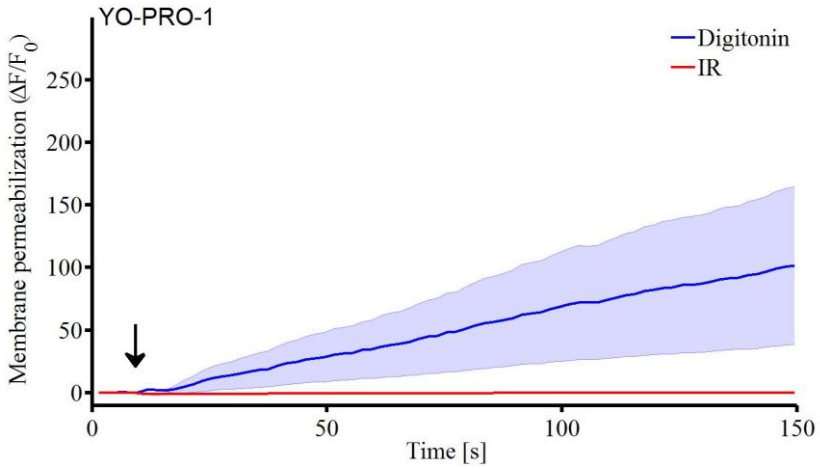

Figure III-14 Membrane permeabilization test performed by YO-PRO-1 fluorescence measurement in HT22 cells exposed to infrared radiation. The membrane permeabilization agent digitonin is used as a positive control.

In response to the infrared exposure, no increase in the YO-PRO-1 intracellular fluorescence was reported. That means that YO-PRO-1 did not pass through the plasma membrane under the influence of infrared, meaning that infrared did not permeabilize the cell membrane. In the positive control experiment, where digitonin, a membrane permeabilization agent, is added to the bath, there is a significant increase in the YO-PRO-1 fluorescence, showing this dye ability to report plasma membrane permeabilization. So the energy density delivered by those infrared exposures of 500 ms is sufficient to elicit strong intracellular Ca^{2+} concentration increase, but not strong enough to observe membrane permeabilization.

Once the membrane permeabilization studied, the origin of the intracellular Ca^{2+} signal was investigated, see Figure III-15. The aim of the experiment is to determine whether the infrared-induced Ca^{2+} signal was originating from an entry of the ions in the cells from the external medium or from a release from intracellular organelles. In this way, experiments were performed with cells in HBSS without any Ca^{2+} ions, replaced by EGTA, a calcium chelator. Thus the medium is a Ca^{2+} free medium.

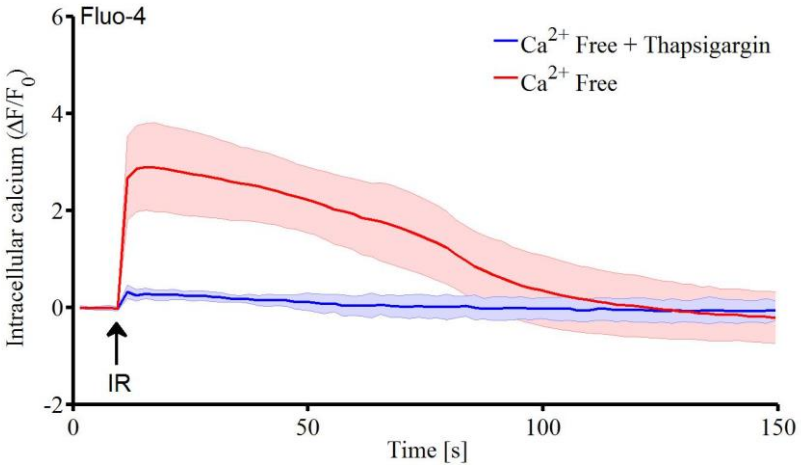

Figure III-15 Infrared-induced Ca^{2+} transients in HT22 cells are due to a release of Ca^{2+} ions from the intracellular organelles.

When the extracellular calcium is removed, the infrared-induced Ca^{2+} transient is still present, suggesting that the Ca^{2+} response takes its origin in the intracellular organelles. To confirm this theory, the SERCA pump inhibitor thapsigargin was used in five other experiments. Here, the HT22 cells were preincubated in Ca^{2+} free HBSS and thapsigargin (2 µM) in order to deplete the endoplasmic reticulum Ca^{2+} stores. In these conditions, after the incubation, the application of the infrared exposure did not result in any Ca^{2+} transient, suggesting the involvement of the endoplasmic reticulum.

Figure III-16 shows the results of further experiments with 2-APB. 2-APB, an inhibitor of IP_3 channels and Ca^{2+} release from the endoplasmic reticulum, was added to the Ca^{2+} free HBSS medium with a concentration of 1 mM.

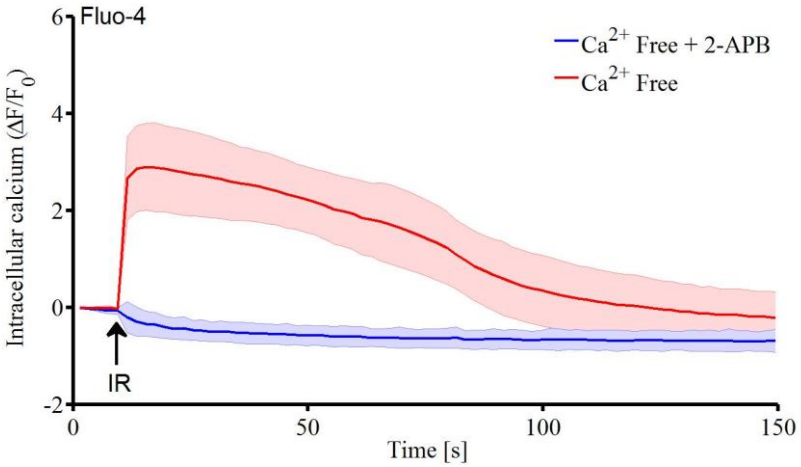

Figure III-16 Inhibition of IP_3 channels and Ca^{2+} release from the endoplasmic reticulum prevented the infrared-induced Ca^{2+} transient in HT22 cells.

As a result, the addition of 2-APB in the medium prevented the infrared-induced Ca^{2+} transient. This confirmed the main involvement of the release of Ca^{2+} ions from the endoplasmic reticulum in the infrared response.

Then, to see whether if infrared acted directly on the endoplasmic reticulum or if it was mediated by the Phospholipase C triggering the IP_3 pathway, a series of experiment was performed with U73122 (10 µM in Ca^{2+} free HBSS medium) and U73343 (10 µM in Ca^{2+} free HBSS medium). U73122 is known to inhibit the activity of phospholipase C. It presents also some side effects. Those side effects are shared by U73343, which does not block phospholipase C activity. Figure III-17 presents the results obtained.

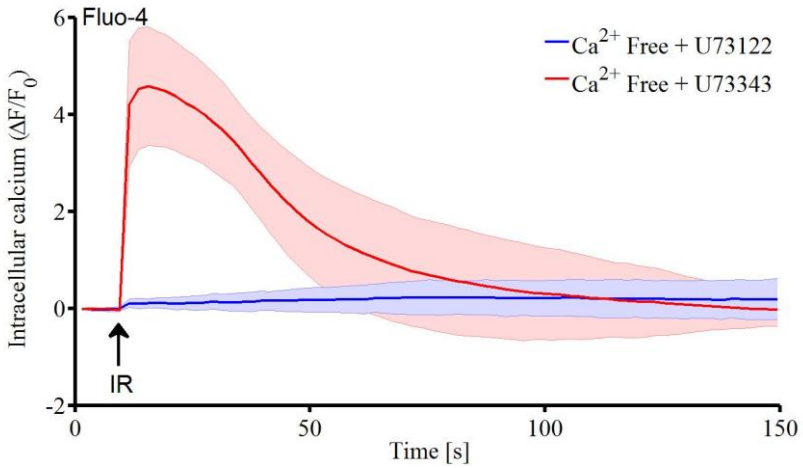

Figure III-17 Inhibition of the phospholipase C activity prevented the infrared-induced Ca^{2+} transient in HT22 cells.

The inhibition of the phospholipase C activity significantly blocked the infrared- induced Ca^{2+} release. Negative control experiments performed with the inactive analog, U73343, did not prevent the Ca^{2+} release, showing the necessity of the phospholipase C in the infrared response. Together, these results confirmed that infrared stimulation activates the phospholipase C and the IP_3 signaling pathway, leading to the release of Ca^{2+} ions from the intracellular stores of the cell.

We also investigated whether we observed similar intracellular Ca^{2+} responses with shorter pulses operating in the thermal confinement regime. As explained in Chapter I, thermal confinement regime happens when the duration of the infrared pulse duration t_p respects the relationship, $t_p \leq \delta^2/4\kappa$ [6], [84], where δ is the smallest dimension of heated volume, here defined by the radius of the fiber core, and κ the thermal diffusivity of water, $\kappa \approx 1.3 \times 10^{-3}$ cm^2/s. With a fiber core radius of 52.5 µm, this gives a maximum laser exposure duration of about 5 ms to respect thermal confinement. Thus a single 4 ms infrared exposure was applied, with a distance of 200 µm between the fiber tip and the cells, and a delivered energy density of 10.4 $J.cm^{-2}$. Figure III-18 shows that the application of short exposures resulted in a similar

intracellular Ca^{2+} response, in terms of latency and strength, when compared with 500 ms exposures, operating in the non-confinement regime. Thus, in our experiments, thermal confinement does not appear to be necessary to trigger HT22 mouse hippocampal neural function.

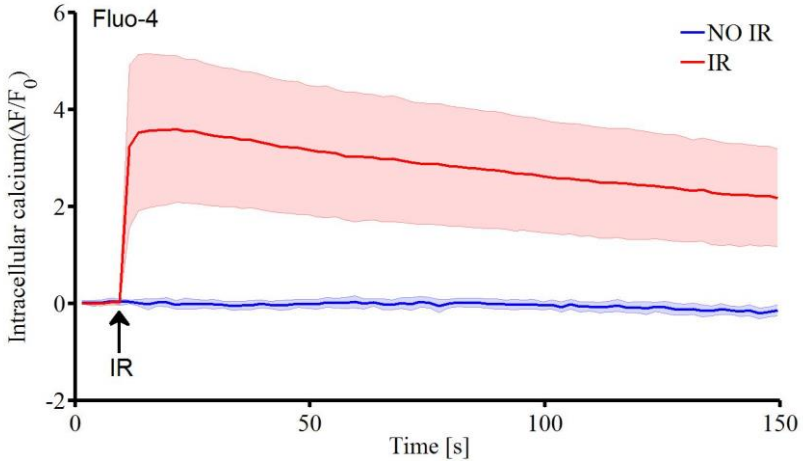

Figure III-18 Infrared stimulation of hippocampal neurons leads to an increase in Ca^{2+} release from ER stores. A significant change in Fluo-4 signal was observed in HT22 cells receiving a 4 ms IR exposure when compared to control experiments without infrared exposure.

III.4.2. Extracellular electrophysiology

Extracellular electrophysiology is another way to investigate on the stimulation of HT22 mouse hippocampal neuronal functions. It allows to electrically probe the changes in membrane depolarization associated with action potentials. Custom microelectrodes arrays were used, to show whether action potentials, or extracellular spikes, followed 4 ms infrared exposure in these cells. The infrared exposure resulted in a strong and slow electrical artifact (see Figure III-19.A). Thus, to minimize these artifacts the energy density delivered was divided by a factor of 2. Figure III-19.B shows the presence or not of spikes and their timing and rate induced by multiple 4 ms infrared exposures with an energy density delivered of 5.2 $J.cm^{-2}$ per pulse. The reversibility and reproducibility was also shown by the repeated exposures at 0.05 Hz. It should be noted that while IR induced artifacts could be removed by digital filtering, they are commonly seen in optogenetics.

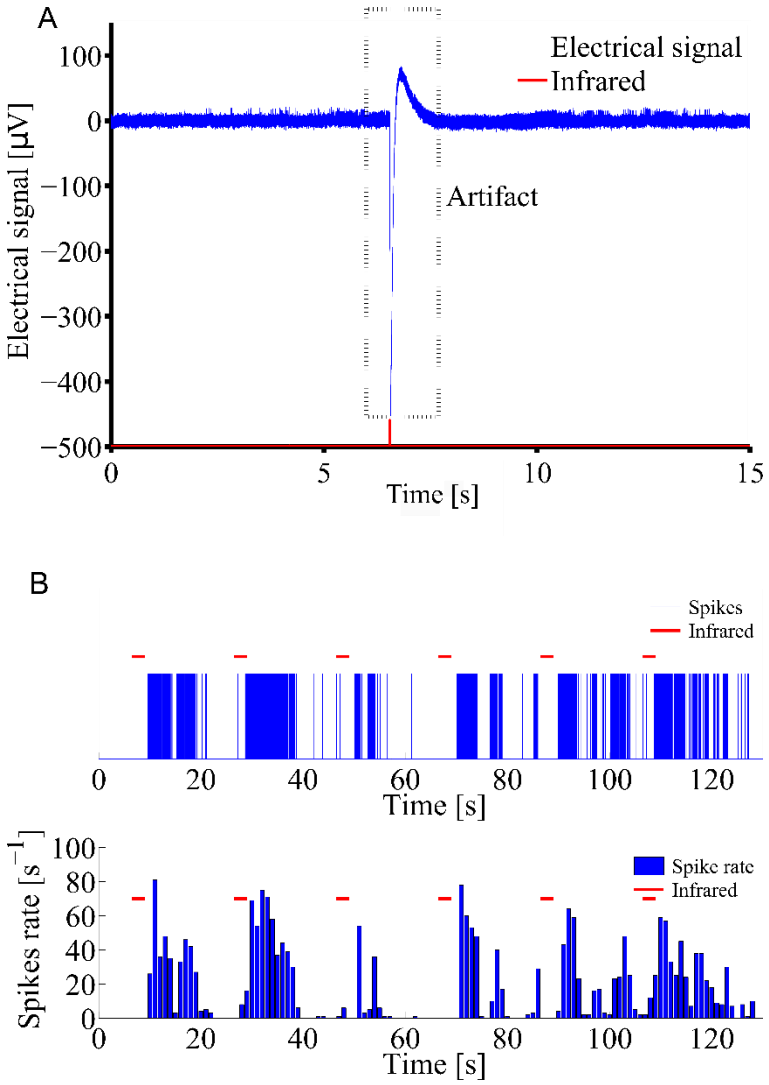

Figure III-19 Infrared exposure of HT22 mouse hippocampal neurons triggers electrical spikes from these neurons. A. Exposure to 5.2 J.cm^{-2} infrared radiation during 4 ms induced an artifact in the recorded signal. B. Filtered and processed data by threshold detection showing spike timing following repeated exposure to 5.2 J.cm^{-2} infrared radiation at 4 ms, operating in the confinement regime.

These results confirm the stimulation of neural functions in HT22 mouse hippocampal neurons by infrared exposure. However, such measurements have limitations compared to calcium imaging. For each electrode, the possibility to have more than one cell contribution in the electrical signal is not to be excluded. Thus, a spike ordering process should be used to isolate the possible contributions of each cell involved in the response. Furthermore, the strong and slow artifact, probably due to a thermal effect on the electrode, is not present in calcium imaging experiments, inducing less complexity in the data processing.

III.4.3. U87 human glioblastoma cells

The same protocol that for HT22 mouse hippocampal neurons were used in U87 human glioblastoma cells to investigate on the source of the Ca^{2+} signals The infrared power was still fixed at 275 mW during the 500 ms of exposure (energy density of 90.4 $J.cm^{-2}$).

In the same way, the ability of the infrared radiation to induce intracellular Ca^{2+} signal was highlighted by recording Fluo-4 fluorescence in U87 cells exposed to infrared and in U87 cells at rest, without any exposure. Experiments in both conditions were repeated 10 times.

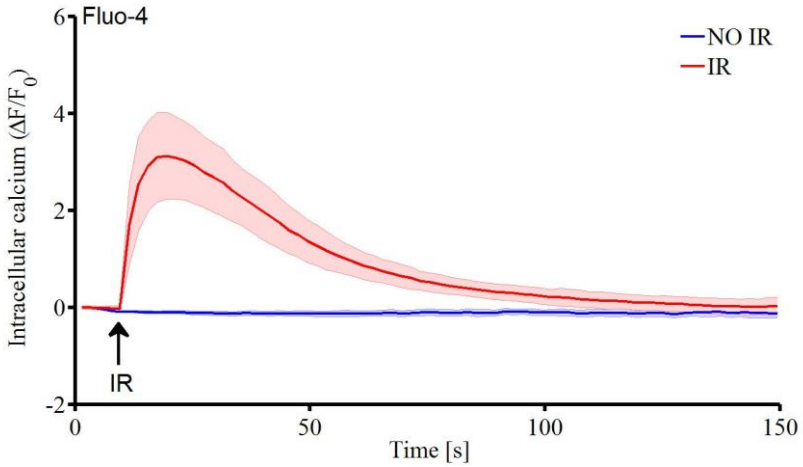

Figure III-20 Intracellular calcium variation in U87 cells induced by exposure to infrared compared to control experiments without any exposure

The application of infrared exposure resulted here again in a strong change in the fluorescence of the dye Fluo-4, indicating a strong change in the intracellular Ca^{2+} ions concentration. The control experiments highlighted that the acquisition parameters allowed to probe the fluorescence without photobleaching, neither spontaneous calcium signals.

YO-PRO-1 (1µM) was then used to see if infrared exposure cause the permeabilization of the plasma membrane.

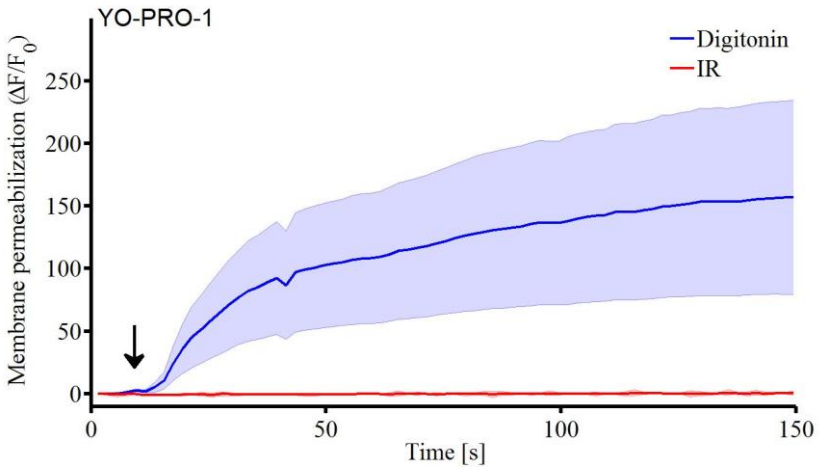

Figure III-21 Membrane permeabilization test performed by YO-PRO-1 fluorescence measurement in U87 cells exposed to infrared radiation. The membrane permeabilization agent called digitonin is used as a positive control.

In response to the infrared exposure, no increase in the YO-PRO-1 intracellular fluorescence was reported, indicating an absence of plasma membrane permeabilization. In the positive control experiment with digitonin, there was a significant increase in the YO-PRO-1 fluorescence. As for HT22 cells, the energy density delivered to U87 cells is sufficient to elicit intracellular Ca^{2+} concentration increase, but not strong enough to observe membrane permeabilization.

To see whether the origin of the intracellular Ca^{2+} signal in U87 cells was the same that in the HT22 cells, intracellular Ca^{2+} signal were measured in U87 cells in Ca^{2+} free medium with and without thapsigargin (2µM).

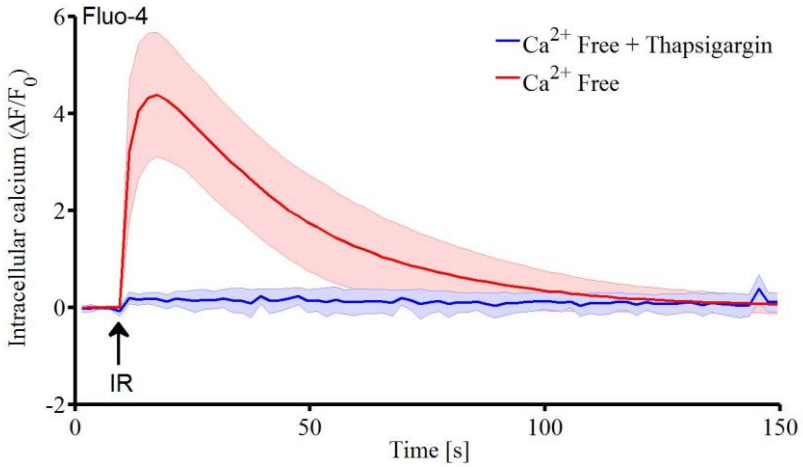

Figure III-22 Infrared-induced Ca^{2+} transients in U87 cells are due to a release of Ca^{2+} ions from the intracellular organelles

When the extracellular calcium is removed, the infrared-induced Ca^{2+} transient is still there, but was prevented with the use of thapsigargin. This suggests that the Ca^{2+} response takes its origin in the intracellular organelles like in the endoplasmic reticulum.

Further experiments with 2-APB (1mM) were also performed in Ca^{2+} free HBSS medium.

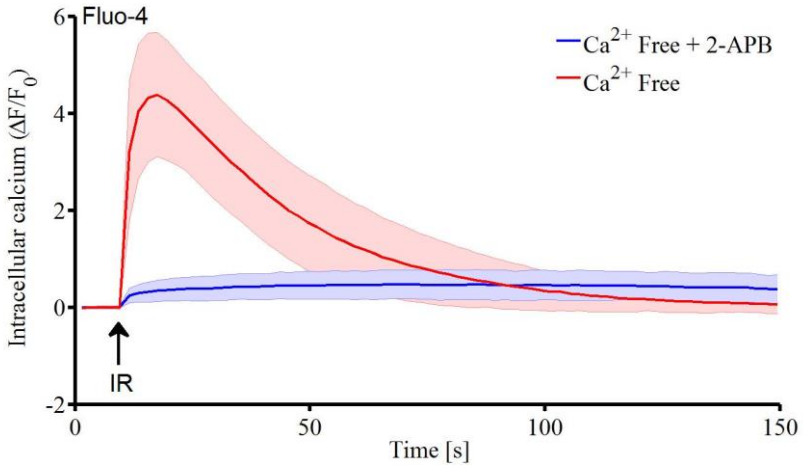

Figure III-23 Inhibition of IP_3 channels and Ca^{2+} release from the endoplasmic reticulum prevented the infrared-induced Ca^{2+} transient in U87 cells.

As a result, the addition of 2-APB in the medium prevented the infrared-induced Ca^{2+} transient. This confirmed the main involvement of the release of Ca^{2+} ions from the endoplasmic reticulum in the infrared response.

Then, to see whether if infrared acted directly on the Phospholipase C as in HT22 cells, a series of experiment was performed with U73122 (10 µM in Ca^{2+} free HBSS medium) and U73343 (10 µM in Ca^{2+} free HBSS medium).

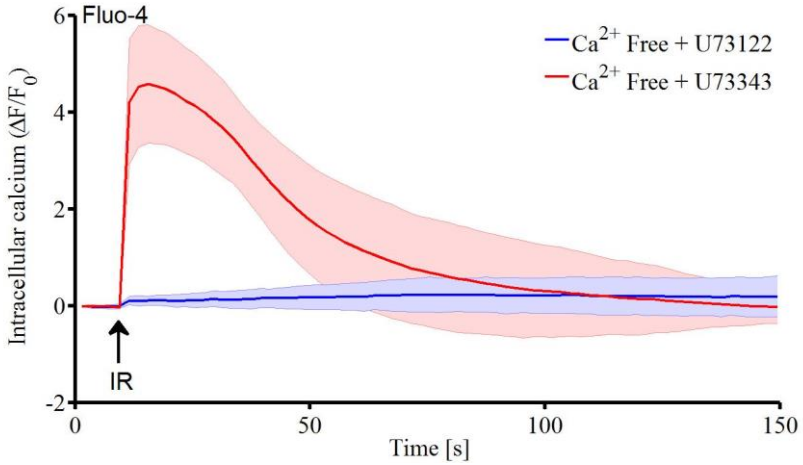

Figure III-24 Inhibition of the phospholipase C activity prevented the infrared-induced Ca^{2+} transient in U87 cells.

The inhibition of the phospholipase C activity with U73122 significantly blocked the infrared-induced Ca^{2+} release. Negative control experiments performed with U73343 had no effect on the Ca^{2+} release, showing the necessity of the phospholipase C in the infrared response. These results confirmed that infrared stimulation activates the phospholipase C and the IP_3 signaling pathway, leading to the release of Ca^{2+} ions from the intracellular stores of the cell.

III.4.4. Statistically analysis

The statistically significance of the previous results were investigating by the performance of t-tests. Table III-3 recapitulates the t-values, freedom degrees, and p-values associated to the t-tests. It should be noted that the Matlab function 'ttest2' gave us the exact p-values associated with the t-tests, allowing to know if the data sets compared are significantly statistically different.

Table III-3 Statistical analysis of the significance of the pharmacological studies.

Sets of data compared	HT22 mouse hippocampal neurons			U87 human glioblastoma cells		
	|t-value|	d.f.	p-value	|t-value|	d.f.	p-value
Infrared / No infrared (Fluo-4, Figure III-13 and Figure III-20)	15.74	18	$7.24\ e^{-8}$	11.59	18	$9.91\ e^{-7}$
Infrared / digitonin (YO-PRO1, Figure III-14 and Figure III-21)	4,56	17	$1.85\ e^{-3}$	5.7	17	$4.51\ e^{-4}$
EGTA / EGTA + Thapsigargin (Fluo-4, Figure III-15 and Figure III-22)	8.34	11	$4.96\ e^{-5}$	9.97	13	$1.69\ e^{-6}$
EGTA / EGTA + 2-APB (Fluo-4, Figure III-16 and Figure III-23)	9.05	16	$1.32\ e^{-5}$	9.48	18	$3.52\ e^{-6}$
U73122 / U73343 (Fluo-4, Figure III-17 and Figure III-24)	6.54	28	$9.01\ e^{-5}$	11.36	18	$9.45\ e^{-7}$

The statistical analysis showed us that in all the pharmacological studies performed, the means of what we tested and its associated control are statistically significantly different with a confidence better than 99.5 %.

III.5. Discussion

The results presented in this chapter showed that infrared exposure caused an intracellular Ca^{2+} response without the need of extracellular Ca^{2+} entry in both HT22 mouse hippocampal neurons and U87 human glioblastoma cells. The pharmacological experiments led in this chapter made us conclude on the activation of the PLC / IP_3 pathway by the infrared exposure. This activation resulted in the release of Ca^{2+} ions from the endoplasmic reticulum to the cytosol. Those conclusions are in agreement with the PIP_2 depletion observed by Beier and colleagues [80]. However, in Beier's work, membrane permeabilization was observed. We did not find any plasma membrane permeabilization, which is furthermore not necessary given that the intracellular Ca^{2+} ions concentration increase occurred even without extracellular Ca^{2+} ions. Since intracellular Ca^{2+} responses happen without the need of extracellular Ca^{2+} entry, TRPV channels activation do not appear necessary to the Ca^{2+} responses observed. Under

physiological conditions, extracellular Ca^{2+} entry would also happen and the thermal activation of ion channels like TRPV may amplify the infrared effect and increase the probability of triggering action potentials. By the way, this may explain the fact that, for HT22 mouse hippocampal neurons, the time necessary for the intracellular Ca^{2+} ions concentration to go back to the baseline level is longer in physiological conditions compared to extracellular medium without Ca^{2+} ions.

With the consideration of all the results, we propose here that infrared exposure leads to the thermal activation of phosphoinositide signaling. It would be similar to heat shock PLC activation reported by Calderwood *et al*. [85]. They showed that increases in temperature activated the Gq class of G-proteins coupled to the PLC. This resulted in the activation of the PLC and the hydrolysis of PIP_2 into IP_3 and DAG. However, our results are not sufficient to know if infrared radiation induces directly the activity of PLC as in pure enzyme assays [86] or if the activation of Gq protein is necessary as showed by Calderwood's work.

Such a mechanism would explain the relations obtained in the dosimetry experiments presented earlier in this chapter. Dufour and coworkers [87] showed that the initial rate of Ca^{2+} release from the endoplasmic reticulum had a sigmoidal relationship to the IP_3 concentration. In the experiments made at constant exposure duration, with increasing energy density delivered by increasing the infrared power (Figure III-8 and Figure III-9), a sigmoidal relation was found between the intracellular Ca^{2+} ion concentration increase and the energy density delivered. With the assumption that the cytosolic concentration of IP_3 is increased with the heat shock strength, and thus with the infrared power applied, the sigmoidal relation found would be in agreement and explained by the sigmoidal relation of Dufour's work.

The activity of TRPV channels triggered as a response to infrared neural stimulation [43] is also expected after PLC activation. PIP_2 has been shown to bind to TRPV1 and TRPV4, and to modulate their activity [88]–[90]. Consequently, the depletion of PIP_2 by the PLC activity triggered by the infrared exposure could have an effect on TRPV channels activity. In addition to this effect, PLC activation results in the generation of DAG. This generation could have an effect on ion channels gating through the activation of protein kinase C by DAG resulting in the release of arachidonic acid stimulating TRPV4 activity [91]–[93].

Xu and Loew in 2003 [94] showed that the use of Gq protein agonists leading PLC activation in neuroblastoma cells induced an increase in intramembrane potential. The intramembrane potential has the contributions of the transmembrane potential, the difference between internal and external surface potential and the internal and external dipole potential. The increase of the internal dipole potential following PIP_2 hydrolysis was identified as the major contribution of this increase in intramembrane potential. The changes in the intramembrane potential were

found to be significant (up to 83 mV), and to be blocked by PLC inhibitors. With such changes induced by PIP_2 hydrolysis, if infrared activates the PLC, shifts in the membrane capacitance as found by Shapiro *et al*. [48] might be expected after infrared exposure.

The thermal activation of PLC was found here in HT22 mouse hippocampal neurons as well as in U87 human glioblastoma cells. PLC activation by infrared radiation may be a general mechanism occurring in both excitable and non-excitable cell types. However, an investigation about the effect of such infrared exposures on long-term cell viability is necessary before to think about therapeutic applications.

All the results of this chapter were published in Journal of Biophotonics in 2017 [95].

Chapter IV. Infrared neural stimulation in mice cortex *in vivo* with GCaMP6s two-photon imaging

The infrared neural stimulation (INS) has proved its efficiency in many studies *in vivo* in the auditory system [22], the facial nerve [28], the cavernous nerve [29], where infrared exposure triggered electrical activity of the targeted neurons. While INS has been widely used to stimulate the peripheral nervous system, its use in the central nervous system is less developed. Stimulating the central nervous system, and especially the brain, is particularly interesting since it is the location of the origins of numerous neurodegenerative diseases like Alzheimer's or Parkinson's. But it is also a great challenge due to the difficulty to reach it spatially.

The first application of INS in the central nervous system was performed by Cayce and coworkers in the rat somatosensory cortex [34]. To probe the effect of INS, intrinsic optical signal were measured. In this way, the ability of INS to stimulate the somatosensory cortex was proved by comparing responses induced by INS and natural tactile stimulation. In the same way, Cayce and coworkers, again, applied successfully INS to stimulate the primary visual cortex of macaque monkeys [35].

In this chapter, the ability of infrared to trigger neural response in mice brain *in vivo* simultaneously probed with two-photon calcium imaging is demonstrated. The exposure of brain tissue to infrared radiation triggered a calcium wave in the imaged area.

IV.1. Two-photon microscopy

To image live cells *in vivo* deep within tissue, two-photon microscopy is the current method of choice. Like other fluorescence microscopy techniques, two-photon microscopy uses a laser to excite the dye. However, while classical fluorescence microscopy techniques provides single photon imaging, two-photon microscopy is based on the simultaneously absorption of two lower energy photons, see Figure IV-1.

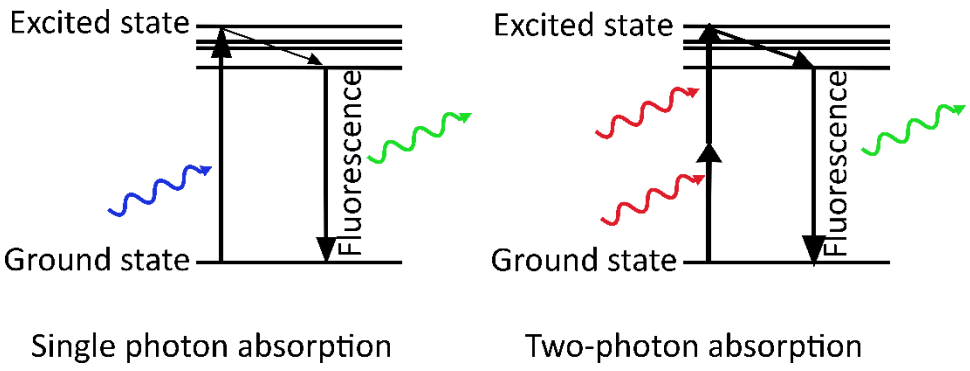

Figure IV-1 Principle of one- and two-photon absorption.

The use of longer wavelengths in two-photon microscopy presents the advantage to be less damaging than shorter wavelength used in classical fluorescence microscopy. In addition the longer wavelengths penetrate more deeply into the biological tissues.

To reach two-photon absorption, two-photons have to be in the same place, at the same time. Thus two conditions have to be fulfilled: the photon density has to be very high in a temporal point of view as well as in a spatial point of view, with obviously the good wavelength. To reach high temporal photon density, the use of pulsed laser excitation is necessary, typically femtosecond or picosecond laser sources. On the other hand, the high spatial photon density is reached by using high numerical aperture microscope objective to have the smallest focal point. Thus the two-photon absorption occurs in the focal plane. Consequently, no out of focus fluorescence light is collected, and the photodamaged area is smaller than with single photon fluorescence, as shown in Figure IV-2. Furthermore, compared to confocal microscopy, there is no need of pinhole to make spatial filtering.

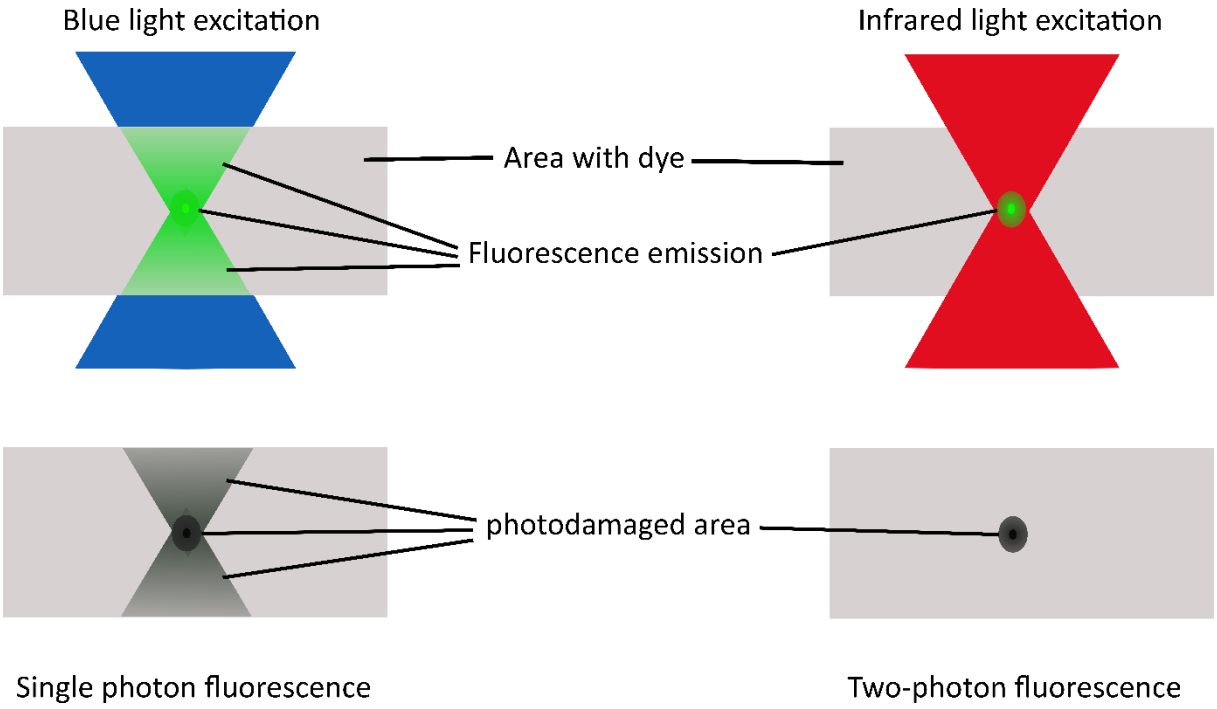

Figure IV-2 Photodamage induced by one- and two-photon fluorescence.

IV.2. Material and methods

IV.2.1. GCaMP6s mice

The measurement of the changes of intracellular calcium ion concentration is a way to assess neural activity [62]. To load calcium dye *in vivo* is harder than *in vitro* since it may require to maintain the targeted tissue under pressure [96].Due to the lack of material in our lab, other solutions were explored.

GCaMP is a genetically encoded calcium indicator (GECI) initially developed by Nakai *et al*.[97]. GCaMP is created by the fusion of a circularly permutated green fluorescent protein (cpEGFP), the M13 peptide and the Calmodulin, a protein that binds to calcium ions. As for other calcium indicators, the fluorescence of GCaMP increases with the binding of Ca^{2+} ions. The GCaMP indicator has been optimized since its creation to probe neural activity [98] allowing with superior sensitivity and brightness. With its Kd of 144 nM [99], GCaMP6s is able to probe rapid changes in intracellular Ca^{2+} ion concentration. Thus, C57BL/6J-Tg(Thy1-GCaMP6s)GP4.3Dkim/J mice (Jackson laboratory [100]) were used in this study for their stable expression levels of the GCaMP6s green fluorescent calcium indicator in excitatory neurons in the cortex (motor cortex, somatosensory cortex, and visual cortex of neocortex layers 2/3 and 5), that are sufficient for *in vivo* imaging.

IV.2.2. Mice preparation

The use of animals has received the approval of the local Ethical and Animal Care Committee (registration number 15-2015-15, MoNaPulse) under the responsibility of SM Bardet and RP O'Connor. All animal cares and experimental procedures were conducted in conformity with the French legislation n° 2013–118 1st February 2013 NOR: AGRG1231951D in accordance with European Community guidelines (directive 2010/63/UE for the Care and Use of Laboratory Animals).

Transgenic C57BL/6J-Tg(Thy1-GCaMP6s)GP4.3Dkim/J mice were bred under specific pathogen-free conditions in the core facility of the University of Limoges (EOPS, Marcland) under a 12 light/12 dark cycle. They are housed in individually ventilated cages within temperature and humidity ranges appropriate for murine species (~18-23°C with 40-60% humidity), to which they can adapt with minimal stress and physiologic alteration. They are fed *ad libitum* with a diet (fa content ranges from 4% to 11%) and water is accessible at all times. Bedding and nesting females are isolated from the male after reproduction in a separate cage containing cotton cylinders.

Mouse genomic DNA was isolated from tail on pups (maximum 3 weeks postnatal aged). The biopsies are transferred in an 1.5 ml tube for an overnight digestion at 56°C in lysis buffer containing 100 mM Tris-HCl (pH 8.5), 5 mM EDTA, 200 mM NaCl, 0.2% SDS and 400 µg/ml proteinase K (P6556, Sigma-Aldrich), followed by 30 s of vortex and 5 min centrifugation at 18 000g. The supernatant is transferred to a clean 1.5 ml tube and an equivalent volume of cold absolute ethanol is added before a 5 min centrifugation at 18 000g. The pellet is washed with 70% ethanol, centrifuged and finally washed with ultrapure water to be kept at 4°C after concentration estimation with a spectrophotometer (NanoDrop, Thermo Fisher Scientific).

Allelic discrimination is achieved by Polymerase Chain Reaction (PCR) with the Taq Core Kit (11EPTQK101, MP Biomedicals) using two pairs of primers : Fw18911 CATCAGTGCAGCAGAGCTTC and Rev18912 CAGCGTATCCACATAGCGTA for detecting the transgene targeting the calcium channel, voltage-dependent sequence), FwoICT21157 CTCCCAACCCCAGAGGTAGT and RevoICT21225 AGACCCCAGATCCAGAAAGG for the internal control targeting chromosome 6.

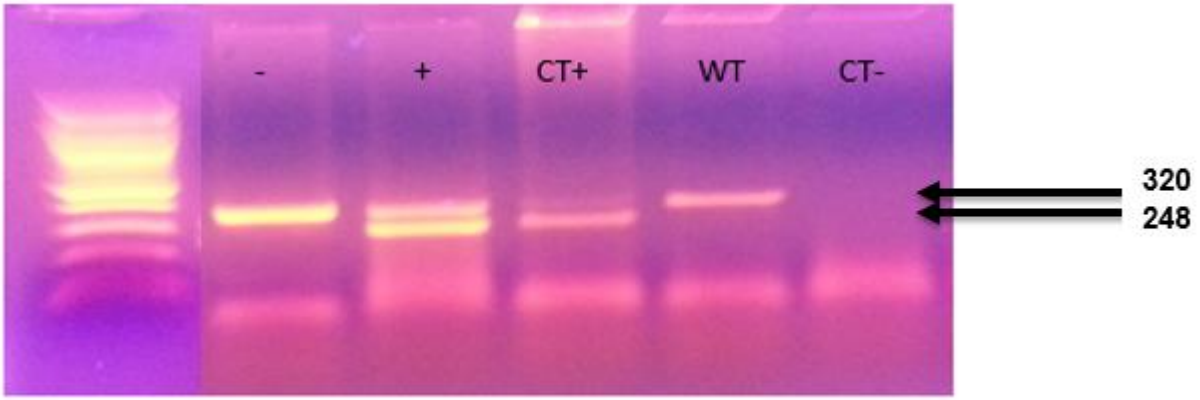

Figure IV-3 Electrophoretic migration of PCR products on agarose gel for mouse genotyping (- : non transgenic pup, + : transgenic pup, CT+ : transgenic male provided by the furnisher, WT : wilt-type animal, CT- : PCR on mix with no genomic DNA). Transgene = 248 bp (lower band), Internal positive control = 320 bp (upper band).

For cranial window surgery, mice were induced using 2.5% isoflurane and anesthetized with intraperitoneal injection of 65 mg/kg – 13 mg/kg Ketamine/Xylazine. Temperature body constant was regulated all along the experiment with a rectal probe controlling a heating pad. Head was fixed on a stereotaxic frame through ear bars to prevent from respiratory and autonomous movements.

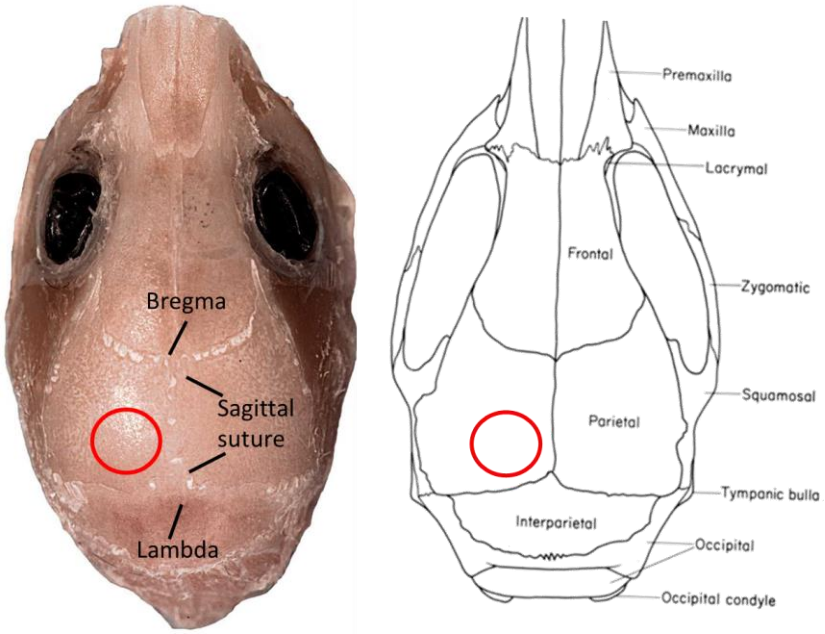

Figure IV-4 Location of the craniotomy in the parietal bone defines a 2.5 mm diameter circular zone.

A circular craniotomy (2.5 mm diameter) was made with a dental drill, with a small bit burr size (1.75mm) avoiding overheating by adding saline solution, to reveal the meninges and brain cortex. If bleeding occurs, it was controlled by applying pressure carefully with cotton. A thin layer of cyanoacrylate glue mixed with dental cement (Unifast Trad powder, GACD, France) was applied over the entire skull and bordering skin. A red fluorescent dye, SR101 or Sulforhodamine 101 (S7635 Sigma-Aldrich, λ_{em} 605 nm) in saline solution (100 µM) was deposited on the brain surface for a counterstaining of astrocytes to be able to analyze data from GCamp6s neurons separately. A 3 mm size glass coverslip (#1 thickness, Harvard Apparatus) is placed by pressure over surgical zone and covered again with cyanoacrylate + dental cement. A black square of 1 mm length was drawn on the glass surface to help in the further localization of the optic fiber and the microscopic objective placement.

The anesthetized animal was then placed under a BX61WI Olympus multiphoton microscope on a warm blanket (37°C) and physiologic constants are followed (regular breathing, body temperature).

IV.2.3. Experimental setup

Figure IV-5 presents the experimental setup used to perform brain calcium imaging in anesthetized mouse stimulated by infrared exposure at 1470 nm.

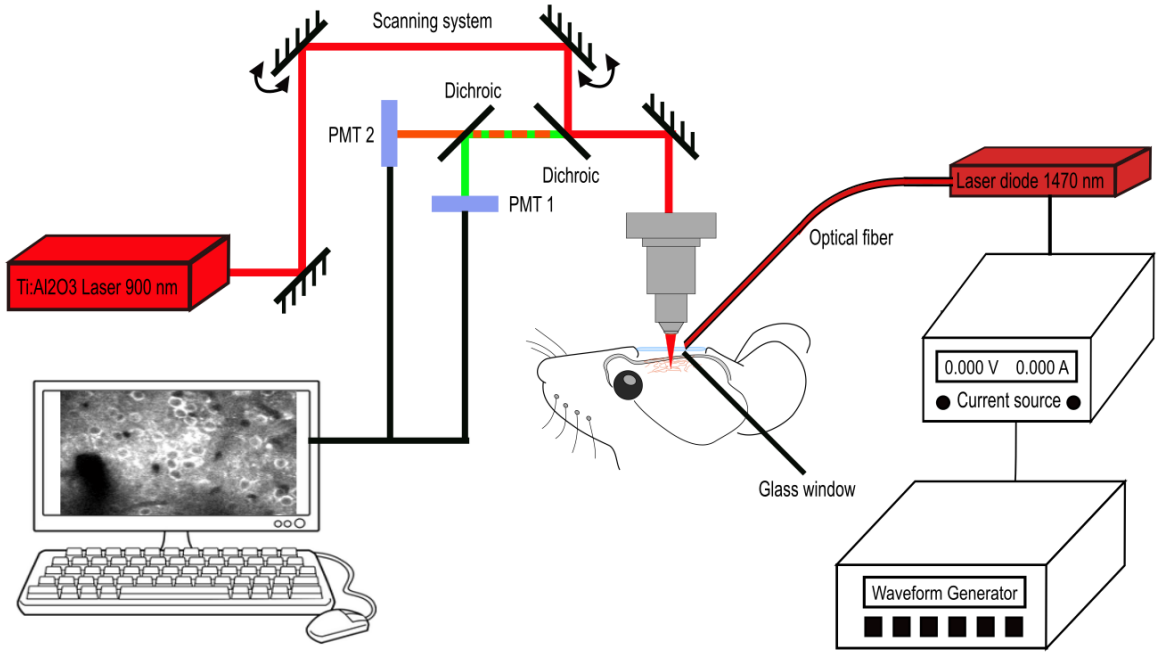

Figure IV-5 Experimental setup.

IV.2.3.1. Two-photon imaging

To perform two-photon imaging, the infrared laser source used was a tunable titanium-doped sapphire oscillator (Chameleon, Coherent, INC, 680-1080 nm, 10 nm, 140 fs, 80 MHz). The central wavelength was fixed at 900 nm and coupled to the BX61WI Olympus microscope. The microscope objective (XLPLN25XWMP2, Olympus) used was a water immersion objective with a magnification of 25X, a 2 mm working distance and a numerical aperture of 1.05. The average power was adjusted at 30 mW at the output of the objective with the use of a density. Excitation light was separated from the emitted fluorescence with a dichroic mirror (λ_c=650 nm). The fluorescence lights of GCaMP6s and SR101 were separated thanks to another dichroic mirror (λ_c=570 nm). They were then collected and recorded thanks to photomultipliers (PMT1 voltage 390 V and PMT2 voltage 424 V) with fluorophore specific emission filters (GFP 495–540 for GCaMP6s, BA 575–630 for SR101) and registered with the software Fluoview FV10-ASW (Olympus).

IV.2.3.2. Infrared stimulation

The infrared source used to stimulate the neurons was a multimode laser diode (LU1470T015, Lumics), emitting in continuous wave mode at 1470 nm. The laser diode presents a fibered output with a 105 µm core diameter and a 0.15 numerical aperture. A cooling block (LU_CB_T_0, Lumics) was used to stabilize the temperature and an adapted power supply (LU_DR_AD, Lumics) controlled the exposure duration and the power of the emitted infrared radiation. The power supply was externally controlled with a function/arbitrary waveform generator (33120A, Agilent Technologies). The tip of the fiber was placed thanks to micromanipulators on the top of the glass window on the mouse head. Figure IV-6 shows the part of the setup surrounding the mouse, with the microscope objective and the optical fiber delivering the infrared exposure to stimulate neurons in the brain.

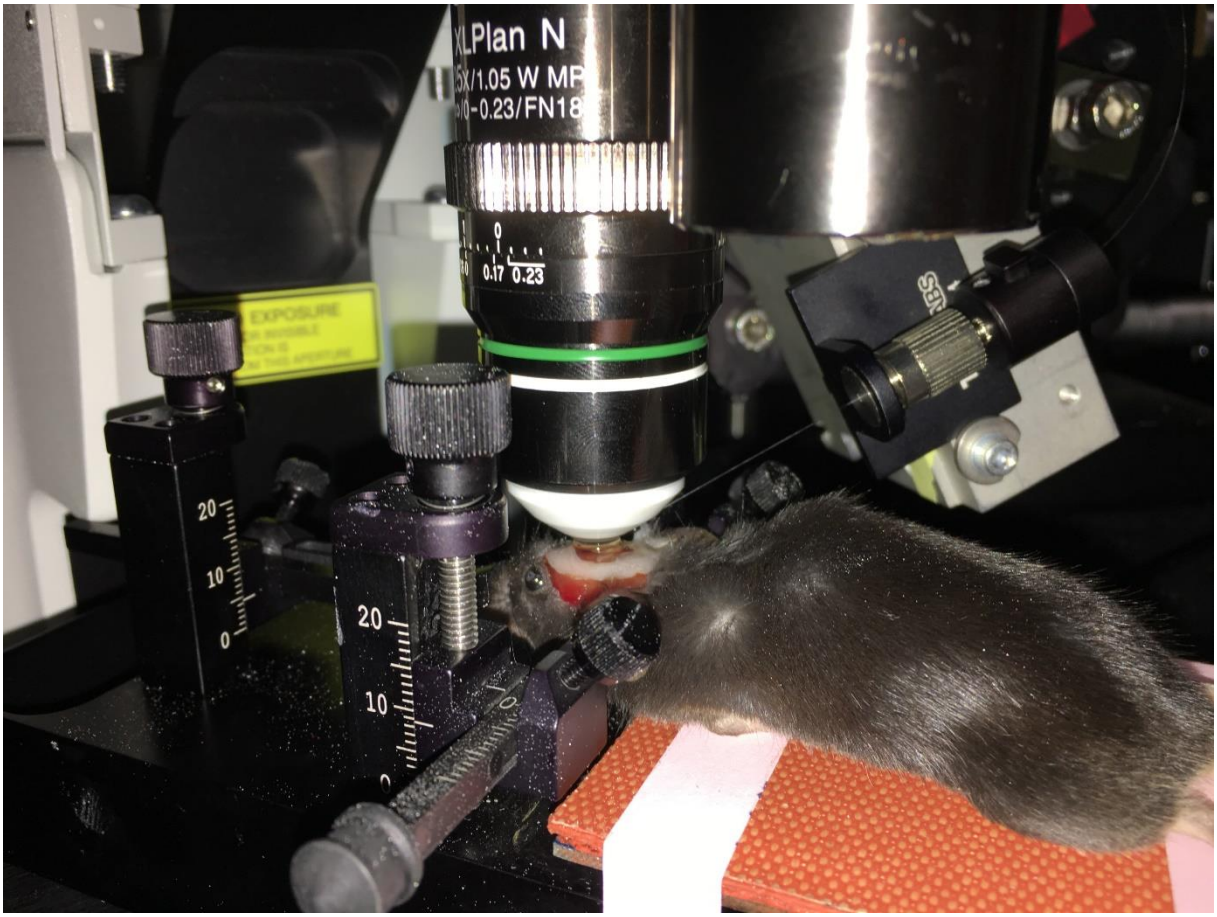

Figure IV-6 Image of a part of the setup surrounding the mouse. It includes the 25X microscope objective, the micromanipulator allowing the positioning of the optical fiber and the mouse lying on a heating blanket.

IV.2.3.3. Image analysis

The selection of the region of interest, defined as a single cell and the extraction of the fluorescence over time were made with Matlab. Relative changes in GCaMP6s fluorescence ($\Delta F/F_0$) was then computed. F_0 denotes the fluorescence baseline for a neuron at rest and $\Delta F=F-F_0$ denotes the change of fluorescence at each time point, reflecting the change of intracellular Ca^{2+} concentration changes.

IV.3. Results

First of all, to see the ability of the system to report neural activity by calcium imaging, fluorescence measurement was done to probe the spontaneous activity. Images were acquired with 12 bits pixels, with a sampling speed of 2 µs per pixel over a frame of 256*256 pixels, making a sampling speed of about 131 ms per frame. Spontaneous activity was successfully probed as shown in Figure IV-7.

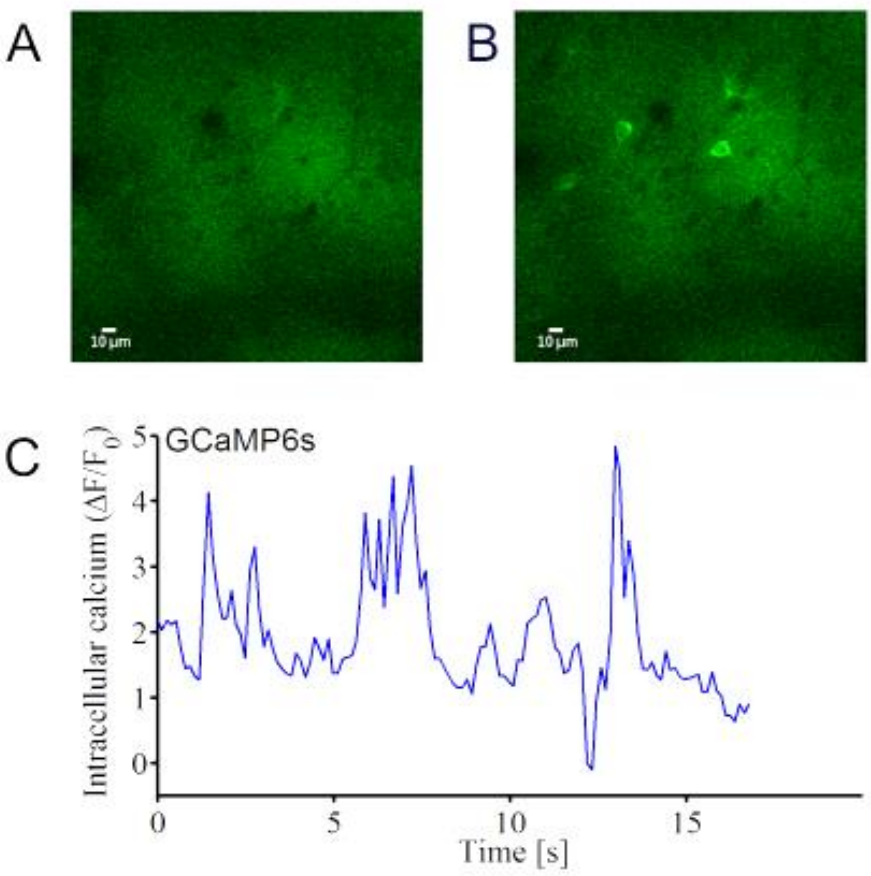

Figure IV-7 A. Image at rest. B. Image with firing neurons. C. Evolution of the intracellular calcium ion concentration over time during spontaneous activity.

To investigate on the ability of the 1470 nm infrared radiation to induce calcium signaling in the mouse brain, the infrared exposure was set to have a duration of 500 ms with an average power of 130 mW. Lower average powers have been tested without any probing results. Due to the very low fluorescence signal of GCaMP6s at rest and the very low spontaneous activity, the depth of the imaging was adjusted thanks to the SR101 fluorescence, indicating the presence of glial cells, see Figure IV-8, and consequently of neurons since neurons and glial cells are located in the same area. In all the exposed results, the imaged layer was between 200 and 300 µm deep from the surface.

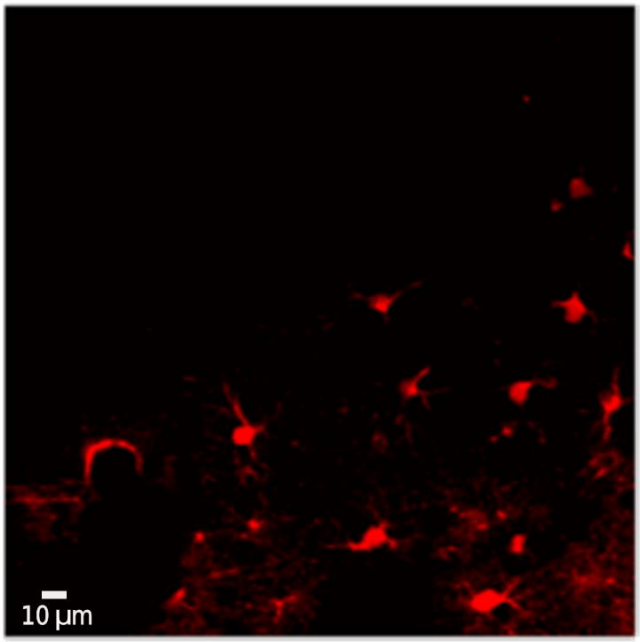

Figure IV-8 Image of glial cells labelled with SR101.

Figure IV-9 shows a series of images taken over time presenting the changes in GCaMP6s fluorescence in neurons targeted by the infrared exposure. Images were acquired with the same parameters (sampling speed of 2 µs per pixel over a frame of 256*256 pixels, making a sampling speed of about 131 ms per frame). The infrared exposure was applied about 30 s after the beginning of the recording.

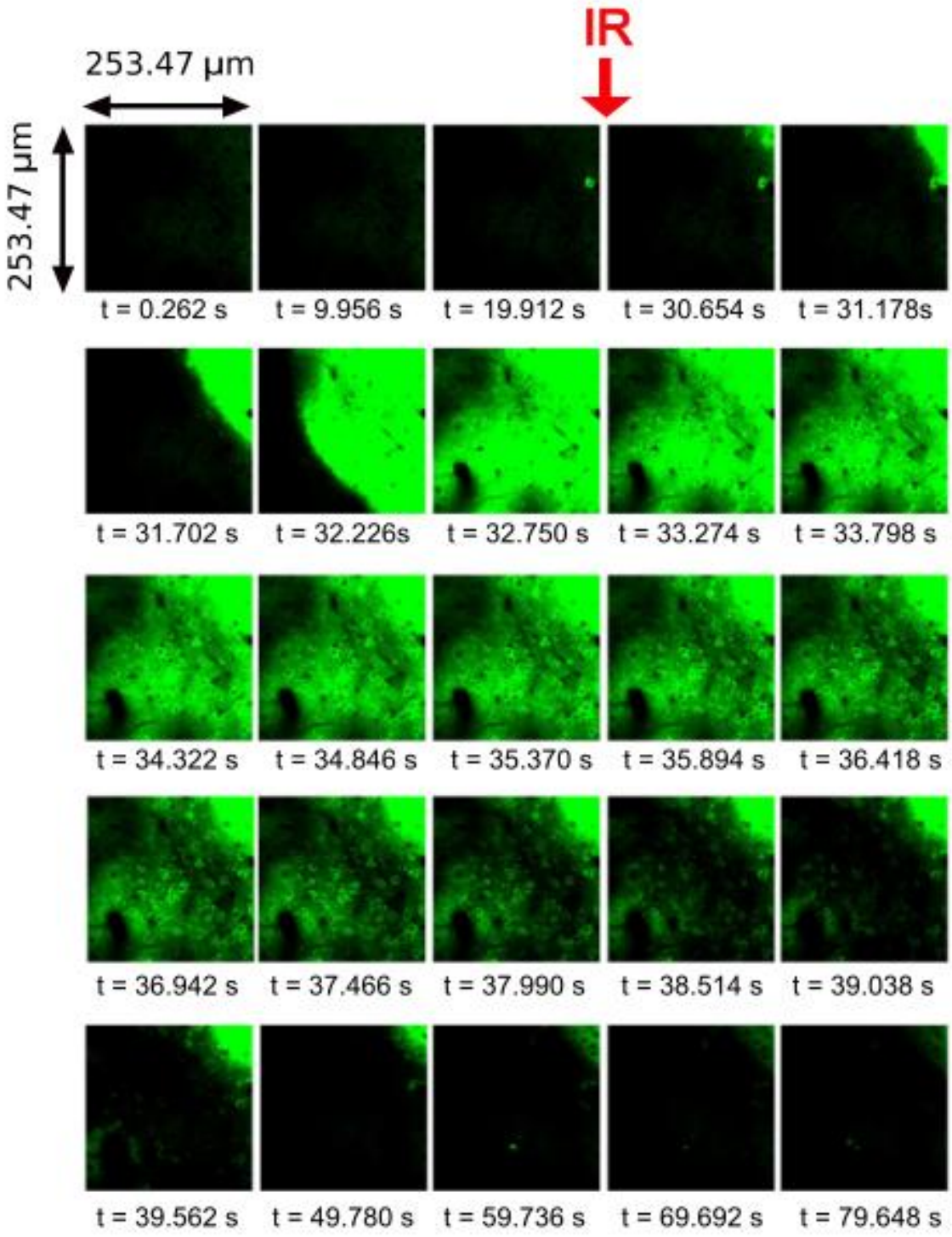

Figure IV-9 Intracellular calcium concentration changes induced by the exposure to 1470 nm radiation.

The infrared exposure clearly triggered a calcium wave lasting approximately 10 s, originating from the top right of the frame. This may be explained by the lack of precision in the optical fiber position. Indeed, the need in these experiments to place the fiber above the glass window was a challenge: the immersion water between the window and the objective preventing a good visibility to place the fiber, and the angle of the fiber necessary due to the low distance between the microscope objective and the glass window (less than 2 mm), made difficult the

optical fiber positioning. The precision was not enough to be sure to reach the area probed by two-photon imaging with the infrared radiation exiting the optical fiber. Thus, in the presented case, it is conceivable to think that the area directly exposed to the infrared radiation was higher and more to the right with regard to the frames recorded. The calcium wave could be the consequence of the activation of the neurons exposed to the infrared, and of the subsequent synaptic activity. Nevertheless, it remains the proof that infrared stimulation in the brain trigger calcium signaling in the neurons exposed. Figure IV-10 shows three different GCaMP6s fluorescence recordings in three different neurons located in the field of view.

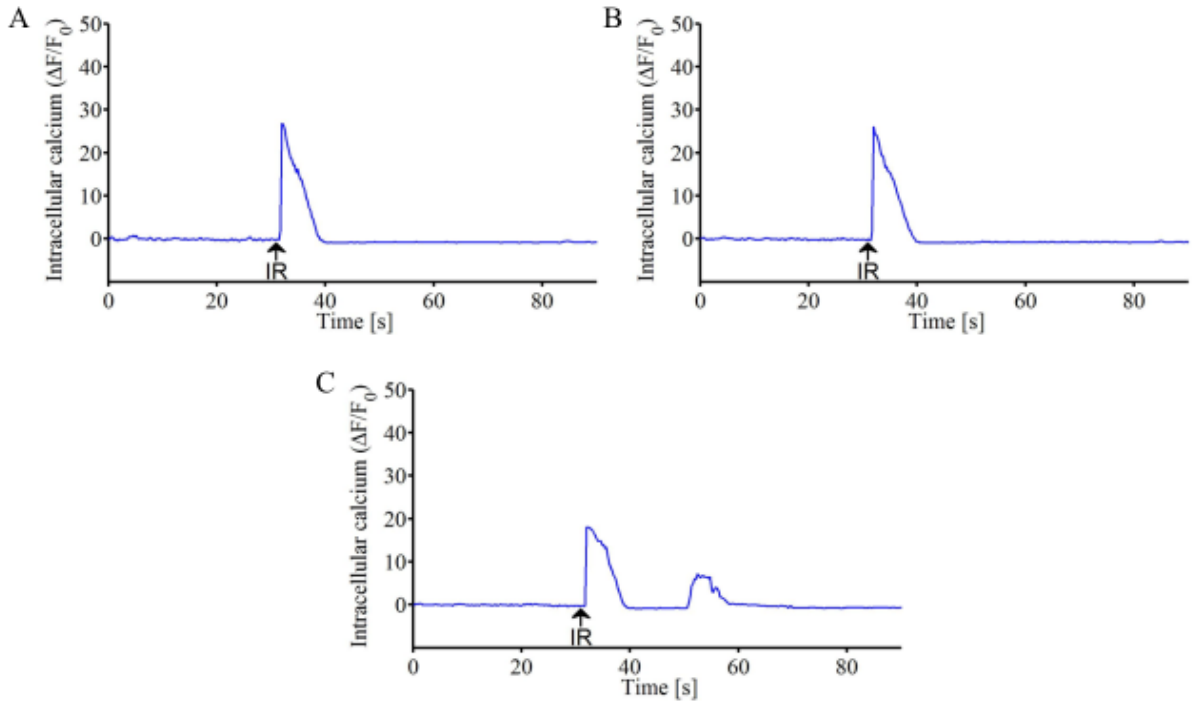

Figure IV-10 Intracellular calcium ion concentration increases in neurons induced by the exposure to 1470 nm infrared radiation.

After the calcium signal, and for each cell considered in Figure IV-10, the fluorescence of GCaMP6s went back to the baseline, meaning that the intracellular calcium ion concentration returns to rest after about 10 s, which is reassuring on the neurons safety.

Then, another area was targeted in the brain, and the optical fiber position was adjusted. Images were acquired with the same parameters (sampling speed of 2 µs per pixel over a frame of 256*256 pixels, resulting in a sampling speed of about 131 ms per frame). The infrared exposure was applied about 5 s after the beginning of the recording. Figure IV-11 shows a series of images taken over time presenting the changes in GCaMP6s fluorescence in neurons targeted by the infrared exposure.

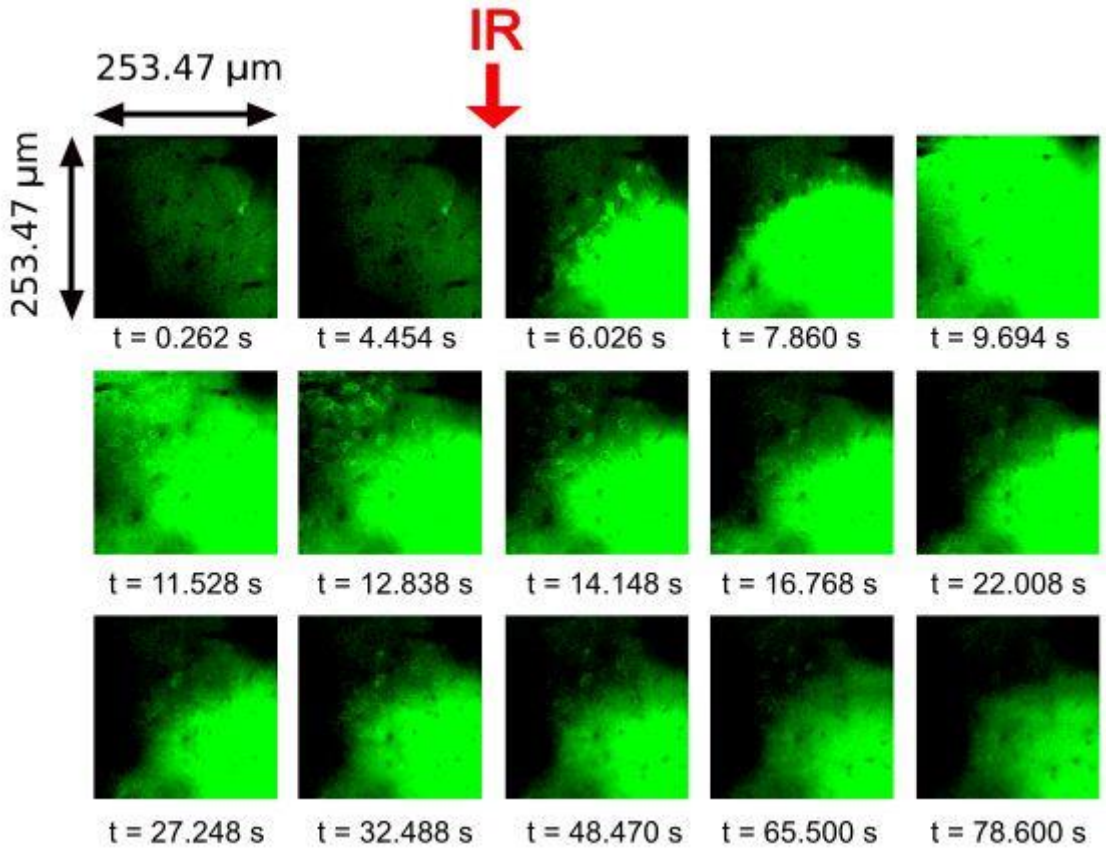

Figure IV-11 Intracellular calcium concentration changes probed by GCaMP6s fluorescence, induced by the exposure to 1470 nm radiation, probed in another area.

Here again, the infrared exposure clearly triggered a calcium wave originating from the right of the frame this time. Two different areas and time courses may be distinguished in Figure IV-11. The first one is almost a circle pretty well delimited on the third frame. In this area, the intracellular calcium ion concentration increases almost immediately after the infrared exposure. In this area, the intracellular calcium ion concentration remains also high for a long time, and decreases in a slow manner. As a hypothesis, this area could represent the exact site where the infrared is delivered. Even if only a bit more of a quarter of this circle appears, it is possible to estimate that its radius would be approximately about 125 µm.

Then, intracellular calcium ion concentration increases in the surrounding area, which could be due to the synaptic transmission. Here, the time course is faster, only a few seconds are needed for the intracellular calcium ion concentration to return at rest. To better see those two different time courses, 4 different region of interest were chosen and the data were processed and presented in Figure IV-12. Here the fluorescence intensity is presented in raw data, since the baseline fluorescence was 0, making the ΔF/F0 being always infinite.

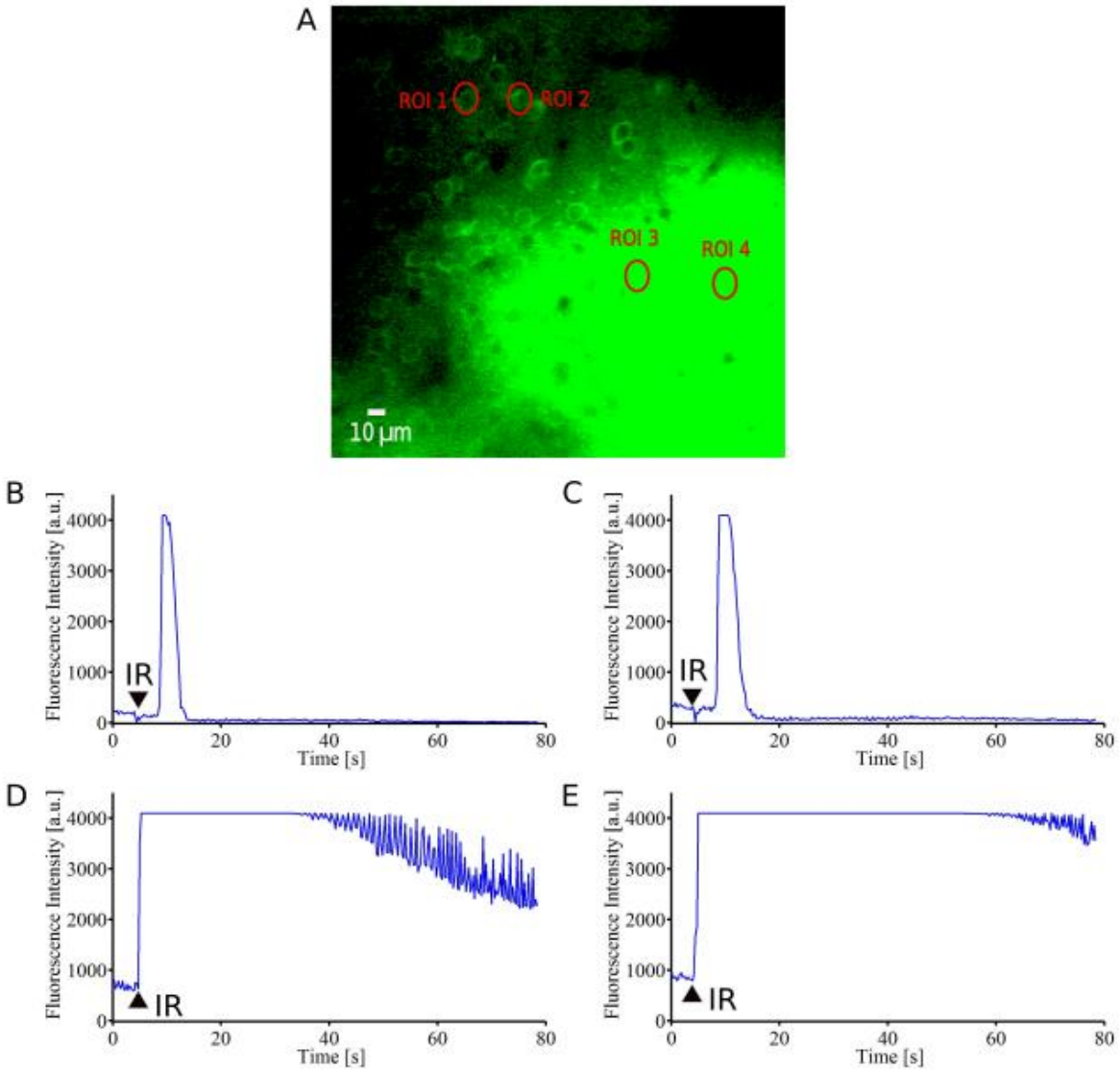

Figure IV-12 Evolution of the intracellular calcium ion concentration in neurons induced by the exposure to 1470 nm infrared radiation. A. Image of the area recorded with the 4 regions of interest considered (t=14.148s). B to E. Evolution of the intracellular calcium ion concentration in ROI 1 to ROI 4.

As seen in the image series in Figure IV-11, for the neurons in the neighboring area of the area where the infrared was delivered, the calcium transient is fast, lasting for 5-10 s. For the area expected to be directly exposed to infrared radiation, the intracellular calcium ion concentration increase was longer. The PMT was saturated for a few tens of seconds before observing a GCaMP6s fluorescence decrease in the sensitivity range of the detector. Unfortunately the recording duration was not long enough to see the intracellular calcium ion concentration going back to the baseline, but the trend seems to suggest that the baseline would be reached back after further time.

IV.4. Conclusion and discussion

The results presented in this chapter showed the ability to stimulate endogenous neurons in the brain of a living mouse with an exposure to 1470 nm radiation, and to record in the same time the intracellular calcium ions concentration changes probed by the fluorescence of GCaMP6s.The results obtained suggest that the infrared-induced calcium signaling happens immediately after the infrared exposure in the area exposed to the infrared. In this area the intracellular calcium ions concentration increases considerably and it requires at least a few tens of second to potentially reach back the resting concentration level. In the surrounding area, the increase of intracellular calcium ion concentration is triggered slightly later, smaller and shorter since it has a duration of a few seconds compared to the exposed area. The observed calcium wave originating from the exposed area suggests that the calcium signaling in the surrounding area could be the consequence of synaptic activity. To investigate on that point, a pharmacological study could be considered using for example gabapentin, an agonist of N-type and P/Q type calcium channels, which reduces excitatory amino acid neurotransmission in the brain.

Here, it is hard to certify whether the energy density delivered to the tissue was above the damage threshold or not. A more complete study, with the assurance of a correct position of the fiber, with the application of different infrared powers exposed and with more extensive histological analysis of the tissue would be required to know that. The same study could also allow to estimate the stimulation threshold. Unfortunately, the lack of time and of transgenic mice prevented to have further and more complete results.

Nevertheless, the principle to assess the infrared-induced neural activity in the brain by the use of genetically encoded fluorescence indicator like GCaMP6s is here proved. The critical point to improve in the experimental procedure presented is the positioning of the optical fiber delivering the 1470 nm infrared exposure. With the procedure used, the fiber had to be located just above the glass window. Here the positioning was difficult due to the short free space between the microscope objective and the mouse head, the needed fiber angle to not touch the microscope objective, the immersion water in the critical area where the fiber tip had to be, and the lack of bright field system on the microscope used.

One of the way to improve that point would be to upgrade the imaging system with a bright field option, to clearly see the tip of the fiber and the glass window on the mouse head. Then, knowing the angle of the fiber and the penetration depth of the targeted area, it would be possible to calculate the distance needed between the fiber tip and the microscope objective center axis to be sure to expose the targeted area imaged with the microscope. Then the use of micromanipulator would get through the remaining technical points.

Another idea would be to find a way to insert the fiber directly in the brain tissue, to be close enough to the imaged area. This would also have other advantages. Indeed, the distance between the fiber tip and the neurons would be smaller than in the present case. Thus, probably less infrared energy density would be required to successfully stimulate the neurons. In the present case, the energy of the infrared delivered to the targeted neurons is the energy still present after the absorption of more than 200 µm. With less energy density and consequently less energy delivered in all the depth exposed to the infrared, the probability to damage the surrounding tissue would be smaller. Also, with a smaller distance between the fiber tip and the targeted neurons, the area exposed would be smaller due to the beam divergence. This could result in an improved spatial selectivity of the infrared stimulation efficiency.

With a more developed setup, a study on the potential differences in the stimulated brain regions could be also considered. According to the brain region, the stimulation and damage thresholds may be different. That could also be interesting to compare the effects triggered by the infrared stimulation and by the electrical stimulation since they do not involve the same mechanism of action. In a first time motor or autonomic effects like heart and respiration rates could be considered because they are easy to detect.

Conclusion

The efficiency of the use of infrared laser light to achieve neural stimulation has been demonstrated in many studies, on a wide variety of targets. However, its underlying mechanism is not fully elucidated and remains a field of interest. From the beginning, photochemical interaction mechanism was excluded due to the low energy of infrared photon. In the same way, photomechanical interactions were not believed since the infrared pulses durations are too long to allow stress confinement. Different works attempted to identify this mechanism leading to the consideration of a few hypotheses based on a photothermal interaction, occurring due to the conversion into heat of the infrared radiation absorption by water. The first proposition highlighted the absolute temperature as the key parameter, since passed above a certain threshold, it could activate heat sensitive ion channels like TRPV channels resulting in the generation of action potentials. Another hypothesis was based on an electrostatic mechanism where rather than the value of the temperature itself, the temperature gradient was believed to influence the plasma membrane capacitance. This would result in a change of the membrane potential which would be sufficient to initiate action potentials. The main purpose of this PhD was to clarify the underlying mechanism behind the infrared neural stimulation and to measure the temperature changes associated to the infrared exposure.

To measure the temperature at the cellular level, the fluorescent dye Rhodamine B was used. In a first time, to demonstrate the ability of RhB to measure the temperature in cells exposed to an exogenous heat source, the temperature changes in cells were measured with the exposure to infrared radiation at 805 nm and to nanosecond pulsed electric fields. With the optical setup used, the thermal precision was found to be 0.1 °C and the temporal resolution of a few milliseconds. Both of those resolution may be improved by both better quantum efficiency and readout speed.

The underlying mechanism of INS has then been investigated by assessing the neural activity induced by infrared exposure with calcium imaging using Fluo-4 fluorescent dye. Here, effects on both HT22 mouse hippocampal neurons and U87 human glioblastoma cells were considered. In both of the cell types, the infrared exposure triggered an increase in the intracellular calcium concentration. After a dosimetry study, pharmacological experiments were performed to find the origin of Ca^{2+} ions. The results obtained led to the conclusion that infrared exposure triggered the activation of the enzyme Phospholipase C in both types of cells. This activation resulted in the release of Ca^{2+} ions from the endoplasmic reticulum to the cytosol mediated by the IP_3 pathway. Those conclusions are in agreement with the PIP_2 depletion observed in Beier's work and consequently with the change in the membrane potential triggered by infrared exposure. No membrane permeabilization was however reported. TRPV

activation observed in several works in literature may also be expected after PLC activation. PIP_2 depletion induced by PLC activity may have an effect on TRPV channels since PIP_2 has been shown to bind to TRPV1 and TRPV4 and to modulate their activity. In addition, PLC activity results in the generation of dialglycerol, activating the protein kinase C, resulting in the release of arachidonic acid stimulating TRPV4 activity. However both membrane permeabilization and TRPV activation do not appear necessary since intracellular Ca^{2+} responses happen without the need of extracellular Ca^{2+} entry.

Temperature measurement were also done with the same infrared exposure parameters used in the pharmacological study. With the consideration of all the results, we propose that the infrared exposure induced the thermal activation of phosphoinositide signaling. However, further work should be done in order to know if the Gq protein coupled to PLC is involved or if there is a direct activation of PLC not mediated by the G-protein. The mechanism was found to be the same in HT22 mouse hippocampal neurons as well as in U87 human glioblastoma cells. Infrared-induced thermal activation seems consequently to be a general mechanism occurring in both electrically excitable and non-excitable cell types.

Finally, the ability to probe the intracellular calcium concentration during INS in the mice brain *in vivo* has been demonstrated, for the first time, with the use of GCaMP6s mice. During the few tries performed, the results suggested that the infrared-induced calcium response occurred immediately after the start of the infrared exposure in the area directly exposed to the light. Here, the intracellular calcium increase required at least a few tens of second before to reach back the rest concentration. In the surrounding area, a calcium wave was identified, propagating from the infrared exposed area. The beginning of the calcium wave was delayed of a few seconds after the infrared exposure. Here, the intracellular calcium increase lasted a few seconds before to reach back the rest concentration. As a hypothesis, the calcium wave originating from the infrared exposed area was identified as the consequence of synaptic transmission in the brain originating from the neurons directly stimulated by the infrared exposure.

Bibliography

[1] R. Liljemalm, “Infrared Laser Stimulation of Cerebral Cortex Cells-Aspects of Heating and Cellular Responses,” KTH Royal Institute of Technology, 2013.

[2] D. Purves *et al.*, *Neuroscience*. Sinauer Associates, Inc, Sunderland, Massachusetts, USA. ISBN 0-87893-725-0, 2004.

[3] M. H. Niemz, *Laser-tissue interactions: fundamentals and applications*. Springer Science & Business Media, 2013.

[4] G. M. Hale and M. R. Querry, “Optical constants of water in the 200-nm to 200-μm wavelength region,” *Appl. Opt.*, vol. 12, no. 3, pp. 555–563, 1973.

[5] L. Shi, L. A. Sordillo, A. Rodríguez-Contreras, and R. Alfano, “Transmission in near-infrared optical windows for deep brain imaging,” *J. Biophotonics*, vol. 9, no. 1–2, pp. 38–43, 2016.

[6] S. L. Jacques, “Laser-tissue interactions: photochemical, photothermal, and photomechanical,” *Surg. Clin. North Am.*, vol. 72, no. 3, pp. 531–558, 1992.

[7] P. Limousin *et al.*, “Electrical stimulation of the subthalamic nucleus in advanced Parkinson’s disease,” *N. Engl. J. Med.*, vol. 339, no. 16, pp. 1105–1111, 1998.

[8] A. L. Benabid *et al.*, “Chronic electrical stimulation of the ventralis intermedius nucleus of the thalamus as a treatment of movement disorders,” *J. Neurosurg.*, vol. 84, no. 2, pp. 203–214, 1996.

[9] E. S. Boyden, F. Zhang, E. Bamberg, G. Nagel, and K. Deisseroth, “Millisecond-timescale, genetically targeted optical control of neural activity,” *Nat Neurosci*, vol. 8, no. 9, pp. 1263–1268, Sep. 2005.

[10] P. S. Lagali *et al.*, “Light-activated channels targeted to ON bipolar cells restore visual function in retinal degeneration,” *Nat. Neurosci.*, vol. 11, no. 6, pp. 667–675, 2008.

[11] C. Schroll *et al.*, “Light-induced activation of distinct modulatory neurons triggers appetitive or aversive learning in Drosophila larvae,” *Curr. Biol.*, vol. 16, no. 17, pp. 1741–1747, 2006.

[12] D. Huber *et al.*, “Sparse optical microstimulation in barrel cortex drives learned behaviour in freely moving mice,” *Nature*, vol. 451, no. 7174, pp. 61–64, 2008.

[13] A. R. Adamantidis, F. Zhang, A. M. Aravanis, K. Deisseroth, and L. De Lecea, “Neural substrates of awakening probed with optogenetic control of hypocretin neurons,” *Nature*, vol. 450, no. 7168, pp. 420–424, 2007.

[14] X. Han *et al.*, “Millisecond-timescale optical control of neural dynamics in the nonhuman primate brain,” *Neuron*, vol. 62, no. 2, pp. 191–198, 2009.

[15] J. Wells, C. Kao, E. D. Jansen, P. Konrad, and A. Mahadevan-Jansen, “Application of infrared light for in vivo neural stimulation,” *J. Biomed. Opt.*, vol. 10, no. 6, pp. 64003–64012, 2005.

[16] A. D. Izzo, E. Suh, J. Pathria, J. Walsh Joseph T., D. S. Whitlon, and C.-P. Richter, “Selectivity of neural stimulation in the auditory system: a comparison of optic and electric stimuli,” *J. Biomed. Opt.*, vol. 12, no. 2, pp. 21007–21008, 2007.

[17] C.-P. Richter *et al.*, “Spread of cochlear excitation during stimulation with pulsed infrared radiation: inferior colliculus measurements.,” *J. Neural Eng.*, vol. 8, no. 5, p. 56006, Oct. 2011.

[18] A. I. Matic, J. Walsh Joseph T., and C.-P. Richter, “Spatial extent of cochlear infrared neural stimulation determined by tone-on-light masking,” *J. Biomed. Opt.*, vol. 16, no.

11, pp. 118002–1180028, 2011.

[19] A. D. Izzo, C. Richter, E. D. Jansen, and J. T. Walsh, “Laser stimulation of the auditory nerve,” *Lasers Surg. Med.*, vol. 38, no. 8, pp. 745–753, 2006.

[20] A. D. Izzo *et al.*, “Optical parameter variability in laser nerve stimulation: a study of pulse duration, repetition rate, and wavelength,” *IEEE Trans. Biomed. Eng.*, vol. 54, no. 6, pp. 1108–1114, 2007.

[21] V. Goyal, S. Rajguru, A. I. Matic, S. R. Stock, and C.-P. Richter, “Acute damage threshold for infrared neural stimulation of the cochlea: functional and histological evaluation.,” *Anat. Rec. (Hoboken).*, vol. 295, no. 11, pp. 1987–99, Nov. 2012.

[22] A. I. Matic *et al.*, “Behavioral and Electrophysiological Responses Evoked by Chronic Infrared Neural Stimulation of the Cochlea,” *PLoS One*, vol. 8, no. 3, p. e58189, Mar. 2013.

[23] D. M. Harris, S. M. Bierer, J. D. Wells, and J. O. Phillips, “Optical nerve stimulation for a vestibular prosthesis,” in *Proc. SPIE 7180, Photons and Neurons*, 2009, vol. 7180, p. 71800R–71800R–7.

[24] S. M. Rajguru *et al.*, “Infrared photostimulation of the crista ampullaris,” *J. Physiol.*, vol. 589, no. 6, pp. 1283–1294, 2011.

[25] R. Boyle and S. M. Highstein, “Resting discharge and response dynamics of horizontal semicircular canal afferents of the toadfish, Opsanus tau,” *J. Neurosci.*, vol. 10, no. 5, pp. 1557–1569, 1990.

[26] K. Zhao, X. Tan, H. Young, and C.-P. Richter, “Stimulation of Neurons with Infrared Radiation,” in *Biomedical Optics in Otorhinolaryngology*, Springer, 2016, pp. 253–284.

[27] P. J. Boutros, J. Ahn, G. Y. Fridman, C. Dai, D. Lasker, and C. C. Della Santina, “Vestibulo-ocular reflex eye movement responses to infra-red laser stimulation of the mammalian labyrinth,” *Assoc. Res. Otolaryngol.*, vol. 36, p. 255, 2013.

[28] I. U. Teudt, A. E. Nevel, A. D. Izzo, J. T. Walsh, and C. Richter, “Optical stimulation of the facial nerve: a new monitoring technique?,” *Laryngoscope*, vol. 117, no. 9, pp. 1641–1647, 2007.

[29] N. M. Fried, G. A. Lagoda, N. J. Scott, L. M. Su, and A. L. Burnett, “Laser stimulation of the cavernous nerves in the rat prostate, in vivo: Optimization of wavelength, pulse energy, and pulse repetition rate,” *2008 30th Annual International Conference of the IEEE Engineering in Medicine and Biology Society*. pp. 2777–2780, 2008.

[30] N. M. Fried, G. a Lagoda, N. J. Scott, L.-M. Su, and A. L. Burnett, “Noncontact stimulation of the cavernous nerves in the rat prostate using a tunable-wavelength thulium fiber laser.,” *J. Endourol.*, vol. 22, no. 3, pp. 409–13, 2008.

[31] S. Tozburun, C. D. Stahl, T. C. Hutchens, G. A. Lagoda, A. L. Burnett, and N. M. Fried, “Continuous-wave Infrared Subsurface Optical Stimulation of the Rat Prostate Cavernous Nerves Using a 1490-nm Diode Laser,” *Urology*, vol. 82, no. 4, pp. 969–973, Oct. 2013.

[32] S. Tozburun, G. A. Lagoda, A. L. Burnett, and N. M. Fried, “Subsurface near-infrared laser stimulation of the periprostatic cavernous nerves,” *J. Biophotonics*, vol. 5, no. 10, pp. 793–800, 2012.

[33] S. Tozburun, T. C. Hutchens, M. A. McClain, G. A. Lagoda, A. L. Burnett, and N. M. Fried, “Temperature-controlled optical stimulation of the rat prostate cavernous nerves,” *J. Biomed. Opt.*, vol. 18, no. 6, p. 67001, 2013.

[34] J. M. Cayce, R. M. Friedman, E. D. Jansen, A. Mahavaden-Jansen, and A. W. Roe, “Pulsed infrared light alters neural activity in rat somatosensory cortex in vivo,”

Neuroimage, vol. 57, no. 1, pp. 155–166, Jul. 2011.

[35] J. M. Cayce, R. M. Friedman, G. Chen, E. D. Jansen, A. Mahadevan-Jansen, and A. W. Roe, “Infrared neural stimulation of primary visual cortex in non-human primates,” *Neuroimage*, vol. 84, pp. 181–190, Jan. 2014.

[36] F. A. Wininger, J. L. Schei, and D. M. Rector, “Complete optical neurophysiology: toward optical stimulation and recording of neural tissue,” *Appl. Opt.*, vol. 48, no. 10, pp. D218–D224, 2009.

[37] B. Entwisle, S. McMullan, P. Bokiniec, S. Gross, R. Chung, and M. Withford, “In vitro neuronal depolarization and increased synaptic activity induced by infrared neural stimulation,” *Biomed. Opt. Express*, vol. 7, no. 9, pp. 3211–3219, 2016.

[38] N. I. Smith, Y. Kumamoto, S. Iwanaga, J. Ando, K. Fujita, and S. Kawata, “A femtosecond laser pacemaker for heart muscle cells,” *Opt. Express*, vol. 16, no. 12, pp. 8604–8616, 2008.

[39] M. W. Jenkins *et al.*, “Optical pacing of the embryonic heart,” *Nat Phot.*, vol. 4, no. 9, pp. 623–626, Sep. 2010.

[40] A. R. Duke, J. M. Cayce, J. D. Malphrus, P. Konrad, A. Mahadevan-Jansen, and E. D. Jansen, “Combined optical and electrical stimulation of neural tissue in vivo,” *J. Biomed. Opt.*, vol. 14, no. 6, pp. 60501–60503, 2009.

[41] A. R. Duke, H. Lu, M. W. Jenkins, H. J. Chiel, and E. D. Jansen, “Spatial and temporal variability in response to hybrid electro-optical stimulation.,” *J. Neural Eng.*, vol. 9, no. 3, p. 36003, 2012.

[42] J. Wells *et al.*, “Biophysical Mechanisms of Transient Optical Stimulation of Peripheral Nerve,” *Biophys. J.*, vol. 93, no. 7, pp. 2567–2580, Oct. 2007.

[43] A. Y. Rhee, G. Li, J. Wells, and J. P. Y. Kao, “Photostimulation of sensory neurons of the rat vagus nerve,” in *Proc. SPIE 6854, Optical Interactions with Tissue and Cells XIX*, 2008, vol. 6854, p. 68540E–68540E–5.

[44] E. Suh, A. Izzo Matic, M. Otting, J. Walsh Joseph T., and C.-P. Richter, “Optical stimulation in mice lacking the TRPV1 channel,” in *Proc. SPIE 7180, Photons and Neurons*, 2009, vol. 7180, p. 71800S–71800S–5.

[45] E. S. Albert *et al.*, “TRPV4 channels mediate the infrared laser-evoked response in sensory neurons,” *J. Neurophysiol.*, vol. 107, no. 12, p. 3227 LP-3234, Jun. 2012.

[46] J.-M. Bec *et al.*, “Characteristics of laser stimulation by near infrared pulses of retinal and vestibular primary neurons,” *Lasers Surg. Med.*, vol. 44, no. 9, pp. 736–745, 2012.

[47] E. J. Katz, I. K. Ilev, V. Krauthamer, D. H. Kim, and D. Weinreich, “Excitation of primary afferent neurons by near-infrared light in vitro,” *Neuroreport*, vol. 21, no. 9, 2010.

[48] M. G. Shapiro, K. Homma, S. Villarreal, C.-P. Richter, and F. Bezanilla, “Infrared light excites cells by changing their electrical capacitance,” *Nat. Commun.*, vol. 3, p. 736, 2012.

[49] E. J. Peterson and D. J. Tyler, “Activation using infrared light in a mammalian axon model,” *2012 Annual International Conference of the IEEE Engineering in Medicine and Biology Society*. pp. 1896–1899, 2012.

[50] G. M. Dittami, S. M. Rajguru, R. A. Lasher, R. W. Hitchcock, and R. D. Rabbitt, “Intracellular calcium transients evoked by pulsed infrared radiation in neonatal cardiomyocytes,” *J. Physiol.*, vol. 589, no. 6, pp. 1295–1306, 2011.

[51] O. Zohar *et al.*, “Thermal imaging of receptor-activated heat production in single cells,”

Biophys. J., vol. 74, no. 1, pp. 82–89, 1998.

[52] C. Gota, K. Okabe, T. Funatsu, Y. Harada, and S. Uchiyama, “Hydrophilic fluorescent nanogel thermometer for intracellular thermometry,” *J. Am. Chem. Soc.*, vol. 131, no. 8, pp. 2766–2767, 2009.

[53] L. Shang, F. Stockmar, N. Azadfar, and G. U. Nienhaus, “Intracellular thermometry by using fluorescent gold nanoclusters,” *Angew. Chemie Int. Ed.*, vol. 52, no. 42, pp. 11154–11157, 2013.

[54] K. Okabe, N. Inada, C. Gota, Y. Harada, T. Funatsu, and S. Uchiyama, “Intracellular temperature mapping with a fluorescent polymeric thermometer and fluorescence lifetime imaging microscopy,” *Nat. Commun.*, vol. 3, p. 705, 2012.

[55] C. Wang *et al.*, “Determining intracellular temperature at single-cell level by a novel thermocouple method,” *Cell Res.*, vol. 21, no. 10, p. 1517, 2011.

[56] K. M. McCabe, E. J. Lacherndo, I. Albino-Flores, E. Sheehan, and M. Hernandez, “LacI (Ts)-regulated expression as an in situ intracellular biomolecular thermometer,” *Appl. Environ. Microbiol.*, vol. 77, no. 9, pp. 2863–2868, 2011.

[57] J. S. Donner, S. A. Thompson, M. P. Kreuzer, G. Baffou, and R. Quidant, “Mapping intracellular temperature using green fluorescent protein,” *Nano Lett.*, vol. 12, no. 4, pp. 2107–2111, 2012.

[58] L. Yang, H.-S. Peng, H. Ding, F.-T. You, L.-L. Hou, and F. Teng, “Luminescent Ru (bpy) 3 2+-doped silica nanoparticles for imaging of intracellular temperature,” *Microchim. Acta*, vol. 181, no. 7–8, pp. 743–749, 2014.

[59] J.-M. Yang, H. Yang, and L. Lin, “Quantum dot nano thermometers reveal heterogeneous local thermogenesis in living cells,” *ACS Nano*, vol. 5, no. 6, pp. 5067–5071, 2011.

[60] L. M. Maestro *et al.*, “CdSe quantum dots for two-photon fluorescence thermal imaging,” *Nano Lett.*, vol. 10, no. 12, pp. 5109–5115, 2010.

[61] F. Vetrone *et al.*, “Temperature sensing using fluorescent nanothermometers,” *ACS Nano*, vol. 4, no. 6, pp. 3254–3258, 2010.

[62] B. L. Sabatini, T. G. Oertner, and K. Svoboda, “The life cycle of Ca 2+ ions in dendritic spines,” *Neuron*, vol. 33, no. 3, pp. 439–452, 2002.

[63] J. Ferguson and A. W. H. Mau, “Spontaneous and stimulated emission from dyes. Spectroscopy of the neutral molecules of acridine orange, proflavine, and rhodamine B,” *Aust. J. Chem.*, vol. 26, no. 8, pp. 1617–1624, 1973.

[64] R. F. Kubin and A. N. Fletcher, “Fluorescence quantum yields of some rhodamine dyes,” *J. Lumin.*, vol. 27, no. 4, pp. 455–462, 1982.

[65] J. J. Shah, M. Gaitan, and J. Geist, “Generalized temperature measurement equations for rhodamine B dye solution and its application to microfluidics,” *Anal. Chem.*, vol. 81, no. 19, pp. 8260–8263, 2009.

[66] U. Seger-Sauli, M. Panayiotou, S. Schnydrig, M. Jordan, and P. Renaud, “Temperature measurements in microfluidic systems: Heat dissipation of negative dielectrophoresis barriers,” *Electrophoresis*, vol. 26, no. 11, pp. 2239–2246, 2005.

[67] J. J. Shah *et al.*, “Microwave dielectric heating of fluids in an integrated microfluidic device,” *J. Micromechanics Microengineering*, vol. 17, no. 11, p. 2224, 2007.

[68] J. Sakakibara and R. J. Adrian, “Whole field measurement of temperature in water using two-color laser induced fluorescence,” *Exp. Fluids*, vol. 26, no. 1–2, pp. 7–15, 1999.

[69] D. Ross, M. Gaitan, and L. E. Locascio, “Temperature measurement in microfluidic systems using a temperature-dependent fluorescent dye,” *Anal. Chem.*, vol. 73, no. 17, pp. 4117–4123, 2001.

[70] P. Löw, B. Kim, N. Takama, and C. Bergaud, “High-Spatial-Resolution Surface-Temperature Mapping Using Fluorescent Thermometry,” *Small*, vol. 4, no. 7, pp. 908–914, 2008.

[71] L. Gui and C. L. Ren, “Temperature measurement in microfluidic chips using photobleaching of a fluorescent thin film,” *Appl. Phys. Lett.*, vol. 92, no. 2, p. 24102, 2008.

[72] Y. Y. Chen and A. W. Wood, “Application of a temperature-dependent fluorescent dye (Rhodamine B) to the measurement of radiofrequency radiation-induced temperature changes in biological samples,” *Bioelectromagnetics*, vol. 30, no. 7, pp. 583–590, 2009.

[73] S. Kohler, R. P. O’Connor, T. D. T. Vu, P. Leveque, and D. Arnaud-Cormos, “Experimental microdosimetry techniques for biological cells exposed to nanosecond pulsed electric fields using microfluorimetry,” *IEEE Trans. Microw. Theory Tech.*, vol. 61, no. 5, pp. 2015–2022, 2013.

[74] J. B. Davis and P. Maher, “Protein kinase C activation inhibits glutamate-induced cytotoxicity in a neuronal cell line,” *Brain Res.*, vol. 652, no. 1, pp. 169–173, 1994.

[75] X.-H. Chen, S. J. Beebe, and S.-S. Zheng, “Tumor ablation with nanosecond pulsed electric fields,” *Hepatobiliary Pancreat. Dis. Int.*, vol. 11, no. 2, pp. 122–124, 2012.

[76] A. G. Pakhomov, J. F. Kolb, J. A. White, R. P. Joshi, S. Xiao, and K. H. Schoenbach, “Long-lasting plasma membrane permeabilization in mammalian cells by nanosecond pulsed electric field (nsPEF),” *Bioelectromagnetics*, vol. 28, no. 8, pp. 655–663, 2007.

[77] P. T. Vernier, Y. Sun, and M. A. Gundersen, “Nanoelectropulse-driven membrane perturbation and small molecule permeabilization,” *BMC Cell Biol.*, vol. 7, no. 1, p. 37, 2006.

[78] J. Song, R. P. Joshi, and K. H. Schoenbach, “Synergistic effects of local temperature enhancements on cellular responses in the context of high-intensity, ultrashort electric pulses,” *Med. Biol. Eng. Comput.*, vol. 49, no. 6, pp. 713–718, 2011.

[79] D. Moreau, C. Lefort, R. Burke, P. Leveque, and R. P. O’Connor, “Rhodamine B as an optical thermometer in cells focally exposed to infrared laser light or nanosecond pulsed electric fields,” *Biomed. Opt. Express*, vol. 6, no. 10, pp. 4105–4117, 2015.

[80] H. T. Beier, G. P. Tolstykh, J. D. Musick, R. J. Thomas, and B. L. Ibey, “Plasma membrane nanoporation as a possible mechanism behind infrared excitation of cells,” *J. Neural Eng.*, vol. 11, no. 6, p. 66006, 2014.

[81] N. I. Smith *et al.*, “Generation of calcium waves in living cells by pulsed-laser-induced photodisruption,” *Appl. Phys. Lett.*, vol. 79, no. 8, pp. 1208–1210, 2001.

[82] G. Buzsáki, C. A. Anastassiou, and C. Koch, “The origin of extracellular fields and currents — EEG, ECoG, LFP and spikes,” *Nat Rev Neurosci*, vol. 13, no. 6, pp. 407–420, Jun. 2012.

[83] M. Sessolo *et al.*, “Easy-to-Fabricate Conducting Polymer Microelectrode Arrays,” *Adv. Mater.*, vol. 25, no. 15, pp. 2135–2139, 2013.

[84] N. Kallweit *et al.*, “Optoacoustic effect is responsible for laser-induced cochlear responses,” *Sci. Rep.*, vol. 6, 2016.

[85] S. K. Calderwood, M. A. Stevenson, and B. D. Price, “Activation of phospholipase C by heat shock requires GTP analogs and is resistant to pertussis toxin,” *J. Cell.*

Physiol., vol. 156, no. 1, pp. 153–159, 1993.

[86] Y. Wu, O. Perisic, R. L. Williams, M. Katan, and M. F. Roberts, “Phosphoinositide-specific phospholipase C δ1 activity toward micellar substrates, inositol 1, 2-cyclic phosphate, and other water-soluble substrates: a sequential mechanism and allosteric activation,” *Biochemistry*, vol. 36, no. 37, pp. 11223–11233, 1997.

[87] J.-F. Dufour, I. M. Arias, and T. J. Turner, “Inositol 1, 4, 5-trisphosphate and calcium regulate the calcium channel function of the hepatic inositol 1, 4, 5-trisphosphate receptor,” *J. Biol. Chem.*, vol. 272, no. 5, pp. 2675–2681, 1997.

[88] H. Chuang *et al.*, “Bradykinin and nerve growth factor release the capsaicin receptor from PtdIns (4, 5) P2-mediated inhibition,” *Nature*, vol. 411, no. 6840, pp. 957–962, 2001.

[89] N. Takahashi *et al.*, “TRPV4 channel activity is modulated by direct interaction of the ankyrin domain to PI (4, 5) P2,” *Nat. Commun.*, vol. 5, 2014.

[90] K. Venkatachalam and C. Montell, “TRP channels,” *Annu. Rev. Biochem.*, vol. 76, pp. 387–417, 2007.

[91] A. K. Ho and D. C. Klein, “Activation of alpha 1-adrenoceptors, protein kinase C, or treatment with intracellular free Ca2+ elevating agents increases pineal phospholipase A2 activity. Evidence that protein kinase C may participate in Ca2+-dependent alpha 1-adrenergic stimulation o,” *J. Biol. Chem.*, vol. 262, no. 24, pp. 11764–11770, 1987.

[92] M. Peters-Golden, R. W. McNish, J. K. Brieland, and J. C. Fantone, “Diminished protein kinase C-activated arachidonate metabolism accompanies rat macrophage differentiation in the lung.,” *J. Immunol.*, vol. 144, no. 11, pp. 4320–4326, 1990.

[93] H. Watanabe, J. Vriens, J. Prenen, G. Droogmans, T. Voets, and B. Nilius, “Anandamide and arachidonic acid use epoxyeicosatrienoic acids to activate TRPV4 channels,” *Nature*, vol. 424, no. 6947, pp. 434–438, 2003.

[94] C. Xu and L. M. Loew, “Activation of phospholipase C increases intramembrane electric fields in N1E-115 neuroblastoma cells,” *Biophys. J.*, vol. 84, no. 6, pp. 4144–4156, 2003.

[95] D. Moreau, C. Lefort, J. Pas, S. M. Bardet, P. Leveque, and R. P. O’Connor, “Infrared neural stimulation induces intracellular Ca2+ release mediated by phospholipase C,” *J. Biophotonics*, p. e201700020–n/a.

[96] C. Stosiek, O. Garaschuk, K. Holthoff, and A. Konnerth, “In vivo two-photon calcium imaging of neuronal networks,” *Proc. Natl. Acad. Sci.*, vol. 100, no. 12, pp. 7319–7324, 2003.

[97] J. Nakai, M. Ohkura, and K. Imoto, “A high signal-to-noise Ca2+ probe composed of a single green fluorescent protein,” *Nat. Biotechnol.*, vol. 19, no. 2, pp. 137–141, 2001.

[98] H. Dana *et al.*, “Thy1-GCaMP6 transgenic mice for neuronal population imaging in vivo,” *PLoS One*, vol. 9, no. 9, p. e108697, 2014.

[99] J. T. Lock, I. Parker, and I. F. Smith, “A comparison of fluorescent Ca 2+ indicators for imaging local Ca 2+ signals in cultured cells,” *Cell Calcium*, vol. 58, no. 6, pp. 638–648, 2015.

[100] T.-W. Chen *et al.*, “Ultra-sensitive fluorescent proteins for imaging neuronal activity,” *Nature*, vol. 499, no. 7458, p. 295, 2013.

Annexes

Annex 1 t-Table

df/p	0.40	0.25	0.10	0.05	0.025	0.01	0.005	0.0005
1	0.324920	1.000000	3.077684	6.313752	12.70620	31.82052	63.65674	636.6192
2	0.288675	0.816497	1.885618	2.919986	4.30265	6.96456	9.92484	31.5991
3	0.276671	0.764892	1.637744	2.353363	3.18245	4.54070	5.84091	12.9240
4	0.270722	0.740697	1.533206	2.131847	2.77645	3.74695	4.60409	8.6103
5	0.267181	0.726687	1.475884	2.015048	2.57058	3.36493	4.03214	6.8688
6	0.264835	0.717558	1.439756	1.943180	2.44691	3.14267	3.70743	5.9588
7	0.263167	0.711142	1.414924	1.894579	2.36462	2.99795	3.49948	5.4079
8	0.261921	0.706387	1.396815	1.859548	2.30600	2.89646	3.35539	5.0413
9	0.260955	0.702722	1.383029	1.833113	2.26216	2.82144	3.24984	4.7809
10	0.260185	0.699812	1.372184	1.812461	2.22814	2.76377	3.16927	4.5869
11	0.259556	0.697445	1.363430	1.795885	2.20099	2.71808	3.10581	4.4370
12	0.259033	0.695483	1.356217	1.782288	2.17881	2.68100	3.05454	43178
13	0.258591	0.693829	1.350171	1.770933	2.16037	2.65031	3.01228	4.2208
14	0.258213	0.692417	1.345030	1.761310	2.14479	2.62449	2.97684	4.1405
15	0.257885	0.691197	1.340606	1.753050	2.13145	2.60248	2.94671	4.0728
16	0.257599	0.690132	1.336757	1.745884	2.11991	2.58349	2.92078	4.0150
17	0.257347	0.689195	1.333379	1.739607	2.10982	2.56693	2.89823	3.9651
18	0.257123	0.688364	1.330391	1.734064	2.10092	2.55238	2.87844	3.9216
19	0.256923	0.687621	1.327728	1.729133	2.09302	2.53948	2.86093	3.8834
20	0.256743	0.686954	1.325341	1.724718	2.08596	2.52798	2.84534	3.8495
21	0.256580	0.686352	1.323188	1.720743	2.07961	2.51765	2.83136	3.8193
22	0.256432	0.685805	1.321237	1.717144	2.07387	2.50832	2.81876	3.7921
23	0.256297	0.685306	1.319460	1.713872	2.06866	2.49987	2.80734	3.7676
24	0.256173	0.684850	1.317836	1.710882	2.06390	2.49216	2.79694	3.7454
25	0.256060	0.684430	1.316345	1.708141	2.05954	2.48511	2.78744	3.7251
26	0.255955	0.684043	1.314972	1.705618	2.05553	2.47863	2.77871	3.7066
27	0.255858	0.683685	1.313703	1.703288	2.05183	2.47266	2.77068	3.6896
28	0.255768	0.683353	1.312527	1.701131	2.04841	2.46714	2.76326	3.6739
29	0.255684	0.683044	1.311434	1.699127	2.04523	2.46202	2.75639	3.6594
30	0.255605	0.682756	1.310415	1.697261	2.04227	2.45726	2.75000	3.6460

Annex 2 Article published in Biomedical Optics Express

Biomedical Optics EXPRESS

Rhodamine B as an optical thermometer in cells focally exposed to infrared laser light or nanosecond pulsed electric fields

David Moreau,[1,*] Claire Lefort,[1] Ryan Burke,[1] Philippe Leveque,[1] and Rodney P. O'Connor[1]

[1]*Univ. Limoges, CNRS, XLIM, UMR 7252, F-87000 Limoges, France*
[*]*david.moreau@xlim.fr*

Abstract: The temperature-dependent fluorescence property of Rhodamine B was used to measure changes in temperature at the cellular level induced by either infrared laser light exposure or high intensity, ultrashort pulsed electric fields. The thermal impact of these stimuli were demonstrated at the cellular level in time and contrasted with the change in temperature observed in the extracellular bath. The method takes advantage of the temperature sensitivity of the fluorescent dye Rhodamine B which has a quantum yield linearly dependent on temperature. The thermal effects of different temporal pulse applications of infrared laser light exposure and of nanosecond pulsed electric fields were investigated. The temperature increase due to the application of nanosecond pulsed electric fields was demonstrated at the cellular level.

OCIS codes: (170.2520) Fluorescence microscopy; (280.6780) Temperature; (260.3060) Infrared.

References and links

1. E. E. Hoover and J. A. Squier, "Advances in multiphoton microscopy technology," Nat. Photonics **7**(2), 93–101 (2013).
2. B.-H. Li, S.-S. Xie, Z. Huang, and B. C. Wilson, "Advances in photodynamic therapy dosimetry," Prog. Biochem. Biophys. **36**(6), 676–683 (2009).
3. C.-P. Richter and X. Tan, "Photons and neurons," Hear. Res. **311**, 72–88 (2014).
4. J.-M. Bec, E. S. Albert, I. Marc, G. Desmadryl, C. Travo, A. Muller, C. Chabbert, F. Bardin, and M. Dumas, "Characteristics of laser stimulation by near infrared pulses of retinal and vestibular primary neurons," Lasers Surg. Med. **44**(9), 736–745 (2012).
5. A. J. Welch, "The thermal response of laser irradiated tissues," IEEE J. Quantum Electron. **20**(12), 1471–1481 (1984).
6. E. S. Albert, J. M. Bec, G. Desmadryl, K. Chekroud, C. Travo, S. Gaboyard, F. Bardin, I. Marc, M. Dumas, G. Lenaers, C. Hamel, A. Muller, and C. Chabbert, "TRPV4 channels mediate the infrared laser-evoked response in sensory neurons," J. Neurophysiol. **107**(12), 3227–3234 (2012).
7. M. G. Shapiro, K. Homma, S. Villarreal, C.-P. Richter, and F. Bezanilla, "Infrared light excites cells by changing their electrical capacitance," Nat. Commun. **3**, 736 (2012).
8. R. Liljemalm, T. Nyberg, and H. von Holst, "Heating during infrared neural stimulation," Lasers Surg. Med. **45**(7), 469–481 (2013).
9. R. P. Joshi, A. Mishra, J. Song, A. G. Pakhomov, and K. H. Schoenbach, "Simulation studies of ultrashort, high-intensity electric pulse induced action potential block in whole-animal nerves," IEEE Trans. Biomed. Eng. **55**(4), 1391–1398 (2008).
10. X. H. Chen, S. J. Beebe, and S. S. Zheng, "Tumor ablation with nanosecond pulsed electric fields," HBPD INT **11**(2), 122–124 (2012).
11. A. G. Pakhomov, J. F. Kolb, J. A. White, R. P. Joshi, S. Xiao, and K. H. Schoenbach, "Long-lasting plasma membrane permeabilization in mammalian cells by nanosecond pulsed electric field (nsPEF)," Bioelectromagn. **28**(8), 655–663 (2007).
12. P. T. Vernier, Y. Sun, and M. A. Gundersen, "Nanoelectropulse-driven membrane perturbation and small molecule permeabilization," BMC Cell Biol. **7**(1), 37 (2006).
13. J. Song, R. P. Joshi, and K. H. Schoenbach, "Synergistic effects of local temperature enhancements on cellular responses in the context of high-intensity, ultrashort electric pulses," Med. Biol. Eng. Comput. **49**(6), 713–718 (2011).

#247362 Received 6 Aug 2015; revised 19 Sep 2015; accepted 22 Sep 2015; published 24 Sep 2015

14. G. Baffou, H. Rigneault, D. Marguet, and L. Jullien, "A critique of methods for temperature imaging in single cells," Nat. Methods **11**(9), 899–901 (2014).
15. L. Shang, F. Stockmar, N. Azadfar, and G. U. Nienhaus, "Intracellular Thermometry by Using Fluorescent Gold Nanoclusters," Angew. Chem. Int. Ed. Engl. **52**(42), 11154–11157 (2013).
16. J. S. Donner, S. A. Thompson, M. P. Kreuzer, G. Baffou, and R. Quidant, "Mapping Intracellular Temperature Using Green Fluorescent Protein," Nano Lett. **12**(4), 2107–2111 (2012).
17. L. M. Maestro, E. M. Rodriguez, F. S. Rodriguez, M. C. la Cruz, A. Juarranz, R. Naccache, F. Vetrone, D. Jaque, J. A. Capobianco, and J. G. Solé, "CdSe Quantum Dots for Two-Photon Fluorescence Thermal Imaging," Nano Lett. **10**(12), 5109–5115 (2010).
18. O. Zohar, M. Ikeda, H. Shinagawa, H. Inoue, H. Nakamura, D. Elbaum, D. L. Alkon, and T. Yoshioka, "Thermal imaging of receptor-activated heat production in single cells," Biophys. J. **74**(1), 82–89 (1998).
19. F. Vetrone, R. Naccache, A. Zamarrón, A. Juarranz de la Fuente, F. Sanz-Rodriguez, L. Martinez Maestro, E. Martín Rodriguez, D. Jaque, J. García Solé, and J. A. Capobianco, "Temperature sensing using fluorescent nanothermometers," ACS Nano **4**(6), 3254–3258 (2010).
20. L. Yang, H.-S. Peng, H. Ding, F.-T. You, L.-L. Hou, and F. Teng, "Luminescent Ru(bpy)3 2+-doped silica nanoparticles for imaging of intracellular temperature," Mikrochim. Acta **181**(7–8), 743–749 (2013).
21. J. Ferguson and A. W. H. Mau, "Spontaneous and stimulated emission from dyes. Spectroscopy of the neutral molecules of acridine orange, proflavine, and rhodamine B," Aust. J. Chem. **26**(8), 1617–1624 (1973).
22. R. F. Kubin and A. N. Fletcher, "Fluorescence quantum yields of some rhodamine dyes," J. Lumin. **27**(4), 455–462 (1982).
23. J. J. Shah, M. Gaitan, and J. Geist, "Generalized temperature measurement equations for Rhodamine B dye solution and its application to microfluidics," Anal. Chem. **81**(19), 8260–8263 (2009).
24. U. Seger-Sauli, M. Panayiotou, S. Schnydrig, M. Jordan, and P. Renaud, "Temperature measurements in microfluidic systems: heat dissipation of negative dielectrophoresis barriers," Electrophoresis **26**(11), 2239–2246 (2005).
25. J. J. Shah, S. G. Sundaresan, J. Geist, D. R. Reyes, J. C. Booth, M. V. Rao, and M. Gaitan, "Microwave dielectric heating of fluids in an integrated microfluidic device," J. Micromech. Microeng. **17**(11), 2224 (2007).
26. L. Gui and C. L. Ren, "Temperature measurement in microfluidic chips using photobleaching of a fluorescent thin film," Appl. Phys. Lett. **92**(2), 024102 (2008).
27. D. Ross, M. Gaitan, and L. E. Locascio, "Temperature measurement in microfluidic systems using a temperature-dependent fluorescent dye," Anal. Chem. **73**(17), 4117–4123 (2001).
28. P. Löw, B. Kim, N. Takama, and C. Bergaud, "High-Spatial-Resolution Surface-Temperature Mapping Using Fluorescent Thermometry," Small **4**(7), 908–914 (2008).
29. J. Sakakibara and R. J. Adrian, "Whole field measurement of temperature in water using two-color laser induced fluorescence," Exp. Fluids **26**(1–2), 7–15 (1999).
30. P. Reungpatthanaphong, S. Dechsupa, J. Meesungnoen, C. Loetchutinat, and S. Mankhetkorn, "Rhodamine B as a mitochondrial probe for measurement and monitoring of mitochondrial membrane potential in drug-sensitive and -resistant cells," J. Biochem. Biophys. Methods **57**(1), 1–16 (2003).
31. Y. Y. Chen and A. W. Wood, "Application of a temperature-dependent fluorescent dye (Rhodamine B) to the measurement of radiofrequency radiation-induced temperature changes in biological samples," Bioelectromagnetics **30**(7), 583–590 (2009).
32. S. Kohler, R. P. O'Connor, T. D. Thao Vu, P. Leveque, and D. Arnaud-Cormos, "Experimental microdosimetry techniques for biological cells exposed to nanosecond pulsed electric fields using microfluorimetry," IEEE Trans. Microw. Theory Tech. **61**(5), 2015–2022 (2013).
33. D. Arnaud-Cormos, P. Leveque, Y. H. Wu, J. M. Sanders, M. A. Gundersen, and P. T. Vernier, "Microchamber setup characterization for nanosecond pulsed electric field exposure," IEEE Trans. Biomed. Eng. **58**(6), 1656–1662 (2011).

1. Introduction

Near infrared laser light is used in many biological applications, including multiphoton microscopy [1], photodynamic therapy [2] and neural stimulation [3,4]. The exposure of biological tissues to infrared laser light poses a recurring question [5]: is the tissue health compromised due to the infrared exposure and does this transient hyperthermic stress cause any persistent damage to the cell? In the field of neural stimulation, this question concerns the mechanism of action and specifically whether it has a thermal effect acting on temperature sensitive ion channels [6] or a more direct effect on membrane capacitance due to the gradient of temperature [7]. One of the important challenges in understanding the effect of infrared exposure on biological tissues is the quantification of the local temperature in the exposed cells [8].

Similarly, nanosecond pulsed electric fields (nsPEFs) are an emerging tool with potential for both neurostimulation [9] and cancer treatment [10], depending on the intensity and pulse duration used. nsPEFs can be used to transiently permeabilize the plasma membranes of cells [11,12], but despite having high peak power, the effect of these ultrashort pulses are

#247362 Received 6 Aug 2015; revised 19 Sep 2015; accepted 22 Sep 2015; published 24 Sep 2015

considered to be nonthermal due to the low average energy density that they deliver. Interestingly, it has been shown analytically that the application of nsPEFs to cells could result in both thermal (Joule heating) and electrical effects [13]. Thus, like infrared laser light, local temperature measurements of biological samples exposed to nsPEFs are necessary to better understand the mechanisms involved in these effects.

A number of different microscopy techniques can be used to map temperature at the single-cell level to study thermal effects caused by infrared laser light or electrical sources [14] and each has its strengths and weaknesses. For example, Shang and colleagues [15] demonstrated the utility of fluorescence lifetime microscopy for cellular and subcellular measurements of temperature; however, this method is highly sensitive to pH and viscosity. Another highly promising technique is based on the anisotropy of fluorescence from green fluorescent protein [16], yet this requires the use of cell lines stably expressing fluorescent proteins, making it less suitable for studies of neurons or primary tissues that are difficult to transfect. A wide variety of other methods have been used, taking advantage of the temperature sensitivity of fluorescent quantum dots [17], Europium thenoyltrifluoroacetonate (EuTTA) [18], Er^{3+}-doped nanoparticles [19] or doped silica nanoparticles containing a combination of these substances [20]. The application of these techniques is limited by the toxicity of these substances and differential uptake and repartition in into organelles and membranes.

Rhodamine B (RhB) is a well-known water soluble fluorophore, with an absorption peak centered at 554 nm, and an emission peak at 576 nm. In the current context, the most interesting property of this molecule is its temperature dependent fluorescence quantum yield [21], which decreases linearly as temperature increases [22]. The fluorescence of RhB is negligibly pressure sensitive and pH independent above a pH of 6 [23]. RhB has been used in several microfluidic applications [24–29], and interestingly, distributes across biological membranes where it has been used as a mitochondrial probe [30]. These properties lead us to test whether RhB dye could be successfully used as optical thermometer in small biological compartments at the subcellular level. It has been used recently in the measurement of temperature in rat tail tendon samples exposed to radiofrequency electromagnetic fields [31], and similarly used in our group to measure temperature in cells exposed to continuous wave microwaves [32].

In this paper, we present experiments applying RhB to measure temperature at the cellular level to highlight the temperature changes induced in cells focally exposed to infrared laser light at 800 nm or 10 ns pulsed electric fields. First, the setup and the calibration procedure are detailed. Then, the different exposure systems are described that were used to deliver infrared laser light or nsPEFs to U87 human cancer cells during imaging experiments. The thermal effect of continuous infrared exposure was investigated, including the influence of the power of the radiation used and the distance between the source of infrared and the cells. The effects of an intermittent infrared exposure on the temperature of the cells was also investigated. Finally, the influence of nsPEFs on local cellular temperature was studied as a function of intensity, pulse number and repetition frequency. In the case of the exposure to nsPEFs, the temperature measurements made with RhB were compared with those completed with a calibrated external thermometer. In both cases, the local increase of temperature due to nsPEFs was demonstrated. RhB was therefore a highly sensitive and useful tool for investigating the cellular-level temperature impact of these stimuli.

2. Experimental setup

Figure 1(a) shows the experimental setup used for both infrared and nsPEFs exposure experiments that was located in a room with a stabilized temperature at 23°C. The setup can be divided into three parts, including the systems for imaging and measuring the temperature (lower part of the figure) and the systems for controlling and exposing cells to infrared laser light (upper right part of the figure) and to nsPEFs (upper left part of the figure). Figure 1(b) shows an expanded view of the petri dish when the nsPEFs delivery system was applied (left part of the figure) and when the infrared delivery system was used (right part of the figure).

#247362 Received 6 Aug 2015; revised 19 Sep 2015; accepted 22 Sep 2015; published 24 Sep 2015

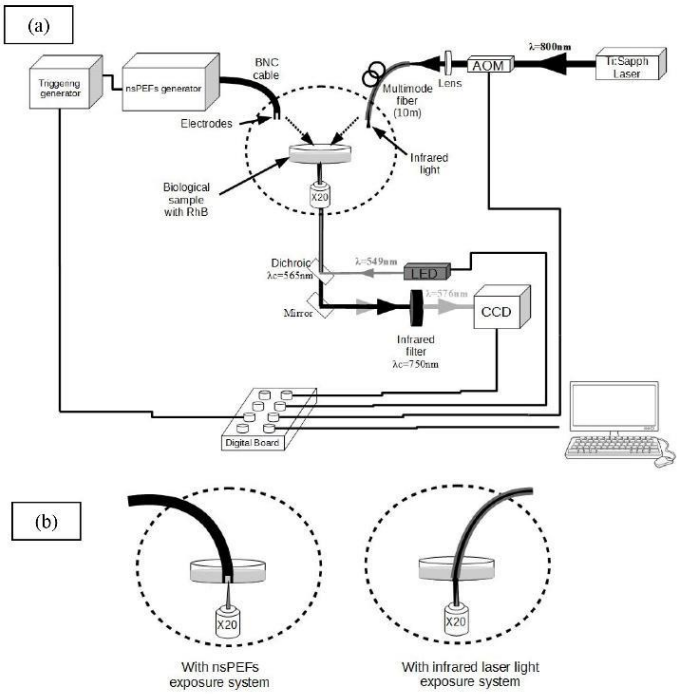

Fig. 1. (a). Experimental setup. (b) Zoom on the delivery of nsPEFs and infrared in the petri dish.

2.1. Rhodamine B fluorescence intensity measurement and conversion to temperature

The setup allowed the detection of the RhB fluorescence using wide field epifluorescence microscope (Leica DMI6000 B). The excitation light for RhB (λ = 549 nm) was provided by a light emitting diode (LED)-based light engine (Spectra7, Lumencor). This light, with an average power of 3.5 mW, was delivered to the cells with a dichroic mirror centered at 565 nm. A 20X objective was used to focus the light from the LED in the petri dish containing the cells loaded with RhB. The fluorescence emission (peak λ = 576 nm) of RhB was then collected through the dichroic mirror and separated from any infrared light with a longpass filter (λ_c = 750 nm) and detected with a electron-multiplying charge-coupled device camera (EM-CCD, 16 bit, pixel matrix 512x512, Evolve 512, Photometrics). All elements in the fluorescence imaging setup were controlled and synchronized by freely available software (Winfluor, Strathclyde University). The parameters of acquisition of the CCD was controlled as well as the LED engine by the software and by an analog output from digital acquisition (DAQ) board (USB-6229-BNC, National Instruments).

The calibration procedure was divided in two steps that occured simultaneously. Fig. 2 shows an example of the conversion of the fluorescence into temperature. For this calibration procedure, RhB was diluted in 2.5 mL of water in a petri dish to a final concentration of 50 µM. The petri dish was placed in a metallic ring containing a resistive element and

#247362 Received 6 Aug 2015; revised 19 Sep 2015; accepted 22 Sep 2015; published 24 Sep 2015

temperature controller (TC-E35, Bioscience Tools). The whole solution was heated from 23°C to 29°C by the heater element. At the same time, the evolution of the fluorescence intensity was recorded by the imaging software and was synchronized with the output voltage of the fiber thermometer. Fig. 2(a) shows an example of these results. A calibrated fiber optic thermometer (LUXTRON 812 Industrial Temperature Monitor) with an analog voltage output was used that allowed extraction of a linear relationship between the temperature of the sample (measured with the thermometer) and the voltage output of the fiber thermometer, as acquired by software. Fig. 2(b) shows a recording of the temperature over time. Finally, by extracting the previous results in time, it was possible to extract the relationship between the evolution of the fluorescence intensity and the change of temperature. This setup therefore allowed measurement of the evolution of fluorescence intensity with the temperature of the RhB. Ten calibration procedures were performed and the average decrease of fluorescence intensity with temperature was found to be linear and estimated at 1.63% +/–0.2 per Celsius degree.

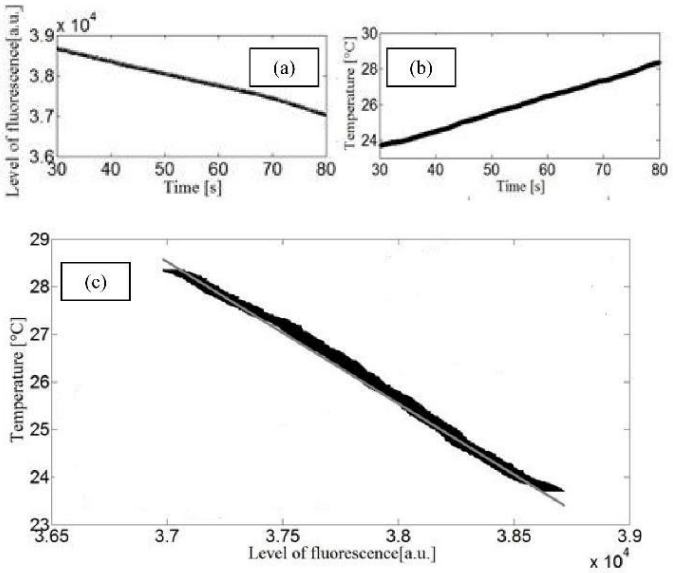

Fig. 2. (a). recording of the level of fluorescence versus time. (b). recording of the temperature with external thermometer versus time. (c). Conversion of fluorescence intensity into temperature. Results of measurement in black, linear fit in grey.

2.2. Shaping and routing of infrared laser light excitation

The infrared laser source was a femtosecond-pulsed tunable Titanium-Sapphire oscillator (Chameleon, Coherent, INC, 680-1080 nm, 10 nm, 140 fs, 4 W, 80 MHz). The central wavelength was fixed at 805 nm for all experiments. The laser beam was injected into a 10-m-long multimode graded-index fiber (GIF50C, Thorlabs). The fiber had a core diameter of 50 µm and a numerical aperture of 0.2, and caused a spectral broadening as presented in Fig. 3. The infrared laser light brought to the biological samples therefore had a spectral width of 19 nm at the full width half maximum (FWHM).

#247362 Received 6 Aug 2015; revised 19 Sep 2015; accepted 22 Sep 2015; published 24 Sep 2015

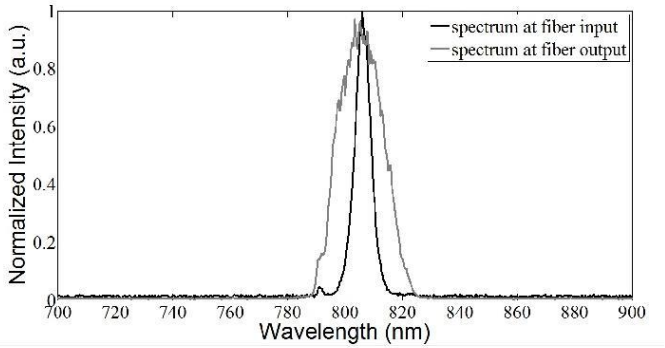

Fig. 3. Spectral broadening due to the fiber.

A maximum average power of 0.7 W was available at the fiber output, representing an injection efficiency of 78%. The infrared laser was rapidly modulated by an acousto-optical modulator (AOM, MT110IR, AA Optoelectronic), inserted before the fiber input. Transmission through the AOM was controlled by software and by the digital acquisition board allowing rapid and precise temporal control of infrared power to the biological samples. The switching delay between application of the voltage on the AOM and the response at the fiber output was measured to be 250 µs.

2.3. nsPEF delivery system

To study the impact of nsPEFs on local temperature, the nsPEF delivery system replaced the infrared delivery system (Fig. 1). The nanosecond pulse generator (FID Technology, 10 kV maximum voltage, 50 Ohm output impedance, 10 ns pulse width) was triggered by a function generator (Agilent 33120A) controlled by a custom Labview program (Labview 7.1, National Instruments). The trigger signal consisted of square pulses with a duty cycle of 10% and was recorded by the DAQ board during all experiments. The electric pulses delivered to electrodes by a high voltage cable. Bipolar electrodes were separated by a distance of 1.5 mm and connected in parallel to a 50 Ohm resistor to impedance-match the nsPEF generator, as previously described [33].

2.4. Preparation of U87 cell culture labelled with RhB

Human U87 glioblastoma cells were purchased from American Type Culture Collection (ATCC) and grown in Minimum Essential Media (MEM) supplemented with fetal bovine serum, glutamine and antibiotics and kept in an incubator under a 5% CO_2 atmosphere. Cells were detached with trypsin and subcultured onto glass bottomed petri dishes (Fluodish, WPI) and allowed to attach to glass in the incubator for 24 hours before experiments. Culture media was then removed from petri dishes containing adherent U87 cells, and replaced with a 50 µM RhB concentration made in a physiologically balanced HEPES buffered salt solution (HBSS) pH-buffered to 7.4. Cells were incubated with RhB for 2 hours to allow for dye incorporation. After the loading period, petri dishes were washed twice with fresh HBSS in order to remove extracellular dye and finally placed on the microscope stage.

3. Measurement of temperature of cells under infrared exposure

Figure 4 shows the image of the cells as detected by the CCD camera from the fluorescence of the RhB inside cells. It also shows an example of an area illuminated by the infrared laser from the optical fiber and an example of a region of interest (ROI) that was analyzed. Single cell ROIs were thus defined after positioning the infrared exposure area with a

#247362 Received 6 Aug 2015; revised 19 Sep 2015; accepted 22 Sep 2015; published 24 Sep 2015

micromanipulator. This ROI delimited the pixels that were considered in the recording of fluorescence intensity over time. The fluorescence intensity values of the pixels located in the ROI were averaged in order to extract the mean fluorescence intensity.

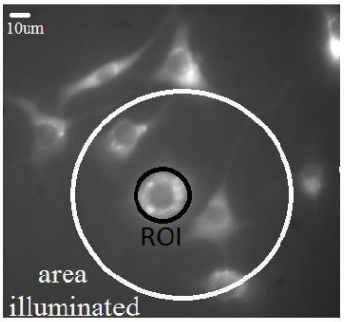

Fig. 4. Image of the cells labelled with RhB. Localisation of the infrared exposure area and definition of the region of interest where the cell temperature is measured.

3.1. Continuous infrared exposure

The first example of infrared laser exposure considered was a continuous application with a duration of 60 s and an average power at the fiber output of 200 mW (Fig. 5) . The optical fiber was placed 0.5 mm above the cells. The LED illumination occurred for a total duration of 200 s. High temporal resolution was not required in this case, so imaging was performed with temporal sampling of 200 ms in order to increase the signal to noise ratio. Infrared exposure induced an initial fast increase of temperature of 1.5 °C and eventually reached a steady state with the thermal balance between the contribution of energy by the infrared radiation and the thermal exchange with the extracellular bath. This steady state was observed when the temperature of the system stabilized and did not vary more than +/– 0.1 °C. After the end of the exposure, the temperature of the cell returned to its basal value (23 °C), demonstrating that the change in fluorescence of RhB with temperature was reversible. Experiments performed to examine the photobleaching of RhB by the LED illumination (data not shown) revealed an exponential term that could be approximated by a linear trend after 10 minutes, corresponding to a decrease of -2.10^{-3} °C/s. Before each experiments, we exposed the RhB to the LED illumination until we reached this linear decrease. All the following results were therefore corrected for this linear trend.

#247362 Received 6 Aug 2015; revised 19 Sep 2015; accepted 22 Sep 2015; published 24 Sep 2015

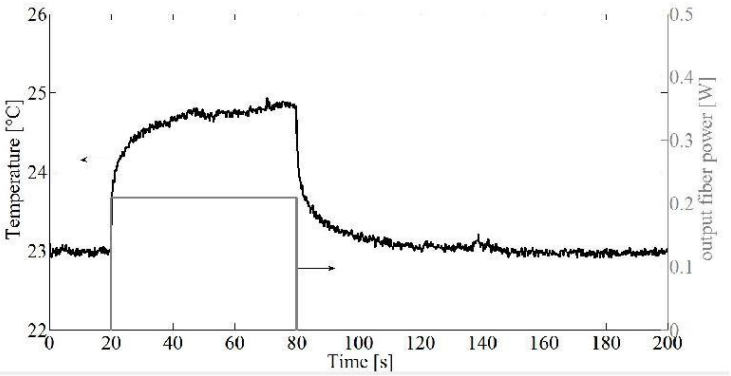

Fig. 5. Temperature measurement of cell under continuous infrared exposure.

3.2. Study of the impact of output fiber power

The impact of the average power at the output of the fiber on the temperature increase in cells was investigated. The average power at the output of the multimode fiber was varied from 100 mW to 700 mW by steps of 100 mW. The temporal resolution was set at 200 ms during a recording period of 200 s and the fiber output was positioned 0.5 mm above the cells. Fig. 6(a) presents the evolution of the temperature in the ROI. A linear dependence of the increase of temperature reached at the steady state with the infrared laser light power is highlighted in Fig. 6(b) . As expected, the temperature increase was higher with the use of infrared radiation with higher average power. Indeed, the change in temperature varied from nearly 0.5 °C at 100 mW) to nearly 5°C at 700 mW. The time constant, determined as the time when the temperature increase reached 63% of the final increase was found to be 2.4 s (+/–0.2 s) for all the power used as predicted by the linearity of the heat diffusion equation.

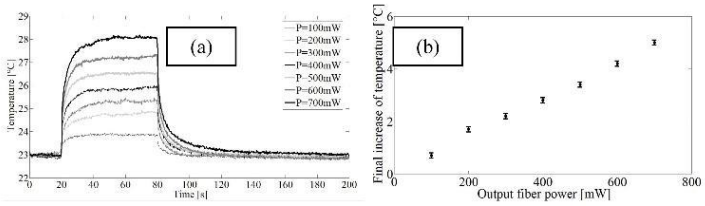

Fig. 6. (a). Evolution of temperature in cells depending on the average power P. (b). Evolution of the final increase of temperature depending on the average power at the output of the fiber with error bars illustrating the +/–0.1 °C of incertitude.

3.3. Intermittent pulsed infrared exposure

Intermitttent rectangular pulses of infrared exposure were used to evaluate the temporal resolution of the method. The average power at the output of the fiber was 500 mW and the fiber was maintained at a distance of 0.5 mm from the cells. The infrared exposure started after a baseline recording of 5 s and consisted of a series of 100 ms pulses modulated by the AOM each with a duration of 100 ms and delay of 50 ms (duty cycle = 67%) over a period of approximately 10 s. Fig. 7 presents the results. A magnified view of the temporal pattern of

#247362 Received 6 Aug 2015; revised 19 Sep 2015; accepted 22 Sep 2015; published 24 Sep 2015

the optical exposure is shown in the inset of Fig. 7 . The best temporal resolution that could be obtained was approximately 4 ms due to limitations in the camera readout and LED control speed. The intermittent infrared exposure induced a global increase of temperature of nearly 3.5 °C, from 23 °C to 26.5 °C. Furthermore, each pulse induced a small increase of temperature whereas the delay between pulses was associated with decrease of temperature not sufficient to return at the basal value. Unfortunately, the noise present in the measurement, due to the low integration time needed on the camera, prevented us to estimate obviously the value of the increase of temperature induced by one single pulse.

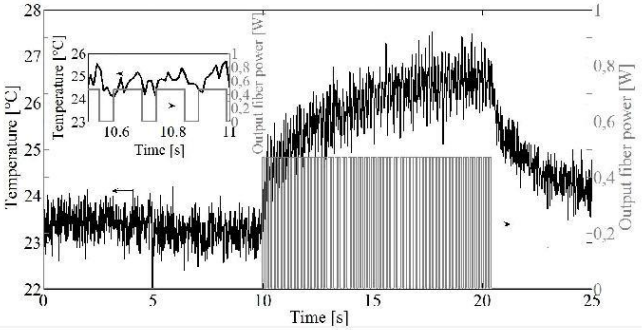

Fig. 7. Intermittent infrared exposure. Inset. Zoom from 10.5 s to 11 s.

4. Application of the optical measurement of temperature to cells exposed to nsPEFs

Given that RhB showed promise in measuring rapid temperature changes caused by infrared exposure, the method was used to study the impact of nsPEFs on local temperature at the cellular level. The bipolar electrodes were positioned with a micromanipulator so that the cells of interest were located in the field of view of the microscope and between the electrodes. ROIs were chosen selecting cells in the center of the field of view. In order to understand the contribution of pulse number and repetition frequency to potential heating at the cellular level, different pulse applications were tested from 1 single nsPEF to 100 nsPEFs with a frequency of 100 Hz including the configurations using 10 nsPEFs at 10 and 100 Hz and 100 at 10 Hz. Pulses were 10 ns long with an associated electric field between the electrodes of 44.1 kV/cm. The pulse trigger signal was recorded and synchronized with the measurement of RhB fluorescence using a temporal resolution of 200 ms so that the evolution of temperature with each pulse could be considered locally at the cellular level.

At the same time, temperature in the extracellular bath between the electrodes was measured and recorded with the fiber optic temperature sensor (Luxton). The Luxton fiber probe is a specialized temperature sensor that is immune to radiofrequency and high voltage interferences. These combination of the cellular measurement of temperature with RhB and the extracellular recordings with the Luxtron sensor allowed the comparison of their relative sensitivities to local temperature changes with time.

The results of these two techniques are shown in Fig. 8 . Table 1 summarizes the temperature changes as measured by RhB fluorescence and the Luxtron temperature probe.

#247362 Received 6 Aug 2015; revised 19 Sep 2015; accepted 22 Sep 2015; published 24 Sep 2015

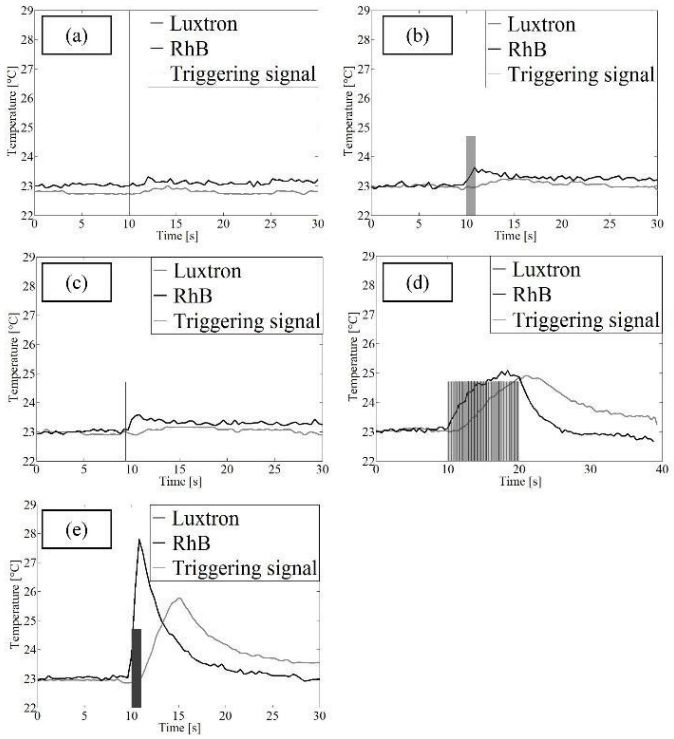

Fig. 8. Temperature modification induced by nsPEFs as simultaneously measured by RhB fluorescence and Luxtron thermometer. (a). 1 single pulse. (b). 10 nsPEFs at 10 Hz. (c). 10 nsPEFs at 100 Hz. (d). 100 nsPEFs at 10 Hz. (e). 100 nsPEFs at 100 Hz.

Table 1. Recapitulative of temperature increases for both techniques and all parameters used.

		Number of pulses					
		1		10		100	
		RhB	Luxtron	RhB	Luxtron	RhB	Luxtron
Frequency (Hz)	10	0°C	0°C	0.6°C	0.3°C	2.1°C	2°C
	100	0°C	0°C	0.6°C	0.3°C	4.8°C	2.8°C

No significant temperature changes were observed with the delivery of a single 10ns pulse with either the RhB measurement at the cellular level or the Luxtron probe between the electrodes (Fig. 8(a)) . With the application of 10 nsPEFs, for both 10 Hz and 100 Hz the temperature elevation was measured at 0.6°C with RhB fluorescence. The influence of pulse repetition is apparent in the application of 100 nsPEFs since at 10 Hz, an increase of 2.1°C was detected whilst 4.8°C was observed at 100 Hz. The increase of the number of pulses also

#247362 Received 6 Aug 2015; revised 19 Sep 2015; accepted 22 Sep 2015; published 24 Sep 2015

induced an increase of local temperature between the electrodes. After the application of nsPEFs ceased, the delay of temperature decrease was several seconds, in the same order as that observed for infrared exposure. This time corresponded to the time necessary for the thermal exchanges with the external medium as temperature of the system returned to equilibrium with room temperature.

Important differences were observed in the measurement of temperature with the Luxtron probe, in comparison to the RhB method, specifically there was a delay between the time when RhB showed temperature changes and when the Luxtron detected changes in the extracellular volume between the electrodes. The difference was observed in the slope of the temperature increase reported by these two methods. The difference in the elevation of temperature can be explained by the fact that with the application of 10 pulses, the modification of temperature was very small. The results therefore show that the RhB temperature measurement had a better temporal resolution and better sensitivity for reporting changes in temperature at the cellular level than the external temperature probe. This was confirmed in experiments using pulse applications of 100 nsPEFs. In this case where a pulse repetition frequency of 10 Hz was used, the delay of the Luxtron probe was very evident. However at low pulse repetition frequencies, the increase in temperature registered by the Luxtron probe was similar to that measured at the cellular level with RhB. At a pulse repetition frequency of 100 Hz, the temporal resolution of the Luxtron probe was not sufficient to measure the temperature elevation before its dissipation. The external thermometer did not therefore represent the rate of change in temperature as observed at the cellular level with RhB fluorescence.

The influence of the amplitude of the nsPEFs was also studied in order to understand at which level of electric field temperature increases are observed. In this case, the delivery of 100 pulses with a frequency of 10 Hz was chosen. The duration of the pulses is still 10 ns. Temperature measurements with RhB and Luxtron thermometer were performed in this configuration, since the magnitude of the temperature change detected was approximately the same for both methods. The amplitude of the pulse was varied from 5.5 kV/cm to 44 kV/cm including 11, 17, 22, and 34 kV/cm. The results are shown in Fig. 9 . Figure 9(h) shows the relationship between the increase of temperature and the amplitude of the nsPEFs with error bars illustrating the +/–0.1 °C standard deviation.

#247362 Received 6 Aug 2015; revised 19 Sep 2015; accepted 22 Sep 2015; published 24 Sep 2015

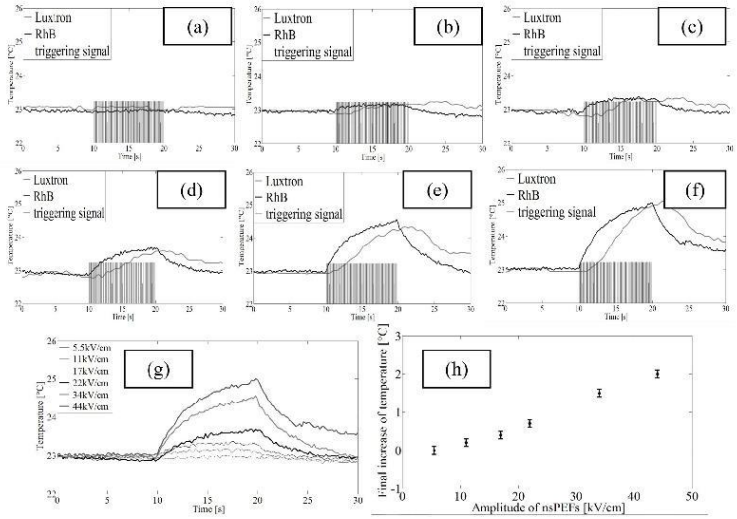

Fig. 9. The influence of pulse amplitude on temperature modifications induced by 100 x 10ns nsPEFs at 10 Hz, measured by RhB and Luxtron thermometer. (a). 5.5 kV/cm. (b). 11 kV/cm. (c). 17 kV/cm. (d). 22 kV/cm. (e). 34 kV/cm. (f). 44 kV/cm. (g). Superposition of RhB measurement curves. (h). The magnitude of the increase of temperature depending on the amplitude of the nsPEFs for an exposure to 100 pulses at 10 Hz.

The amplitude of the nsPEFs played a key role in the local increase of temperature induced by the pulse application. No increase of temperature was observable with the application of nsPEFs with an amplitude of 5.5 kV/cm with our thermal precision. At 11 kV/cm nsPEFs, a very small increase of temperature appeared of about 0.2 °C (+/–0.1°C) was detected. As one would expect, as pulse amplitude was increased, so did the change in temperature induced. Thus, with a fixed number of pulses at this frequency, the local increase of temperature was induced only if the amplitude of nsPEFs exceeded a certain threshold. With the thermal precision of +/–0.1°C accessible with our experiment, the threshold was therefore between 5.5 and 11 kV. This threshold would also be expected to decrease with longer pulse durations, however only pulses of 10 ns were considered in our experiments.

5. Conclusion

Among all the methods available for the microscopic measurement of temperature at the cellular level, RhB fluorescence is by far the simplest with respect to both the optical setup and ease of use for biologists. The temperature sensitivity of RhB, in particular the dependence of its quantum yield with regard to the temperature, has been used in many fluidic applications to make temperature measurement at the micron scale. In this paper, we developed a setup built around a wide field fluorescent microscope using epifluorescence detection to measure temperature in cells exposed to an infrared radiation at 805 nm and to nsPEFs. The thermal effect of each stimulus was demonstrated and it was shown that the increase of temperature induced depended on different parameters such as the average power, the duration of exposure the frequencies of repetition and their amplitude.

In these experiments, local temperature increases were demonstrated at the cellular level in samples exposed to 10 ns PEFs. The effect of nanosecond pulsed electric fields are assumed to be nonthermal, given their low average power and short duration. However, our

#247362 Received 6 Aug 2015; revised 19 Sep 2015; accepted 22 Sep 2015; published 24 Sep 2015

results suggest that temperature changes should be considered in their effects, particularly at higher electric fields, application frequencies and repetition rates.

This method is a first step in understanding some phenomena that are induced by heating biological tissues. The temporal resolution of the method was approximately 4 ms and the sensitivity allowed a detection of approximately 0.1°C change in temperature. This system now permits investigation of temperature modifications at the cellular level and can be combined with fluorescent physiological indicators that permit the measurement of intracellular calcium, plasma membrane potential and mitochondrial membrane potential. The method presented provides an excellent compromise between temporal resolution and sensitivity to measure the thermal impact of infrared radiation and nsPEFs at the cellular level to understand their mechanisms and advance their potential use in therapeutic applications.

Author Contributions

RO, DM and CL conceived of the experiments and wrote the manuscript. RO,CL and DM developed the infrared optical stimulation apparatus and RO, DM integrated it with the fluorescence imaging system. PL developed the nanosecond pulsed electric field application system performed FDTD simulations calculating the electric field. DM and RB performed temperature experiments with nsPEFs. DM, CL performed infrared heating experiments and analyzed data.

Acknowledgments

Research was funded through an ANR Labex Excellence Chair awarded to RO as part of Labex SigmaLim, funds from the Region Limousin and the CNRS. The BioEPIX laboratory at XLIM are part of the European Associated Laboratory (LEA) entitled "Pulsed Electric Fields Applications in Biology and Medicine".

#247362 Received 6 Aug 2015; revised 19 Sep 2015; accepted 22 Sep 2015; published 24 Sep 2015

Annex 3 Article published in Journal of Biophotonics

Infrared neural stimulation induces intracellular Ca^{2+} release mediated by phospholipase C

David Moreau[1], Claire Lefort[1], Jolien Pas[2], Sylvia M. Bardet[1], Philippe Leveque[1], and Rodney P. O'Connor[1,2]*

*Corresponding Author: E-mail: rodney.oconnor@emse.fr
[1] Univ. Limoges, CNRS, XLIM, UMR 7252, F-87000 Limoges, France.
[2] Current address : Bioelectronics Department, École Nationale Supérieure des Mines de Saint-Étienne, Centre Microélectronique de Provence - Georges Charpak Campus, 880 route de Mimet, 13541 Gardanne, France.

Keywords: Infrared neural stimulation, calcium imaging, phospholipase C, IP_3 signaling, photobiomodulation

The influence of infrared laser pulses on intracellular Ca^{2+} signaling was investigated in neural cell lines with fluorescent live cell imaging. The probe Fluo-4 was used to measure Ca^{2+} in HT22 mouse hippocampal neurons and non-electrically excitable U87 human glioblastoma cells exposed to 50-500 ms infrared pulses at 1470 nm. Fluorescence recordings of Fluo-4 demonstrated that infrared stimulation induced an instantaneous intracellular Ca^{2+} transient with similar dose-response characteristics in hippocampal neurons and glioblastoma cells (half-maximal effective energy density EC_{50} of around 58 $J.cm^{-2}$). For both type of cells, the source of the infrared-induced Ca^{2+} transients was found to originate from intracellular stores and to be mediated by phospholipase C and IP_3-induced Ca^{2+} release from the endoplasmic reticulum. The activation of phosphoinositide signaling by IR light is a new mechanism of interaction relevant to infrared neural stimulation that will also be widely applicable to non-excitable cell types. The prospect of infrared optostimulation of the PLC/IP_3 cell signaling cascade has many potential applications including the development of optoceutical therapeutics.

This article has been accepted for publication and undergone full peer review but has not been through the copyediting, typesetting, pagination and proofreading process, which may lead to differences between this version and the Version of Record. Please cite this article as doi: 10.1002/jbio.201700020

1. Introduction

Infrared neural stimulation (INS) has been successfully demonstrated in peripheral nerves [1-5] and the central nervous system.[6,7] The mechanism mediating INS is not fully understood. However, Wells and colleagues suggested that the effect was likely photothermal, given the absorption of infrared (IR) radiation by water at the wavelengths employed in INS experiments (1200-2100 nm).[8] Further, they excluded photochemical and photomechanical effects due to low energy of infrared photons and long pulse durations used, instead proposing that heat sensitive ion channels may be involved. By measuring changes in intracellular Ca^{2+} concentration, Rhee and colleagues showed that temperature-sensitive Transient Receptor Potential Vanilloid (TRPV) cation channel was implicated in these responses.[9] A further study by Albert et al., revealed a similar role for TRPV4 channels in INS experiments performed on primary sensory neurons.[10]

A different mechanism for INS was proposed by Shapiro and coworkers, where the fast heating due to infrared water absorption is suggested to directly influence membrane capacitance, inducing changes in the membrane potential and initiating the action potential.[11] They demonstrated that the infrared-induced current response tracked the rate of change in temperature and not the value of the temperature itself. For this capacitance effect, the general electrostatic mechanism proposed requires only the basic properties of the plasma membrane without the need for specialized temperature-sensitive ion channels. Electrophysiological evidence was presented demonstrating the change in capacitance in *Xenopus* oocytes, human embryonic kidney cells (HEK) and artificial lipid bilayers. However, a simulation study showed that the shift in membrane capacitance required to depolarize an axon would not likely be achieved using the parameters typically used in INS.[12] Furthermore, a recent in vitro study in acute mammalian brainstem slices highlighted the

possibility of evoking inward currents in individual neurons with low power densities, that would suggest that the fast temperature gradient is not necessarily needed [13].

Although recent INS investigations have primarily considered effects occurring at the level of the plasma membrane, there is also evidence that IR irradiation may impact cell excitability via intracellular effects. In cardiomyocytes, another type of excitable cell, IR exposure led to transient increases in intracellular Ca^{2+} that were determined to be of mitochondrial origin.[14] The authors made this conclusion as a pharmacological inhibitor of the mitochondrial Na^{+}/Ca^{2+} exchanger (CGP-37157) attenuated the IR response; however, in the same study, inhibitors of Ca^{2+} release from the endoplasmic reticulum (ER) (2-APB, ryanodine) had similar effects. Earlier studies of femtosecond pulsed IR (780 nm) performed on non-excitable cells also showed that intracellular Ca^{2+} stores were involved, thus Ca^{2+} release from the ER may be a common mechanism in cellular IR effects.[15,16]

A further mechanism for INS has recently been proposed by Beier implicating a thermal destabilization of phospholipids and transient permeabilization of the plasma membrane.[17] This was confirmed by observations of increased permeability of the plasma membrane of primary hippocampal neurons, NG108 neuroblastoma and Chinese hamster ovary (CHO) cells to Ca^{2+} ions, as well as, the influx of the small, cationic membrane impermeant fluorophore, YO-PRO1. Together these results suggest that infrared heating may disrupt phospholipids and cause the transient formation of nanometer diameter pores. Depletion of phosphatidylinositol 4,5-bisphosphate (PIP_2) from the plasma membrane was also observed following IR pulses, as reported by translocation of the fluorescence protein sensor PLCδ-PH-EGFP. Although these results were interpreted as thermal destabilization of phospholipids, it could also be evidence of stimulation of phosphoinositide signaling by INS, as discussed by the authors.

There are a number of means by which infrared induced phosphoinositide signaling might impact cell excitability and lead to neural stimulation. Intracellular Ca^{2+} is a universal signal responsible for controlling numerous cellular processes in both excitable and non-excitable

cells.[18] Extracellular signals from neurotransmitters, hormones or growth factors induce intracellular Ca^{2+} signals through their stimulation of Gq protein-coupled receptors and activation of the enzyme phospholipase C (PLC) to hydrolyze phosphatidylinositol 4,5-bisphosphate ($PI(4,5)P_2$) in the plasma membrane. The cleavage $PI(4,5)P_2$ in the membrane by PLC releases the second messenger inositol 1,4,5-trisphosphate (IP_3) into the cytosol and causes Ca^{2+} release from stores via IP_3-gated Ca^{2+} channels located on the membrane of the ER. [18- 20]. In addition to initiating signals, ER Ca^{2+} stores play a significant role shaping cytosolic transients in neurons and can modulate cell excitability and influence synaptic plasticity.[21,22] Intracellular Ca^{2+} release or extracellular Ca^{2+} entry tunes the further release of Ca^{2+} from IP_3 and ryanodine receptor (RyR) releasable stores in the SR/ER, resulting in signal amplification by Ca^{2+}-induced Ca^{2+} release [23]. Other effects of PLC activation include depletion of $PI(4,5)P_2$ at the plasma membrane and the modulation of ion channel gating leading to enhanced excitability and action potentials, or hyperpolarization and quiescence, depending on the cell type.[24-27]

In this paper, we investigated the hypothesis that infrared stimulation may activate phosphoinositide-signaling pathways via phospholipase C leading to IP_3-induced intracellular Ca^{2+} transients. Fluorescent live-cell Ca^{2+} imaging was used to compare the responses of electrically excitable mouse hippocampal neurons (HT22) and human glioblastoma cells (U87) to 1470 nm IR laser pulses lasting from 50 to 500 milliseconds. Pharmacological manipulations were used to determine the source of the intracellular Ca^{2+} transients and to test whether phospholipase C and IP_3-induced Ca^{2+} release from intracellular stores were involved in these INS responses.

2. Material and methods

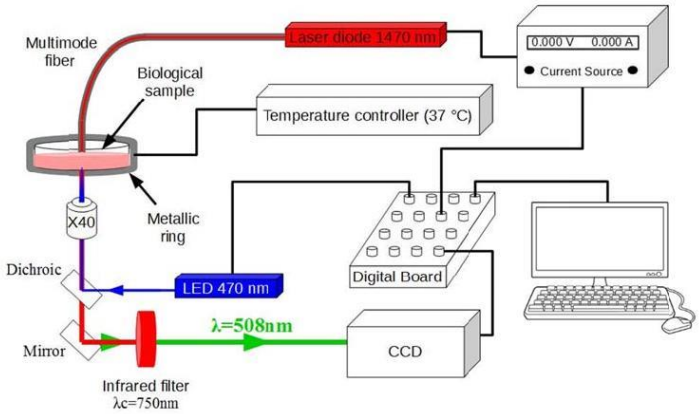

Figure 1. Experimental setup

Figure 1 shows the experimental setup used to expose cells to infrared radiation at physiological temperatures. Cells were maintained at 37 °C using a resistive heating element and temperature controller (TC-E35, Bioscience Tools). The temperature was also measured by a calibrated fiber optic thermometer as 37 °C +/-1 (LUXTRON 812 Industrial Temperature Monitor).

2.1. Fluo-4 AM loading

At the start of imaging experiments, cell culture growth medium was replaced with a modified Tyrode's solution, hereafter known as HEPES Buffered Salt Solution (HBSS), consisting of 121 mM NaCl, 5.6 mM KCl, 1.7 mM $MgCl_2$, 6 mM $NaHCO_3$, 12.5 mM glucose, 2.3 mM $CaCl_2$ and 25 mM HEPES. The pH was adjusted to 7.3 with NaOH. HT22 immortalized mouse hippocampal neurons [28] (The Salk Institute, La Jolla, CA) and U87 human glioblastoma cells (ECACC, Public Health England, 89081402) were used as examples of excitable and non-excitable cells, respectively. Cells were loaded for 45 min with 2 µM Fluo-4 AM and then washed twice with fresh HBSS before microfluorimetry imaging experiments

commenced. The relative change in cytosolic Fluo-4 fluorescence ($\Delta F/F_0$) was used to monitor intracellular Ca^{2+} response to IR stimulation.

2.2. Infrared exposure system and intracellular Ca^{2+} imaging

A multimode laser diode (LU1470T015, Lumics) with a fibered output (core diameter 105 µm, numerical aperture 0.15) emitting at 1470 nm was used as the infrared source. The diode laser temperature was stabilized with a cooling block (LU_CB_T_0, Lumics) and the power supply (LU_DR_AD, Lumics) allowed control of both the exposure time and the power of the infrared light. The exposure parameters were externally controlled with freely available software (Winfluor, Strathclyde University), that allowed the synchronization of the IR exposure with the fluorescence measures of intracellular Ca^{2+}. The output of the fiber was precisely placed 500 µm above the cells with a micromanipulator. The area illuminated at the bottom of the petri dish where cells were attached was calculated using the numerical aperture of the fiber, the refractive index of water, and the distance between the fiber tip and the cells. We then divided the total energy delivered by the area illuminated, by taking into account the high absorption of the infrared exposure by water. Thus, with a distance between the fiber tip and the cells of 500 µm, and with an absorption coefficient of about 28 cm^{-1} for 1470 nm radiation [29], we expect that cells were actually exposed to about the quarter of the energy density calculated with the area illuminated. The rest of the energy would be absorbed by water and converted into heat.

An inverted wide field epifluorescence microscope was used (Olympus IX70) to measure Fluo-4 AM fluorescence intensity. A light emitting diode (LED) (4-Wavelength High-Power LED Source, Thorlabs) was used for excitation of the Fluo-4 (λ_{exc}=470 nm). An average power of 1 mW of excitation light was delivered and focused on the cells under investigation using a 40X microscope objective (Olympus, NA 0.6). The fluorescence emission (λ_{em}=516

nm) of Fluo-4 was collected through the dichroic mirror and detected with a CCD camera (14 bit, pixel matrix 512x512, iXon, AndorTM Technologies). It should be noted that the fluorescence light was isolated from the infrared light with a shortpass filter (λc=750 nm) placed before the CCD. The parameters of the infrared exposure (duration and power), those of acquisition of the CCD, and those of the LED emission were controlled by Winfluor and by an analog output from a digital acquisition (DAQ) board (USB-6229-BNC, National Instruments).

2.3. Temperature measurement with Rhodamine B

Rhodamine B (RhB) is a fluorescent dye that has fluorescence emission intensity that is dependent on temperature. We have recently demonstrated the possibility to use this property to measure temperature with 0.1 °C precision at the single cell level [30]. Following this established method, cells were incubated with 50 µM RhB in HBSS for two hours to load the dye and then washed twice with fresh HBSS. A step of calibration (data not shown) revealed that RhB fluorescence decreased linearly with temperature from 37 °C, with a decrease of about 2.4 %/°C. Thus the measure of the change of the RhB fluorescence intensity allowed the measure of the change of temperature in cells.

2.4. Extracellular electrophysiological recordings

Extracellular electrophysiological recordings were performed with custom microelectrode arrays (MEAs). The MEAs consisted of 64 gold electrodes deposited on glass and spin-coated with poly(3,4-ethylenedioxythiophene) doped with poly(styrenesulfonate) (PEDOT:PSS), a conducting polymer with high conductivity. Parylene-C[poly(para-chloroxylylene)] was used as insulating material because of its moisture, chemical and dielectric barrier properties [31].

Electrical recordings were acquired with a multi-channel amplifier system (RHD2000 series, Intan technologies) with digital output via USB interface, allowing electrophysiological signals to be sampled at a rate of 35 kHz. Data were then notch filtered (50 Hz) and processed by threshold detection to identify neuronal spikes induced by the infrared exposure and to extract the spike rate.

2.5. Pharmacological reagents and cell media preparations

The inhibitor of phospholipase C, U73122 (10 μM), or its inactive analog, U73343 (10 μM), and the IP_3-channel inhibitor, 2-Aminoethoxydiphenylborane (2-APB, 1 mM) were each diluted in 2 mL HBSS. In some cases, $CaCl_2$ was omitted from the HBSS and replaced by the chelator EGTA (4 mM) to yield Ca^{2+} free medium. Cells were pre-incubated with pharmacological inhibitors for 10 min before experiments and during fluorescence recordings. The sarco/endoplasmic reticulum Ca^{2+}-ATPase pump (SERCA) inhibitor, thapsigargin (2 μM), was diluted in HBSS prepared without $CaCl_2$ and with EGTA (4 mM), and cells were incubated in that solution for 20 min to deplete the internal ER Ca^{2+} stores. YO-PRO1 was diluted in HBSS (1 μM), and it was added at the start of imaging experiments without pre-incubation. In experiments testing whether IR stimulation caused membrane permeabilization, YO-PRO1 fluorescence was measured following IR exposure or digitonin was added in place of IR stimulation at a final working concentration of 100 μM as a positive confirmation that YO-PRO1 indeed reported membrane permeabilization.

2.6. Image analysis and statistics

Fluorescence images were processed offline with Winfluor software to manually select the region of interest of cells and extract the fluorescence over time. Raw fluorescence traces

were exported into Matlab (Mathworks, MA). Relative changes in fluorescence ($\Delta F/F_0$) were computed from Fluo-4 signals to reflect changes in intracellular Ca^{2+} as $(F-F_0)/F_0$, where F was the fluorescence at each time point and F_0 was the fluorescence at the baseline before addition of the stimulus. At least 9-10 experiments were performed on naïve cells per treatment condition and observations expressed as the mean fluorescence +/- the standard deviation (SD) of the mean. Independent t-tests were performed with Matlab on the peak $\Delta F/F_0$ following IR stimulation and considered statistically significant when the probability of falsely rejecting the null hypothesis was less than 0.1% ($p<0.001$). Multiple comparison statistics were adjusted by Bonferroni correction.

3. Measurement of intracellular Ca^{2+} by Fluo-4 in cells exposed to infrared laser pulses

3.1. Dosimetry

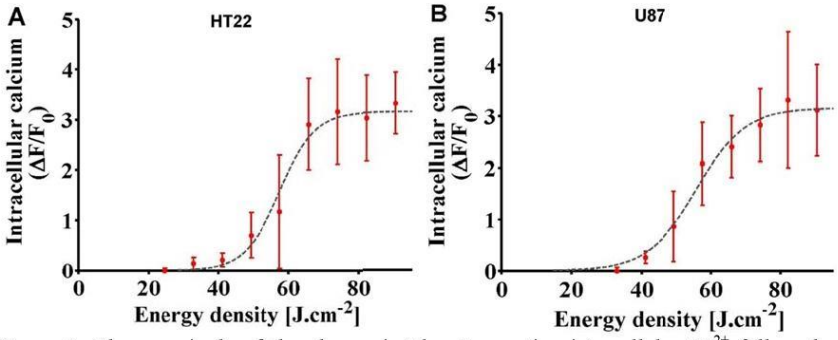

Figure 2. The magnitude of the change in Fluo-4 reporting intracellular Ca^{2+} followed a sigmoidal dose-response relationship with the infrared energy density delivered to the cells. Infrared exposure lasted for a duration of 500 ms. **A**. HT22 neurons. **B**. U87 cells.

3.1.1. HT22 mouse hippocampal neurons

All results are presented as the mean fluorescence of 10 independent recordings of different cells with their associated standard deviation. IR exposure caused a statistically significant change in intracellular Ca^{2+} in HT22 cells that was dose dependent. **Figure 2.A** shows the

dependency of the change in Fluo-4 signal on the energy density delivered during 500 ms exposures to HT22 mouse hippocampal neurons. For exposures of fixed length at 500 ms, as the IR power and delivered energy was increased, intracellular Ca^{2+} increased, given the change in Fluo-4 fluorescence intensity. Nine different infrared powers were tested between 75 mW and 275 mW with a constant step of 25 mW. In our experimental setup, these powers corresponded to energy densities from about 24.7 $J.cm^{-2}$ to 90.4 $J.cm^{-2}$. The intracellular Ca^{2+} response was therefore observable with our setup after an approximate threshold of about 33 $J.cm^{-2}$. The maximal change in intracellular Ca^{2+} observed following IR stimulation corresponded to a ~3.5 fold increase in fluorescence for energy densities of 74 $J.cm^{-2}$ and above. The half-maximal effective energy density (EC_{50}) was approximately 58 $J.cm^{-2}$.

3.1.2. Temperature measurement

Temperature measurements with Rhodamine B were performed in HT22 mouse hippocampal neurons exposed to infrared radiation. The temperature change caused by infrared exposure at the cellular level was investigated for each of the energy densities used in previous experiments with a duration of 500 ms. An image of RhB fluorescence was taken every 50 ms representing the temporal resolution of the temperature measurement. **Figure 3** shows the temperature changes according to the energy density delivered to the cell. Each curve represents the average of nine different recordings on nine different cells.

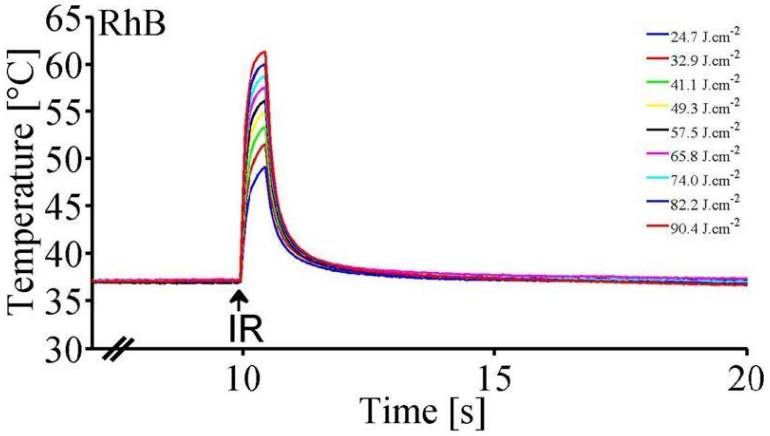

Figure 3. Temperature measurement with RhB in HT22 mouse hippocampal neurons exposed to infrared for 500 ms.

Table 1 reports the temperature reached and the change of temperature (ΔT) for each energy density used.

Table 1. Temperature reached and temperature changes in HT22 mouse hippocampal neurons exposed to infrared during 500 ms in function with the energy density.

Energy density (J.cm^{-2})	Temperature reached (°C)	ΔT (°C)
24.7	49.2	12.2
32.9	51.6	14.6
41.1	53.4	16.4
49.3	54.9	17.9
57.5	56.1	19.1
65.8	57.6	20.6
74.0	58.7	22.7
82.2	60.0	23.0
90.4	61.4	24.4

The high temperature rises induced by 500 ms infrared exposures caused concern about potential cell damage. Thus, exposure of a HT22 mouse hippocampal neuron to two infrared exposures with both duration of 500 ms was performed, to see if full reversibility was obtained. The energy density used was 82.2 J.cm^{-2} corresponding to a temperature rise of

23 °C. The second infrared exposure was made after the intracellular Ca^{2+} concentration returned to the basal value. As a result, see **Figure 4**, both infrared exposures induced Ca^{2+} transients probed with Fluo4. This reversibility demonstrated that the increase in intracellular calcium concentration was not permanent or dysregulated like that observed in damage-induced responses, which reassures that these stimuli do not cause adverse effects on cells in the short-term.

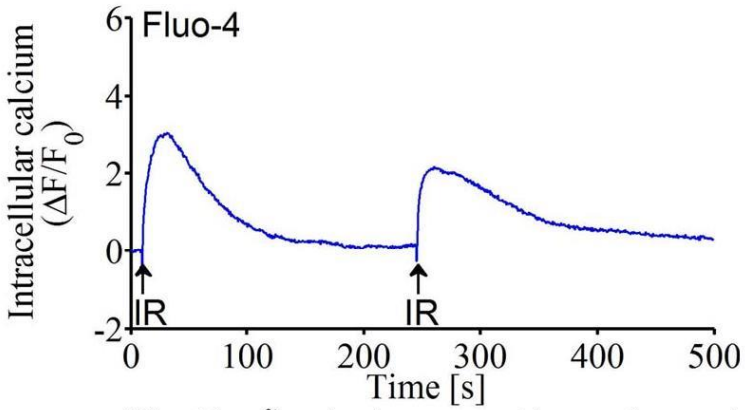

Figure 4. Reversibility of the Ca^{2+} transients in HT22 mouse hippocampal neurons triggered by infrared exposure.

3.1.3. U87 human glioblastoma cells

Figure 2.B shows that in U87 human glioblastoma cells, the intracellular Ca^{2+} and corresponding change in Fluo-4 fluorescence depended on the applied energy density delivered in 500 ms IR exposures. The Ca^{2+} response of these cells followed a sigmoidal dose-response with respect to the density of infrared energy delivered to these cells. The threshold of the U87 Fluo-4 response to IR stimulation was observable with our setup from about 41 $J.cm^{-2}$. The maximal change in intracellular Ca^{2+} was observed as a ~3.5 fold increase in Fluo-4 at an energy density of 82.2 $J.cm^{-2}$ and above. The EC_{50} for U87 cells was around 56 $J.cm^{-2}$.

Comparing the IR dosimetry experiments on HT22 and U87 cells shown in Figure 2.A and 2.B, we see very similar dose-dependence on the energy density for the Ca^{2+} response following the infrared exposure. The EC_{50} for the two cell types were very close (56 $J.cm^{-2}$ for U87 cells against 58 $J.cm^{-2}$ for HT22 neurons), and the maximal changes in fluorescence amplitude were in the same range (~3.5-4 fold).

3.2. Influence of the duration of infrared exposures on the intracellular Fluo-4 signal

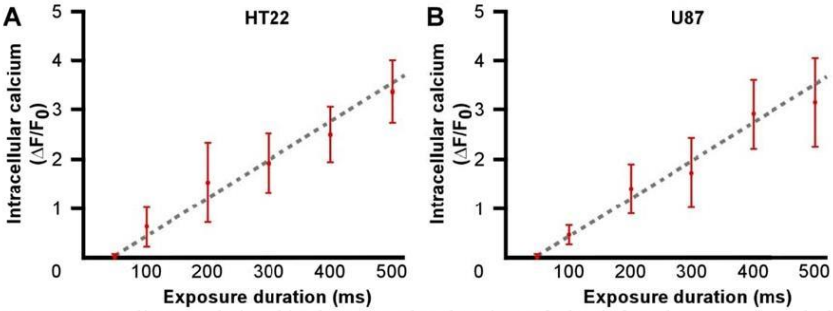

Figure 5. A linear relationship between the duration of the infrared exposure and the amplitude of the Ca^{2+} response in excitable and non-excitable cells. **A**. HT22 hippocampal neurons. **B**. U87 human glioblastoma cells.

3.2.1. HT22 mouse hippocampal neurons

Results of experiments varying IR exposure duration are presented as the mean of 10 independent recordings and their associated standard deviation. **Figure 5.A** shows the relationship between infrared exposure duration and the change in intracellular Ca^{2+} in HT22 mouse hippocampal neurons. Here the power at the output of the fiber was maintained at 275 mW, the highest power used in the previous study. When the duration of the infrared exposure was increased, the peak change in Fluo-4 fluorescence and thus the intracellular Ca^{2+} response increased. The relationship between the duration of the IR exposure and the magnitude of the change in intracellular Ca^{2+} was linear over the range of durations tested. The change in Fluo-

4 signal and Ca^{2+} response was observable with our setup with exposure durations greater than 100 ms.

3.2.2. U87 human glioblastoma cells

Figure 5.B shows the dependence of the intracellular Ca^{2+} response in U87 glioblastoma cells on the duration of the infrared exposure. In these experiments, the power at the output of the fiber was maintained at 275 mW. As with the dosimetry study, we observed that the change in Fluo-4 in HT22 neurons and U87 human glioblastoma cells had similar dependencies on IR exposure duration. The Ca^{2+} responses followed a linear trend with respect to IR exposure duration and appeared after exposure durations of 100 ms at 275 mW of incident power.

3.3. Pharmacological dissection of the IR induced Ca^{2+} signals in HT22 and U87 cells

Following the previous experiments, we chose to fix the infrared exposure duration at 500 ms to pharmacologically dissect the source of the Ca^{2+} signals in these robust IR responses. Infrared power was maintained at 275 mW (energy density of 90.4 $J.cm^{-2}$). Experiments were also performed at this energy density to determine whether IR exposure caused permeabilization of the plasma membrane.

3.3.1. Infrared exposure of HT22 mouse hippocampal neurons induces intracellular Ca^{2+} release from internal stores mediated by PLC activation

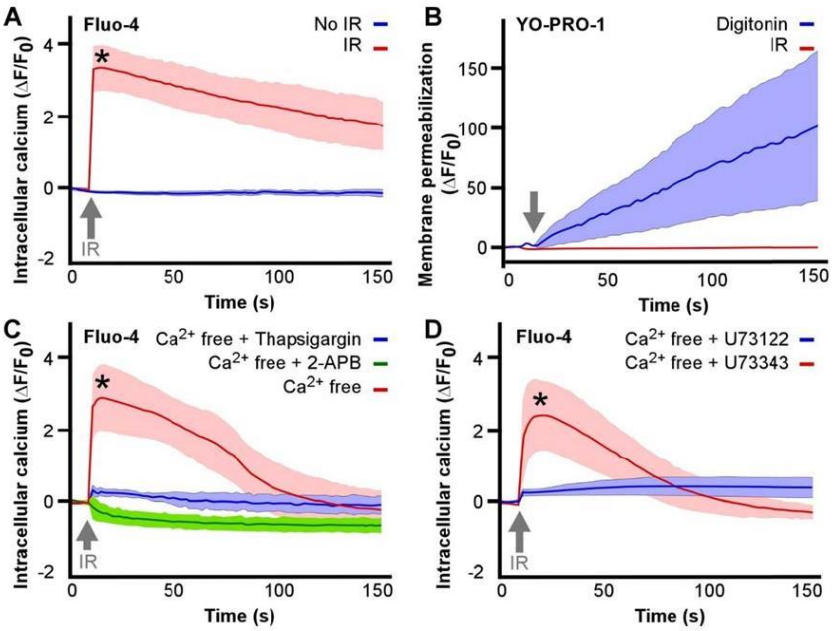

Figure 6. Infrared stimulation of hippocampal neurons leads to an increase in Ca^{2+} release from ER stores. The source of the IR-induced Ca^{2+} signal in mouse HT22 hippocampal was dissected pharmacologically. **A**. A statistically significant change in Fluo-4 signal was observed in HT22 cells (n=10) receiving a 500 ms IR exposure when compared to control experiments without infrared exposure (n=10, t=15.74, p=7.24e-08). **B**. No change in YO-PRO1 fluorescence was observed in cells exposed to infrared radiation (n=10), control experiments using digitonin to permeabilize the plasma membrane showed significant uptake of YO-PRO1 (n=9, t=-4.56, p=1.85e-03). C. The infrared-induced Ca^{2+} response was due to Ca^{2+} release from the ER and not due to entry, as it persisted in Ca^{2+} free media (n=10), but not with store depletion by thapsigargin (n=10) or inhibition of IP_3 receptors with 2-APB (n=10) (1 mM). **D**. Inhibition of PLC by U73122 (10 μM)(n=10) prevented the IR-induced Ca^{2+} response (t=6.54, p=9.01e-05), whereas incubation of cells with the inactive analog, U73343 (10 μM), had no effect (n=10). Asterisks indicate statistical significance at * p<0.001.

The application of a single 500 ms infrared exposure to HT22 neurons (n=10) caused a strong and statistically significant (t=15.74, p=7.24e-08) increase in Fluo-4 indicating an increase in intracellular Ca^{2+} (**Figure 6.A**). The control experiments (n=10), where fluorescence was recorded without the IR exposure showed no photobleaching or spontaneous signals. YO-PRO1 was used to determine whether IR exposure caused permeabilization as previously

reported by Beier et al.[17]. YO-PRO1 is a cell impermeable dye whose fluorescence intensity increases upon entry to the cell and contact to nucleic acids. Thus, membrane permeabilization was investigated by the measurement of YO-PRO1 fluorescence and the resulting presence or not of a change in the fluorescence intensity. No increase in YO-PRO1 was observed in cells (n=10) following the IR exposures (**Figure 6.B**). However, when the plasma membrane permeabilization agent digitonin was added as a positive control (n=9), a statistically significant increase in YO-PRO1 fluorescence was indeed observed (t=-4.56, p=1.85e-03). The energy delivered during infrared exposure for 500 ms at 1470 nm caused an increase in intracellular Ca^{2+}, but was not sufficient to create pressure waves or cause heating that led to observable permeabilization of the plasma membrane.

The origin of the IR-induced intracellular Ca^{2+} transient measured by Fluo-4 in HT22 neurons was investigated by pharmacological inhibitors and ion substitution. Initial experiments were performed to determine whether the IR-induced Ca^{2+} signal was due to Ca^{2+} entry from the extracellular media or release from intracellular organelles. When experiments were performed in HBSS media without Ca^{2+} ions (n=10) and substituted with EGTA to chelate any residual Ca^{2+} in solutions, the IR response was still observed (**Figure 6.C**). In the presence of extracellular Ca^{2+}, the kinetics of the Fluo-4 signal showed a sustained tail, suggestive of Ca^{2+} entry following release (Figure 4.A vs. Figure 4.C); however, extracellular Ca^{2+} was not necessary for the IR induced response. This indicated that the effect was likely due to Ca^{2+} release from intracellular organelles. Depletion of ER Ca^{2+} stores by preincubation of cells for 20 min in Ca^{2+} free media containing the SERCA pump inhibitor thapsigargin (2 μM) prevented the IR-induced increase in Fluo-4 signal (n=10, t=8.34, p=4.96e-05). Further experiments were performed in the presence of 2-APB (1 mM), an inhibitor of IP_3 channels and Ca^{2+} release from the ER. In this case, the IR exposure did not produce an increase in Fluo-4 (Figure 4.C), confirming the response was due to Ca^{2+} release from the ER.

Next, we performed experiments to determine the mechanism of the IR-induced IP_3 stimulated Ca^{2+} release from intracellular stores. Normally, IP_3 acts as a cytosolic second messenger to cause Ca^{2+} release from the ER following ligand binding to Gq protein receptors that activate PLC. The activity of PLC in this signaling cascade can be blocked by the specific inhibitor, U73122, which prevents the hydrolysis of $PI(4,5)P_2$ to IP_3. Experiments were carried out on HT22 cells in the presence of 10 μM of U73122 (n=10) and demonstrated that inhibiting the activity of PLC significantly blocked the IR induced Ca^{2+} release (**Figure 6.D**). Negative control experiments were also performed using the inactive analog, U73343, which had no effect on the IR-induced Fluo-4 signal, showing the necessity and specificity of the PLC in the IR response. Together, these results confirmed that infrared stimulation caused the release of Ca^{2+} ions from the intracellular stores by activating PLC and the IP_3 signaling pathway.

In the studies found in the published literature about infrared neural stimulation, typical infrared exposures used pulses operating within the thermal confinement regime. Thus, we investigated whether we observed similar Ca^{2+} responses with shorter pulses in the thermal confinement regime. This condition is when the duration of the infrared exposures t_p respects the relationship, $t_p \leq \delta^2/4\kappa$ [32,33], where δ is the smallest dimension of heated volume and κ the thermal diffusivity of water, $\kappa \approx 1.3 \times 10^{-3}$ cm^2/s. With our setup, the smallest dimension of the heated volume was the fiber core radius. This gives a maximum laser exposure duration of about 5 ms to respect thermal confinement. We thus applied a single 4 ms infrared exposure, with the optical fiber tip placed at 200 μm above the cells, corresponding to a delivered energy density of 10.4 $J.cm^{-2}$. **Figure 7** shows that the application of short exposures resulted in a similar Ca^{2+} response, in terms of latency and strength, when compared with 500 ms exposures, operating in the non-confinement regime. Thus, in our experiments, thermal confinement does not appear to be necessary to trigger HT22 mouse hippocampal neuronal function.

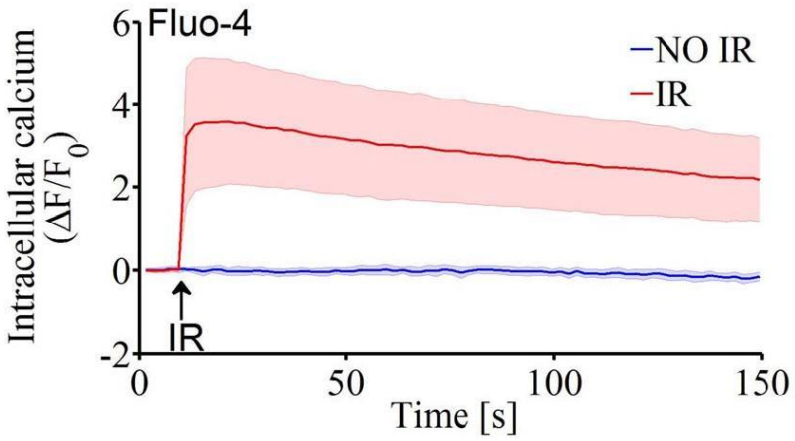

Figure 7 Infrared stimulation of hippocampal neurons leads to an increase in Ca^{2+} release from ER stores. A significant change in Fluo-4 signal was observed in HT22 cells (n=9) receiving a 4 ms IR exposure when compared to control experiments without infrared exposure.

Another way to verify that infrared pulses stimulate HT22 mouse hippocampal neuronal function is to electrically probe the changes in membrane depolarization associated with action potentials with extracellular electrophysiology. Recordings were made using custom microelectrodes arrays (MEAs), to show whether action potentials, or extracellular spikes, followed 4 ms infrared exposure in these cells. Infrared exposure was associated with strong, slow electrical artifact (see **Figure 8.A**). Thus, to minimize these artifacts the energy density delivered was divided by a factor of 2. **Figure 8.B** shows the presence or not of spikes and their timing and rate induced by multiple 4 ms infrared exposures with an energy density delivered of 5.2 $J.cm^{-2}$ per exposure. The reversibility and reproducibility was also shown by the repeated exposures at 0.05 Hz. It should be noted that the IR induced artifacts could be removed by digital filtering, like commonly seen in optogenetics.

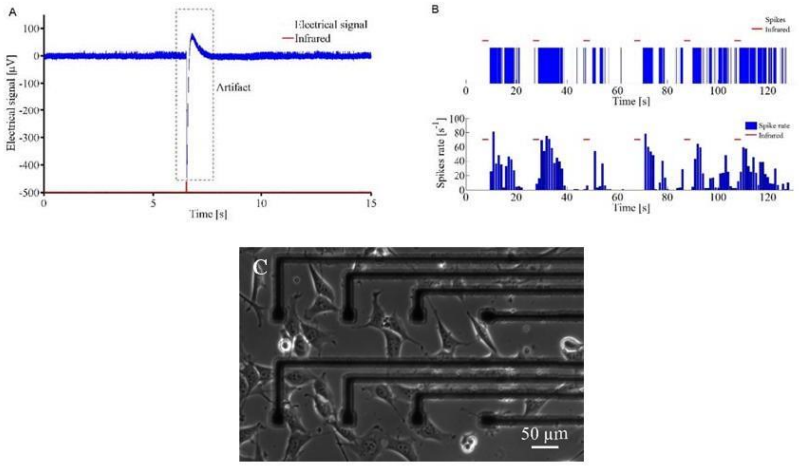

Figure 8. Infrared exposure of HT22 mouse hippocampal neurons leads to triggering of electrical spikes from these neurons. **A**. Exposure to 5.2 J.cm^{-2} infrared radiation during 4 ms induced an artifact in the recorded signal. **B**. Filtered and threshold detection processed data showing spike timing following repeated exposure to 5.2 J.cm^{-2} infrared radiation at 4 ms, operating in the confinement regime. **C**. Custom microelectrodes array used to perform extracellular electrophysiology.

3.3.2. Infrared exposure induces intracellular Ca^{2+} release from internal stores mediated by PLC activation in U87 human glioblastoma cells

Experiments were next performed on the U87 human glioblastoma cell line to determine whether the IR-induced PLC mediated Ca^{2+} responses were also observable in non-excitable cells of neural origin. **Figure 9** shows the results of pharmacological experiments on U87 cells carried out to probe the mechanism of the IR-induced Ca^{2+}. As with HT22 cells, the traces on each graph represent the mean change in fluorescence +/- SD of 10 independent experiments.

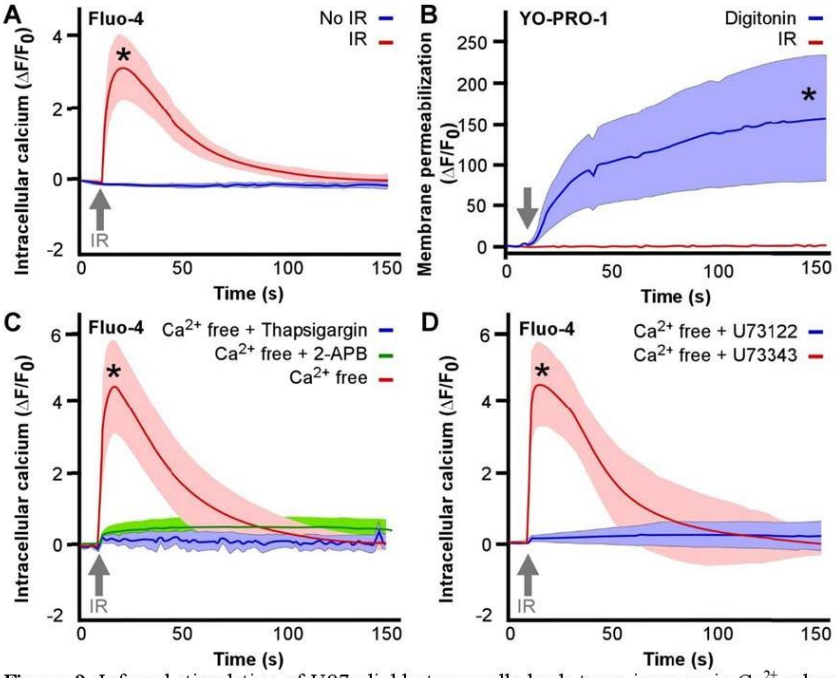

Figure 9. Infrared stimulation of U87 glioblastoma cells leads to an increase in Ca^{2+} release from ER stores The IR-induced Ca^{2+} signal was dissected pharmacologically in U87 cell. **A**. A statistically significant change in Fluo-4 signal was observed in U87 cells receiving a 500 ms IR exposure when compared to control experiments without infrared exposure (t= 11.59, p=9.90e-07). **B**. No change in YO-PRO1 fluorescence was observed in U87 cells exposed to infrared radiation, control experiments using digitonin to permeabilize the plasma membrane showed significant uptake of YO-PRO1 (t=-5.70, p=4.51e-04). **C**. The infrared-induced Ca^{2+} response was due to Ca^{2+} release from the ER and not due to entry, as it persisted in Ca^{2+} free media, but not with store depletion by thapsigargin or inhibition of IP_3 receptors with 2-APB (1 mM). **D**. Inhibition of PLC by U73122 (10 μM) prevented the IR-induced Ca^{2+} response in U87 cells (t=-11.36, p=9.45e-07), whereas incubation with the inactive analog, U73343 (10 μM), had no effect. Traces represent the mean +/- SD of 10 individual cells. Asterisks indicate statistical significance at * p<0.001.

The application of infrared exposures to U87 glioblastoma cells caused a significant increase in intracellular Ca^{2+}, as measured by Fluo-4 (**Figure 9.A**) (t=11.59, p=9.90e-07). The same experimental approach used with HT22 neurons was performed on U87 human glioblastoma cells. The plasma membrane of U87 cells was not disrupted by 500 ms IR exposures at 275 mW, as measured by YO-PRO1 uptake (**Figure 9.B**). As with HT22 neurons, the IR-induced

Ca^{2+} response in U87 cells persisted in Ca^{2+} free media (with EGTA), was inhibited by store depletion by thapsigargin, or block of IP_3 channels with 2-APB (**Figure 9.C**). Similar results were obtained after incubating U87 cells with U73122 (**Figure 9.D**), showing that inhibition of PLC activity significantly abrogated the IR-induced Ca^{2+} response (t=-11.36, p=9.45e-07). Infrared exposure of non-excitable cells therefore also caused release of Ca^{2+} from the ER, mediated by the PLC/IP_3 signaling cascade.

4. Discussion and conclusion

Despite the numerous studies investigating infrared neural stimulation, several hypotheses are still under consideration regarding the primary mechanism(s). In comparison to the two prominent hypotheses involving TRPV channels [9], or direct permeabilization of the plasma membrane [17], our results show that IR exposure causes an intracellular Ca^{2+} response without the necessity of extracellular Ca^{2+}entry. Under physiological conditions, Ca^{2+} entry would also occur and thermal gating of TRPV1, TRPV4 or other cation channels may further amplify the IR effect and increase the probability of action potentials. However, in the case of the IR-induced intracellular Ca^{2+} responses observed in HT22 hippocampal neurons or U87 glioblastoma cells, Ca^{2+} entry was not required for these intracellular responses.

The pharmacological experiments performed in this study lead us to conclude that infrared radiation induces activation of the PLC/IP_3 pathway and subsequent release of Ca^{2+} ions from the ER. This IR response would be commensurate with the depletion of $PI(4,5)P_2$ observed by Beier et al [17], showing translocation of the fluorescence protein sensor PLCδ-PH-EGFP. However, in our experiments membrane permeabilization was not observed, nor necessary, given that the response occurred in the absence of extracellular Ca^{2+}. We propose instead that the thermal activation of phosphoinositide signaling might be similar to that reported in the heat shock studies of PLC activation carried out by Calderwood et al.[34] In this case,

increases in temperature were shown to activate PLC and lead to the hydrolysis of $PI(4,5)P_2$ by thermal activation of the Gq class of G-proteins coupled to the PLC. Tseeb and colleagues [35] showed a similar effect of heat pulses on HeLa cells. Here heat pulses were produced by a focused infrared laser beam on metal nanoparticles. As a result, Ca^{2+} transients were triggered by heat pulses and attributed to a release of Ca^{2+} ions from the ER through IP_3 receptors. It remains to be determined whether thermally-induced IR effects act directly on the activity of PLC-PI hydrolysis, as in pure enzyme assays [36], or that they require GTP and Gq protein interactions [34].

Even if the duration of brief exposures were too short to measure the temperature in an accurate way with Rhodamine B and our setup, the same mechanism could be expected following the application to 4 ms exposures. It is certain that the delivered energy density would be smaller, but two other parameters should be considered in the temperature increase: the distance between the fiber tip and the cells, and the infrared power used during the exposure. The fiber tip was closer to the cells for 4 ms exposures (200 µm) than for 500 ms exposures (500 µm), and the infrared power was set to be higher (810 mW) during 4 ms exposures than for 500 ms exposures (275 mW). The smaller duration of the 4 ms exposures made the density of energy smaller even with higher infrared power. This change in the power induced a higher temperature gradient for 4 ms exposures than for 500 ms exposures. Furthermore, the temperature increase is expected to be higher at a distance of 200 µm of the fiber tip than at 500 µm. Thus, with the contribution of the higher temperature gradient induced by the higher infrared power used and of the smallest distance between the energy source (fiber tip) and the targeted cells, it is conceivable to think that the temperature change would be sufficient to cause PLC activation by transient heat shock.

The previously reported involvement of TRPV1 and TRPV4 channels in infrared neural stimulation would also be expected following the thermal activation of PLC in the plasma membrane. It has been shown that $PI(4,5)P_2$ binds to TRPV1 and TRPV4 channels

modulating their gating behavior.[24,25,37] The rapid depletion of $PI(4,5)P_2$, following thermal PLC activation by infrared pulses, might therefore modulate TRPV activity, and would be attenuated by Ruthenium red or specific TRP inhibitors, depending on their expression in the cell type evaluated. The potential influence of thermal $PI(4,5)P_2$ depletion on cell excitability through M-type KCNQ potassium channels has also been discussed by Beier et al. [17] In addition to these effects, thermally-induced PLC hydrolysis of $PI(4,5)P_2$ would also be expected to generate 1,2-diacylglycerol (DAG) signals in the plasma membrane. Other effects on channel gating might therefore be predicted through DAG mediated protein kinase C effects [38,39] or arachidonic acid stimulation of TRPV4 activity [40]. Future studies should investigate the involvement of these parallel phosphoinositide-signaling pathways in the plasma membrane, which one would expect to be quicker than cytosolic Ca^{2+} release, which requires diffusion of the second messenger IP_3 to the ER.

Infrared-induced thermal effects on membrane capacitance were clearly observed by Shapiro et al.[11], yet it would be difficult to reconcile how such changes in capacitance might activate PLC and IP_3-induced Ca^{2+} release, as observed in our experiments. On the other hand, Xu and Loew demonstrated that PLC activation in neuroblastoma cells by Gq agonists led to an increase in intramembrane potential, as the membrane lost negative charges via $PI(4,5)P_2$ hydrolysis, and the dipole potential increased with hydrolysis of PIP_2 to DAG.[41] PLC inhibitors were shown to block these changes in intramembrane potential associated with $PI(4,5)P_2$ hydrolysis, which were demonstrated to account for a depolarization of the intramembrane potential by up to ~83 mV. These measured changes in intramembrane potential (comprising the transmembrane potential, the difference between internal and external surface potential, and the internal and external dipole potential) caused by PLC hydrolysis are significant. If infrared stimulation activates PLC, either directly or via Gq-protein coupling, shifts in membrane capacitance might be expected given the dramatic change in surface potential and dipole potential of the membrane with the redistribution of

PIP_2 hydrolysis. The voltage-sensitive dye imaging approach used by Loew [41] may therefore be useful for studying whether shifts in the surface and dipole potential of the membrane changes following IR stimulation, as they are not measurable by electrode techniques.

The durations of infrared exposures used in our experiments were approximately a factor of 10-15 longer than those typically used in INS studies, however, the energy densities were similar. The coupling efficiency of IR stimulation can therefore be improved by using wavelengths closer to the peak absorption of water, or by strategies including the addition of gold nanoparticles near the plasmonic resonances of lower wavelengths to enhance focal heating.[42,43] Even though the length of IR exposure used in our experiments favored the measurement of slower PLC/IP_3 mediated intracellular Ca^{2+} transients, $PI(4,5)P_2$ effects at the plasma membrane modulating the gating of ion channels would be expected to be much faster. Further studies should therefore investigate whether PLC activation is involved in other established INS effects in sensory neurons that implicate TRPV channel activity.

In summary, we found that infrared pulses led to PLC/IP_3 dependent Ca^{2+} release from intracellular stores in both excitable and non-excitable cell types. It is to our knowledge, the first demonstration of a direct activation of the PLC/IP_3 signaling pathway by infrared light. We propose that the thermal activation of PLC by infrared laser pulses may be a general mechanism relevant to both INS effects in neurons and other infrared responses in non-excitable cell types. The optical activation of PLC/IP_3 signaling cascades may therefore have potential uses beyond neurostimulation, including the therapeutic application of IR light. Given the robustness of these IR responses on PLC/IP_3/Ca^{2+} signaling, their effects on long-term cell viability and their dependence on PLC isoforms and G-protein coupling should therefore be pursued.

Acknowledgements D. Schubert (The Salk Institute, La Jolla, CA) is thanked for the kind gift of HT22 cells and X. Rovira (Institut de Genomique Fonctionnelle CNRS UMR5203, INSERM U1191, University of Montpellier, France) for detailed cell culture protocols. Funding for this research was received from the Region Limousin, the CNRS and an ANR Labex SigmaLim Excellence Chair awarded to Rodney P. O'Connor.

Author Biographies

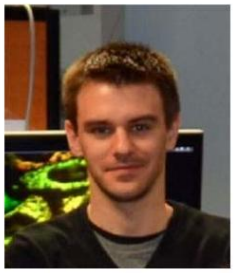

David Moreau was born in Montreuil, France, in 1991. He obtained a BSc and MSc in physics, specialized in photonics and electronics at the University of Limoges, France. He is now a PhD student at the XLIM Research Institute, Limoges, France under the direction of Rodney P. O'Connor and the supervision of Claire Lefort. His research is focused on understanding the mechanism of infrared neural stimulation.

Claire Lefort is a researcher in the French CNRS. She integrated into the Photonics team of XLIM Research Institute, Limoges, France, for her expertise in pulse shaping, multiphoton imaging and laser sources for biological applications. She studies the ability of laser sources homemade at XLIM Research Institute and their implementation for biological applications.

Jolien Pas is a PhD student in the Department of Bioelectronics (BEL) at the Centre Microélectronique de Provence of the Ecole Nationale Supérieure des Mines de Saint-Étienne. Jolien received her Bachelor of Science in Biomedical Engineering at the Technical University of Eindhoven in the Netherlands. She continued with a Master of Science in Eindhoven within the group of 'Supramolecular Medicine and Biomaterials' under the supervision of prof. E.W. Meijer. In her PhD, she is investigating the use of conductive polymers for the growth of primary cortical neuronal cultures in vitro and bioresorbable materials to minimize brain damage of neural depth probes in vivo.

Sylvia M Bardet was born in France in 1979. She received a Ph.D. degree in neurodevelopment from the University of Murcia, Spain in 2007, with a training period in San Francisco, United States. After several postdoctoral research periods in Belgium and France in neurobehavioral, genetic and cancer field, she joined the excellence laboratory research group led by Dr O'Connor where she studied cell biology and in vivo multiphoton microscopy applied to bio-electromagnetism in XLIM Institute (University of Limoges/C.N.R.S.) in Limoges, France. She is now an Associate Professor in the BioEM team led by P. Leveque in the same institute

(University of Limoges/C.N.R.S.), where she continues the same research focus on the biological effects of nanopulses.

Philippe Leveque was born in Poitiers, France, in 1964. He received the Ph.D. degree from the University of Limoges, France, in 1994. In 1995, he joined the C.N.R.S. His main area of interest concerns scattering problems of electromagnetic waves, particularly in the time domain. He is involved in the development of dosimetry and exposure setups for health-risk assessment in cooperation with biological and medical research groups. He is a senior scientist at CNRS and the group leader of Bioelectromagnetics team working in nanopulse application, in the XLIM Research Institute held by the University of Limoges and C.N.R.S. Since 2011, Dr. Leveque is a member of the Electroporation in Biology and Medicine (EBAM) European laboratory.

Rod O'Connor is an Associate Professor in the Bioelectronics department (BEL) at the Centre Microélectronique de Provence. He received a BSc(Hons) and MSc in Neuroscience from Laurentian University in Canada. His doctoral research was carried out in Prof. Sir Michael Berridge's Molecular Signaling Group at the Babraham Institute of the University of Cambridge, where he received a PhD in Biomedical Sciences for his work applying imaging to study the influence of light and pulsed microwaves on Ca^{2+} signaling. Thereafter, he held a Marie Curie fellowship at the European Laboratory for Nonlinear Spectroscopy (LENS) in Florence, Italy, applying multiphoton microscopy for in vivo imaging and femtosecond laser manipulation of the brain. He carried out further postdoctoral training in electrophysiology and optogenetics at the HHMI Janelia Research Campus in Virginia, Boston University and the Woods Hole Oceanographic Institute (WHOI) in Massachusetts. Before moving to BEL, he held a LabEx Chair in Bioengineering at the XLIM Research Institute in Limoges, where he applied advanced biological imaging tools to study the physiological effects of ultrashort, intense pulsed electric fields and infrared light in vitro and in vivo.

References

[1] J. Wells, C. Kao, K. Mariappan, J. Albea, E. D. Jansen, P. Konrad, A. Mahadevan-Jansen, *Optics Letters* **30** (5), 504-506 (2005).

[2] I. U. Teudt, A. E. Nevel, A. D. Izzo, J. T. Walsh, C.-P. Richter, *The Laryngoscope* **117** (9), 1641-1647 (2007).

[3] N. M. Fried, G. A. Lagoda, N. J. Scott, L.-M. Su, A. L. Burnett, *Journal of Endourology* **22** (3), 409-414 (2008).

[4] A. D. Izzo, C.-P. Richter, E. D. Jansen, J. T. Walsh, *Lasers in Surgery and Medicine* **38** (8), 745-753 (2006).

[5] C.-P. Richter, R. Bayon, A. D. Izzo, M. Otting, E. Suh, S. Goyal, J. Hotaling, J. T. Walsh Jr., *Hearing Research* **242** (1–2), 42-51 (2008).

[6] J. M. Cayce, R. M. Friedman, E. D. Jansen, A. Mahadevan-Jansen, A. W. Roe, *NeuroImage* **57** (1), 155-166 (2011).

[7] J. M. Cayce, R. M. Friedman, G. Chen, E. D. Jansen, A. Mahadevan-Jansen, A. W. Roe, *NeuroImage* **84**, 181-190 (2014).

[8] J. Wells, C. Kao, P. Konrad, T. Milner, J. Kim, A. Mahadevan-Jansen, E. D. Jansen, *Biophysical Journal* **93** (7), 2567-2580 (2007).

[9] A. Y. Rhee, G. Li, J. Wells, J. P. Y. Kao, in *Optical Interactions with Tissue and Cells XIX*, Vol.6854 edited by S. L. Jacques, W. P. Roach, R. J. Thomas (SPIE, San Jose, CA, USA, 2008).

[10] E. S. Albert, J. M. Bec, G. Desmadryl, K. Chekroud, C. Travo, S. Gaboyard, F. Bardin, I. Marc, M. Dumas, G. Lenaers, C. Hamel, A. Muller, C. Chabbert, *Journal of Neurophysiology* **107** (12), 3227-3234 (2012).

[11] M. G. Shapiro, K. Homma, S. Villarreal, C.-P. Richter, F. Bezanilla, *Nature Communications* **3**, 736 (2012).

[12] E. J. Peterson, D. J. Tyler, in *2012 Annual International Conference of the IEEE Engineering in Medicine and Biology Society*, (San Diego, CA, USA, 2012).

[13] B. Entwisle, S. McMullan, P. Bokiniec, S. Gross, R. Chung, M. Withford, *Biomedical Optics Express* **7** (9), 3211-3219 (2016).

[14] G. M. Dittami, S. M. Rajguru, R. A. Lasher, R. W. Hitchcock, R. D. Rabbitt, *The Journal of Physiology* **589** (6), 1295-1306 (2011).

[15] N I. Smith, K. Fujita, T. Kaneko, K. Katoh, O. Nakamura, S. Kawata, T. Takamatsu, *Applied physics Letters* **79** (8), 1208-1210 (2001).

[16] S. Iwanaga, T. Kaneko, K. Fujita, N. Smith, O. Nakamura, T. Takamatsu, S. Kawata, *Cell Biochemistry and Biophysics* **45** (2), 161-176 (2006).

[17] H. T. Beier, G. P. Tolstykh, J. D. Musick, R. J. Thomas, B. L. Ibey, *Journal of neural engineering* **11** (6), 066006 (2014).

[18] M. J. Berridge, P. Lipp, M. D. Bootman, *Nature Reviews Molecular Cell Biology* **1**, 11-21 (2000).

[19] H. Streb, R. F. Irvine, M. J. Berridge, I. Schulz, *Nature* **306**, 67-69 (1983).

[20] I. Bezprozvanny, B. E. Ehrlich, *The journal of membrane biology* **145** (3), 205-216 (1995).

[21] A.J. Verkhratsky, O.H. Petersen, *Cell Calcium* **24** (5), 333-343 (1998).

[22] N. Maggio, A. Vlachos, *Neuroscience* **281** (5), 135-146 (2014).

[23] M. Fill, J. A. Copello, *Physiological reviews* **82** (4), 893-922 (2002).

[24] H. H. Chuang, E. D. Prescott , H. Kong, S. Shields, S. E. Jordt, A. I. Basbaum, M. V. Chao, D. Julius, *Nature* **411**, 957-962 (2001).

[25] K. Venkatachalam, C. Montell, *Annual Review of Biochemistry* **76**, 387-417 (2007).

[26] P. Delmas, D. A. Brown, *Nature Reviews Neuroscience* **6**, 850-862 (2005).

[27] N. Gamper, M. S. Shapiro, *Nature Reviews Neuroscience* **8**, 921-934 (2007).

[28] J. B. Davis, P. Maher, *Brain research* **652** (1), 169-173 (1994).

[29] G. M. Hale, M. R. Querry, *Applied Optics* **12** (3), 555-563 (1973).

[30] D. Moreau, C. Lefort, R. Burke, P. Leveque, R. P. O'Connor, *Biomedical Optics Express* **6** (10), 4105-4117 (2015).

[31] M. Sessolo, D. Khodagholy, J. Rivnay, F. Maddalena, M. Gleyzes, E. Steidl, B. Buisson, G. G. Malliaras, *Advanced Materials* **25**, 2135-2139 (2013).

[32] S. L. Jacques, *Surgical Clinics of North America* **72** (3), 531-558 (1992).

[33] N. Kallweit, P. Baumhoff, A. Krueger, N. Tinne, A. Kral, T. Ripken, H. Maier, *Scientific reports* **6,** (2016).

[34] S. K. Calderwood, M. A. Stenvenson, B. D. Price, *Journal of cellular physiology* **156** (1), 153-159 (1993).

[35] V. Tseeb, M. Suzuki, K. Oyama, K. Iway, S. I. Ishiwata, *HFSP Journal* **3** (2), 117-123 (2009).

[36] Y. Wu, O. Perisic, R. L. Williams, M. Katan, M. F. Roberts, *Biochemistry* **36** (37), 11223-11233 (1997).

[37] N. Takahashi, S. Hamada-Nakahara, Y. Itoh, K. Takemura, A. Shimada, Y. Ueda, M. Kitamata, R. Matsuoka, K. Hanawa-Suetsugu, Y. Senju, M. X. Mori, S. Kiyonaka, D. Kohda, A. Kitao, Y. Mori, S. Suetsugu, *Nature Communications* **5**, (2014).

[38] A. K. Ho, D. C. Klein, *Journal of the Biological Chemistry* **262** (24), 11764-11770 (1987).

[39] M. Peters-Golden, R. W. McNish, J. K. Brieland, J. C. Fantone, *The Journal of Immunology* **144** (11), 4320-4326 (1990).

[40] H. Watanabe, J. Vriens, J. Prenen, G. Droogmans, T. Voets, B. Nilius, *Nature* **424**, 434-438 (2003).

[41] C. Xu, L. M. Loew, *Biophysical Journal* **84** (6), 4144-4156 (2003).

[42] C. Paviolo, J. W. Haycock, P. J. Cadusch, S. L. McArthur, P. R. Stoddart, *Journal of Biophotonics* **7** (10), 761-765 (2014).

[43] C. Paviolo, A. C. Thompson, J. Yong, W. G. A. Brown, P. R. Stoddart, *Journal of Neural Engineering* **11** (6), 065002 (2014).

Graphical Abstract

The ability of infrared laser exposure to stimulate intracellular Ca^{2+} signaling is investigated in cell lines of neural origin. Fluorescence live-cell Ca^{2+} imaging with Fluo-4 is used in HT22 mouse hippocampal neurons and U87 human glioblastoma cells. Activation of phospholipase C and IP_3-induced Ca^{2+} release from the endoplasmic reticulum is identified as a common mechanism of infrared-stimulated signaling in both the excitable and non-excitable cell types tested.

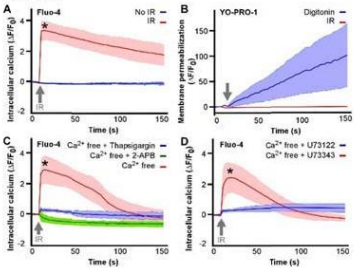

Index

Illustration table

Summary

Stimulation infrarouge de neurones

L'exposition aux radiations laser infrarouge peut être utilisée afin de dépolariser des neurones et stimuler l'activité neuronale. Le mécanisme sous-jacent d'une telle stimulation est supposé résulter d'une interaction photothermique. En effet, l'absorption de la radiation infrarouge par le tissue biologique cible, et l'eau qu'il contient, induit une augmentation de température de manière localisée, qui soit influencerait directement les propriétés membranaires de la cellule soit agirait par le biais de l'activation de canaux ioniques thermo-sensibles. Dans la plupart des cas, l'activité électrique des neurones est mesurée électriquement à l'aide de microélectrodes, mais elle peut également être sondée par le biais de la microscopie de fluorescence faisant intervenir des indicateurs calciques. Dans ce travail, l'impact de l'exposition à la radiation infrarouge sur les signaux calciques de neurones a été étudié dans le but d'éclaircir et de préciser le mécanisme résultant de l'interaction photothermique. Des neurones HT22, issus d'hippocampe de souris, et des cellules U87, issues d'un glioblastome humain, ont été utilisés en tant qu'exemples de cellules électriquement excitables et non excitables respectivement. Afin de mesurer la température et les signaux calciques au niveau cellulaire, les fluorophores Rhodamine B et Fluo-4 ont été employés. Le montage, par conséquent tout optique, pour étudier l'influence de l'exposition infrarouge sur l'activité neurale est donc présenté, ainsi que la démarche scientifique menant à l'identification de l'implication de l'activité de la phospholipase C dans le mécanisme étudié. La possibilité de stimuler l'activité neurale in vivo, dans le cerveau d'une souris, avec une mesure simultanée des signaux calciques, est également démontrée à l'aide de souris transgéniques exprimant le GCaMP6S.

Mots-clés : Stimulation infrarouge de neurones, température, fluorescence, imagerie calcique, messager IP_3.

Infrared stimulation of neurons

Infrared laser light radiation may be used to depolarize neurons and to stimulate neural activity. The underlying mechanism of such stimulation is believed to happen due to a photothermal interaction. The absorption of the infrared radiation by the targeted biological tissue inducing a local temperature increase which either directly influence membrane properties or act via temperature sensitive ion channels. Action potentials are typically measured electrically in neurons with microelectrodes, but they can also be observed using fluorescence microscopy techniques that use synthetic or genetically encoded calcium indicators. In this work, we studied the impact of infrared laser light on neuronal calcium signals to address the mechanism of these thermal effects. HT22 mouse hippocampal neurons and U87 human glioblastoma cells were used loaded with the fluorescent calcium dye Fluo-4 and with the temperature sensitive fluorophore Rhodamine B to measure calcium signals and temperature changes at the cellular level. Here we present our all-optical strategy for studying the influence of infrared laser light on neural activity, and the scientific approach leading to conclusion of the involvement of Phospholipase C activity during infrared neural stimulation. The ability of infrared exposure to trigger neural activity in mice brain *in vivo* is also investigated with the use of GCaMP6s transgenic mice.

Keywords : Infrared neural stimulation, temperature, fluorescence, calcium imaging IP_3 pathway]